



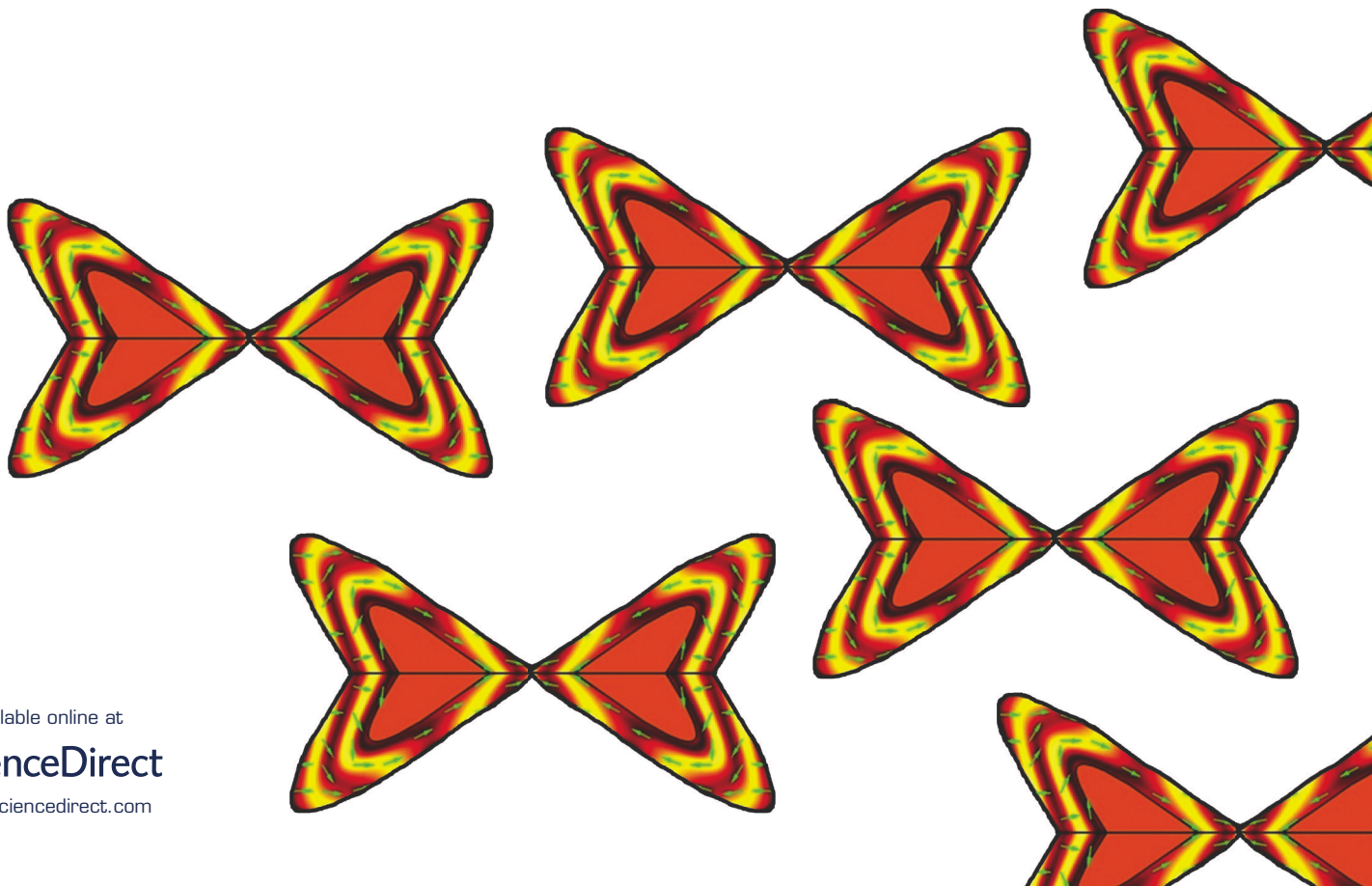
materialstoday

www.materialstoday.com

DECEMBER 2009 | VOLUME 12 | NUMBER 12

Cloaking devices

New opportunities with metamaterials





Stacks of apps.

Solartron Analytical provides a range of solutions that enable researchers to measure the electrical properties of materials. Testing at both high and low temperatures is simplified using the tightly integrated temperature control capability, while our comprehensive data acquisition / materials analysis software completes the picture and helps build a winning hand for your research.

See how our products are used in **your** application by searching our extensive online applications reference library, or book a demo or sales call, via our website at: www.solartronanalytical.com/stacksofapps



US: Tel: 1-865-425-1360
 UK: Tel: +44 (0)1252 556800
solartron.info@ametec.com

materialstoday

Published by

Elsevier Ltd.
The Boulevard, Langford Lane,
Kidlington, OX5 1GB, UK

Editorial

Commercial Editor Jonathan Agbenyega
E-mail: j.agbenyega@elsevier.com
Production Controller Lin Lucas
E-mail: materialstoday@elsevier.com

Advertising

Advertisements Manager Kevin Partridge
E-mail: k.partridge@elsevier.com
Advertisement Sales
Guy Plowman
E-mail: g.plowman@elsevier.com

Free circulation enquiries

Materials Today, Tower House,
Sovereign Park, Market Harborough
LE16 9EF, UK
Tel: +44 (0)1858 439 601
Fax: +44 (0)1858 434 958
E-mail: elsevier@subscription.co.uk

Subscription orders & payments

Materials Today (ISSN 1369-7021) is published 10 times per year by Elsevier Ltd. The Boulevard, Langford Lane, Kidlington, OX5 1GB, UK
Price: €209 / US\$234 / ¥27900
Europe/ROW Tel: +31 20 485 3757
USA Tel: +1 212 633 3730
© Elsevier Ltd. 2009.

All material published in *Materials Today* is copyright Elsevier Ltd.

Annual subscription price in the USA US\$ 234 (valid in North, Central and South America), including air speed delivery. Periodical postage paid at Rahway NJ and additional mailing offices.

USA POSTMASTER: Send change of address: *Materials Today*, Elsevier, 6277 Sea Harbor Drive, Orlando, FL 32887-4800.
AIRFREIGHT AND MAILING in USA by Mercury International Limited, 365, Blair Road, Avenel, NJ 07001.

This journal and the individual contributions contained in it are protected under copyright by Elsevier Ltd, and the following terms and conditions apply to their use: Photocopying: Single photocopies of single articles may be made for personal use as allowed by national copyright laws. Permission of the Publisher and payment of a fee is required for all other photocopying, including multiple or systematic copying, copying for advertising or promotional purposes, resale, and all forms of document delivery. Special rates are available for educational institutions that wish to make photocopies for non-profit educational classroom use.

Permissions may be sought directly from Elsevier Global Rights Department, P.O. Box 800, Oxford OX5 1DX, UK; phone: (+44) 1865 843830, fax: (+44) 1865 853333, e-mail: permissions@elsevier.com. You may also contact Global Rights directly through Elsevier's homepage (<http://www.elsevier.com>), by selecting 'Obtaining Permissions'.

In the USA, users may clear permissions and make payments through the Copyright Clearance Center, Inc., 222 Rosewood Drive, Danvers, MA 01923, USA; phone: (+1) (978) 7508400, fax: (+1) (978) 7504744, and in the UK through the Copyright Licensing Agency Rapid Clearance Service (CLARCS), 90 Tottenham Court Road, London W1P 0LP, UK; phone: +44 (0)20 7631 5555; fax: +44 (0)20 7631 5500. Other countries may have a local reprographic rights agency for payments.

Derivative Works: Subscribers may reproduce tables of contents or prepare lists of articles including abstracts for internal circulation within their institutions. Permission of the Publisher is required for resale or distribution outside the institution.

Permission of the Publisher is required for all other derivative works, including compilations and translations. Electronic Storage or Usage: Permission of the Publisher is required to store or use electronically any material contained in this journal, including any article or part of an article.

Except as outlined above, no part of this publication may be reproduced, stored in a retrieval system or transmitted in any form or by any means, electronic, mechanical, photocopying, recording or otherwise, without prior written permission of the Publisher. Address permissions requests to: Elsevier Global Rights Department, at the mail, fax and e-mail addresses noted above.

Notice: No responsibility is assumed by the Publisher for any injury and/or damage to persons or property as a matter of products liability, negligence or otherwise, or from any use or operation of any methods, products, instructions or ideas contained in the material herein. Because of rapid advances in the medical sciences, in particular, independent verification of diagnoses and drug dosages should be made.

Although all advertising material is expected to conform to ethical (medical) standards, inclusion in this publication does not constitute a guarantee or endorsement of the quality or value of such product or of the claims made of it by its manufacturer.

Printed by Headley Brothers Ltd, Kent, UK
ISSN 1369-7021
Journal number: 03069

Science is the new cool?



Growing numbers of students are electing to take science based subjects

Jonathan Agbenyega | Editor, *Materials Today* | j.agbenyega@elsevier.com

More students than ever before are opting to take science related degrees at university – and this trend is also filtering through to our nations schools which are also recording a surge in interest between 5 – 18 year olds.

These results were announced by the University and Colleges Admissions Service (UCAS). The Engineering and Physical Sciences Research Council (EPSRC) Chief Executive Dave Delpy welcomes this news and comments: "This strengthens the case for supporting our future scientists and engineers"

Dave Delpy goes on to say, "With the increase in undergraduate interest in science and engineering, we anticipate greater numbers of PhD students applying for research funding over the years to come. It is therefore more vital than ever to create a support network for school children to encourage them to engage with science and engineering at an early stage to help them become career scientists and engineers."

I feel this presents a challenge incumbent on all of us; to help educate and promote, a challenge I am sure we will all embrace with enthusiasm. Many schemes and initiatives are already evident in every day life, and just scanning the national news you will find numerous events from industrial and entrepreneurial challenges to polls such as the recent Science Museums poll to vote for the most important invention in science. From a shortlist of inventions such as the Apollo capsule, DNA double helix and the X-ray machine, it attracted an unprecedented

number of votes. To find out which invention was voted the most significant visit www.sciencemuseum.org.uk.

We still face a number of worrying issues and claims over poor levels of science literacy and teaching levels in our schools; the Chief executive of the Royal Society of Chemistry, Dr Richard Pike claims some exam papers contain absolutely no maths in them and some questions even no science. We have heard many arguments and discussions about the fears of dumbing down science, Dr Pike fears if we do not appoint a rigorous regulator soon then overall standards (even though we are witnessing a surge in interest) will suffer. Ofqual have responded and said it was taking steps to improve science.

This renewed interest in science is an opportunity to bring our best brains to the fore and discuss and engage with our next generation of scientists the challenges facing both the environment and industry at large. We must not only inform but also encourage debate, this will ensure we build on the growing interest in science and tackle head-on some of the disconnect between the quality of teaching and resources open to our young students.

The future can be a bright one for science providing we continue to build the infrastructure in our communities, and awareness and interest in our schools and colleges.

Editorial Advisory Panel

Gabriel Aeppli
University College London, UK
Caroline Baillie
Queens University, Canada
Zhenan Bao
Stanford University, USA
Franco Cacialli
University College London, UK
Martin Castell
University of Oxford, UK
Peter Goodhew
University of Liverpool, UK

Ulrich Gösele
*Max Planck Institute of
Microstructure Physics, Germany*
Hermann Grimmeiss
Lunds Universitet, Sweden
Alan Heeger
*University of California, Santa
Barbara, USA*
Mark Johnson
Naval Research Laboratory, USA
Richard A. L. Jones
University of Sheffield, UK

Neil McKeown
Cardiff University, UK
Tae Won Noh
Seoul National University, Korea
Stephen Pearton
University of Florida, USA
Marshall Stoneham FRS
University College London, UK
Helena Van Swygenhoven
Paul Scherrer Institute, Switzerland
Richard Vaia
Air Force Research Laboratory, USA

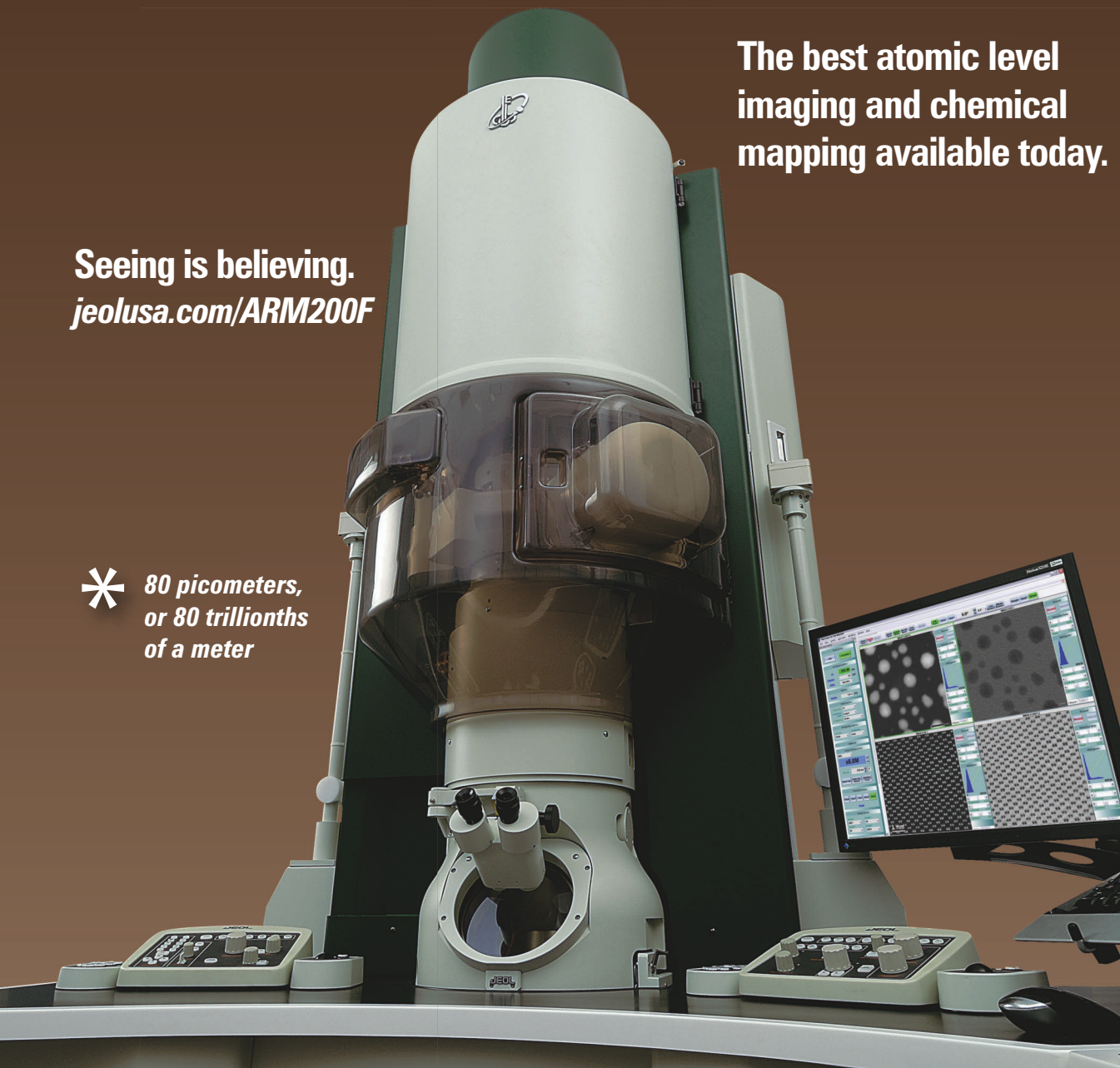
George Whitesides
Harvard University, USA
Jackie Yi-Ru Ying
*Institute of Bioengineering and
Nanotechnology, Singapore*

The Power of TEM-12*

The best atomic level imaging and chemical mapping available today.

Seeing is believing.
jeolusa.com/ARM200F

* 80 picometers,
or 80 trillionths
of a meter



JEOL

Another
Extreme Imaging
Solution

Stability • Performance • Productivity
www.jeolusa.com • salesinfo@jeol.com
978-535-5900



Atomic Resolution Microscope

Contents

materialstoday

Available online at www.sciencedirect.com SCIENCE @ DIRECT®

Regulars

■ Editorial 1

Science is the new cool?

Growing numbers of students are electing to take science based subjects.

■ Research News 8

Synthetic cells help research and provide battery power | Danish nanowires capture the sunlight | New approach produces stimuli-responsive assemblies of nanoparticles | Casting a new light on chromophores | Processing nanotube fibers goes mainstream | A hard X-ray interferometer | Graphene speeds up computers | Innovative metallic glass shows promise for bone surgery | Neuronal nanotubes | Magnetricity is taken for a spin.

Updates

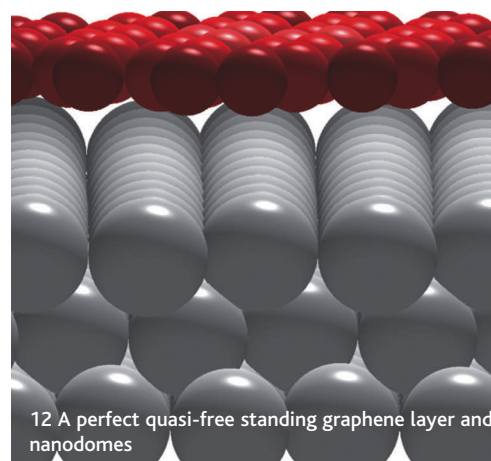
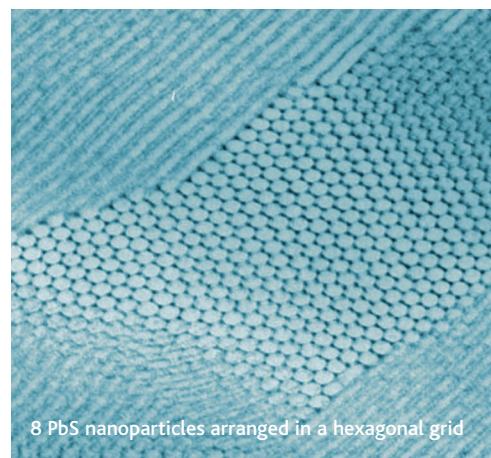
■ Tools and Techniques 70

■ Diary 72

Cite of special scientific interest

Materials Today is covered by Thomson Scientific products and services; beginning with Volume 9 (2006) articles and abstracts have been indexed in SciSearch®, Materials Science Citation Index®, Current Contents®/Physical Chemical and Earth Sciences, and Journal Citation Reports.

Our 2008 listing was recently published and after many months of speculation and anticipation the long wait was over and we were delighted to hear our first impact factor of 12.9. This figure represents an amazing achievement for our magazine and also for all those who have contributed to the content over the years both internally and within the greater research community.





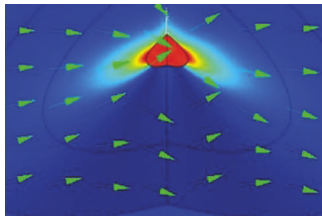
Lead story 16

Optical nano-antennas and metamaterials

Sailing He *et al.*, review some recent approaches to transmission enhancement and light harvesting based on optical nano-antennas and metamaterials. Nano-cavity antennas are used to enhance the extraordinary transmission of TM-polarized light through vertical nano-slits in a metal film.

Sailing He, Yanxia Cui, Yuqian Ye, Pu Zhang, and Yi Jin

Cloaking devices



■ Review 26

Anisotropic metamaterial devices

This paper reviews the recent progress on the parametric design of transformation devices.

Wei Xiang Jiang, Jessie Yao Chin and Tie Jun Cui

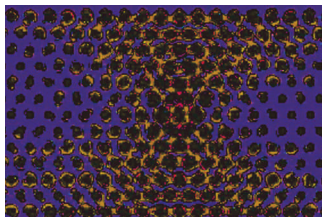


■ Review 34

Phononic crystals and acoustic metamaterials

Phononic crystals have been proposed about two decades ago and some important characteristics have stimulated practical studies in acoustic materials and devices since then.

Ming-Hui Lu, Liang Feng and Yan-Feng Chen



■ Review 44

Electromagnetic wave in 2D photonic crystals

This paper reviews recent progresses on the negative refraction and the abnormal transmission of electromagnetic wave in two-dimensional photonic crystals.

Xiangdong Zhang

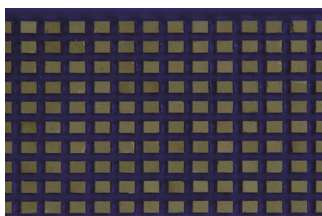


■ Review 52

Resonance properties of metallic ring systems

Lei Zhou *et al.*, review their recent efforts in understanding the resonance properties of metallic ring systems using a rigorous mode-expansion theory.

Lei Zhou, Xueqin Huang, Yi Zhang, Siu-Tat Chui



■ Review 60

Mie resonance-based dielectric metamaterials

Qian Zhao *et al.*, review the recent progresses of Mie resonance-based metamaterials by providing a description of the underlying mechanisms to realize negative permeability, negative permittivity and double negative media.

Qian Zhao, Ji Zhou, Fuli Zhang, Didier Lippens

Next issue

Materials Today will feature the current state of play in the design, performance, and viability of the biomaterials in research and clinical application of artificial organ development and regeneration.

Contents to include:

Resorbable biomaterials as bone graft substitutes

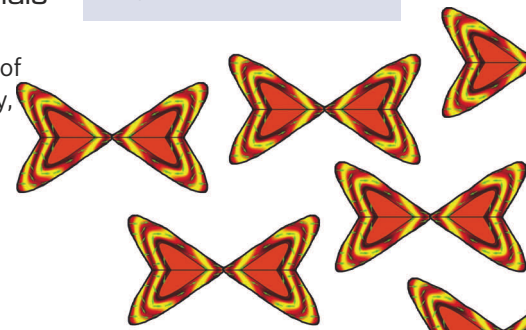
Marc Bohner looks at presenting a concise, accessible overview of the field of resorbable bone graft substitute materials.

Biological and biomimetic materials in tissue engineering

Patterson, *et al.*, reviews the biomaterial matrices which are being developed that mimic the key characteristics of the extracellular matrix.

Ultra hard biomineral in the radular teeth of *Cryptochiton stelleri*

Weaver, *et al.*, describe the architectural and mechanical properties of the radular teeth from *Cryptochiton stelleri* and explain how the unique multi-phasic design of these materials contributes not only to their functionality, but also highlights some interesting design principles that might be applied to the fabrication of synthetic composites.



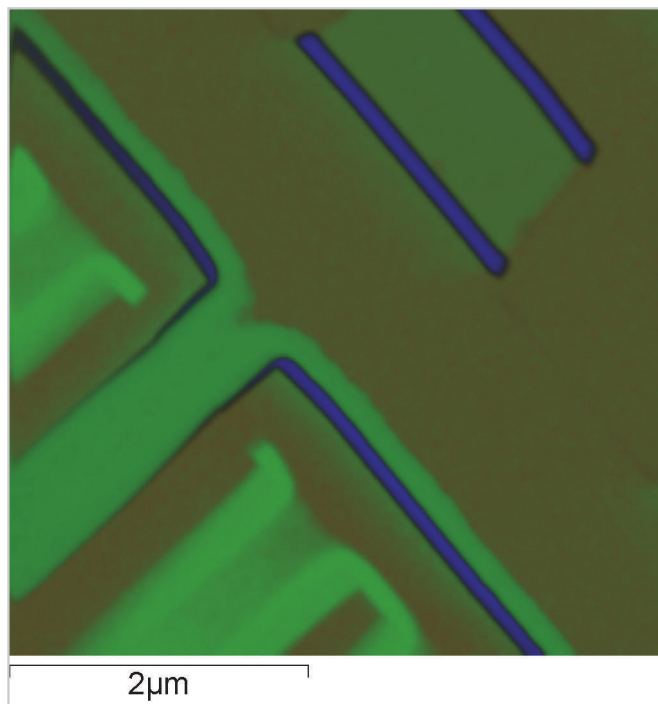
X-Max TEM

BIG performance at the NANO scale

New Large Area Silicon Drift Detector now offers **Maximum Productivity** from your TEM

X-Max TEM

- **Maximum** efficiency
 - larger solid angle for **maximum** count rate
- **Maximum** performance
 - best analytical performance for elements from beryllium upwards
- **Maximum** sensitivity
 - obtain meaningful data from nanostructures and nanoparticles
- **Maximum** convenience of LN₂ free operation
 - improved safety and reduced life cost



Semiconductor image. Sample courtesy M. Phaneuf, Fibics Inc. Ottawa



Improved collection efficiency produces X-ray maps and line scans in shorter times at higher count rates

80mm²

For further information contact us directly:
Email: nanoanalysis@oxinst.com
www.oxford-instruments.com/xmaxtem



The Business of Science®

Synthetic cells help research and provide battery power

BIOMATERIALS

Scientists have discovered a technique for using artificial cells to explore the function of molecules in actual biological cells. The new approach can help the measurement of biological systems and show how cell nanomachinery interacts within cells, which could have a major impact in the development of new medical procedures and drug discovery. The team, from Yale University and the National Institute of Standards and Technology (NIST), have developed a highly simplified model cell that includes only a few chemical processes which reproduce cell function, to help them understand how real cells can generate electric voltages and act as tiny batteries. This research shows how such cells could provide an alternative to conventional solid-state energy-generating devices and other new energy technologies.

Published online in [Xu *et al.*, *Advanced Materials*, doi: 10.1002/adma.200901945], the methodology used allows the study of cellular machinery in terms of some basic properties, such as the size of the droplets, the concentration

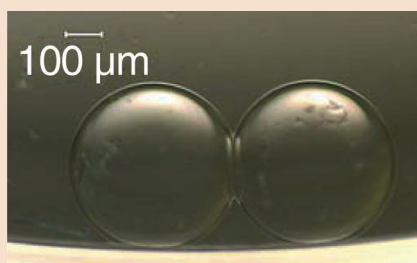


Image of two artificial cells that can act as a tiny battery.

of the aqueous solutions and the number of ion channels in the barrier between the two cells, simplifying the process of examining how biological cells work, and enabling them to examine biological energy conversion processes. The study found that a tiny battery with two droplets, each containing just 200 nanoliters of solution, could deliver electricity for almost 10 minutes, while a bigger system, with a total volume of almost 11 microliters, lasted more than four hours. Although the biological battery is not as effective as a conventional lead-acid battery, it is efficient in terms of

its ability to convert chemical into electrical energy.

The synthetic cells have a droplet of a water-based solution containing a salt – potassium and chloride ions – enclosed within a lipid wall, a molecule with one end that is attracted to water molecules while the other end repels them. If the solutions in the two cells start with different salt concentrations, then poking thin metal electrodes into the droplets creates a small electric battery.

They then inserted into the bilayer a modified form of a protein, alpha-hemolysin, which create pores that act as channels for ions, mimicking the pores in a biological cell. As David LaVan points out, "This preferentially allows either positive or negative ions to pass through the bilayer and creates a voltage across it. We can harness this voltage to generate electric current." The study has effectively demonstrated that synthetic cells can be a key method for making cell measurements, and a means to isolate and study individual components in cell systems.

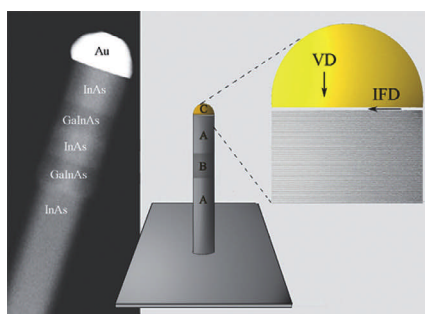
Laurie Donaldson

Danish nanowires capture the sunlight

NANOTECHNOLOGY

Danish nanophysicists have developed a new method for manufacturing nanowires. The discovery has great potential for the development of nanoelectronics and highly efficient solar cells. [Krogstrup, *et al.*, *Nano Lett.* (2009) doi: 10.1021/n1901348d]

We have improved the methodology for producing nanowires. This means we can produce nanowires that contain two different semiconductors, namely gallium indium arsenide and indium arsenide. It is an enormous breakthrough, because for first time on a nanoscale, we can combine the desirable characteristics of these two materials thus gaining new possibilities for the electronics of the future, explains Peter Krogstrup. Incredibly even today only 1 % of the world's electricity comes from solar energy. This is because we are still experiencing difficulty in efficiently converting solar energy into electricity. This latest breakthrough may change this statistic. Different materials capture energy from the sun in different and quite specific absorption areas. When we manufacture nanowires of gallium indium arsenide and indium arsenide,



Nanowire made of the two semiconductors courtesy Peter Krogstrup.

which each have their own absorption area, they can collectively capture energy from a much wider area, therefore utilizing more solar energy.

The nanowires of gallium indium arsenide and indium arsenide also have great potential in nanoelectronics. They can, for example, be used in the new OLED displays and LEDs. But it requires sharp transitions between the two materials in the nanowire.

The cultivation of nanowires takes place in a vacuum chamber. The researchers lay a gold droplet on a

thin disc comprising of the semiconductor and the nanowire grows from below. In the transition between the two semiconductor materials in the gold droplet there was previously a mixing between the materials in the gold droplet and there was a soft transition between the materials. With the new method both of the materials can go from the top of the gold droplet or from the underside of the gold droplet. When the material comes from the underside, there is no mixing of the semiconductor materials. There is therefore a sharp transition on the atomic level between the gallium indium arsenide and indium arsenide.

This sharp transition between the two semiconductors is necessary for the current – in the form of electrons, to be able to travel with high efficiency between the two materials. If the transition is soft, the electrons can easily get caught in the border area. The new mixed nanowire can be beneficial for many areas of nano research around the world, comments Peter Krogstrup.

Jonathan Agbenyega

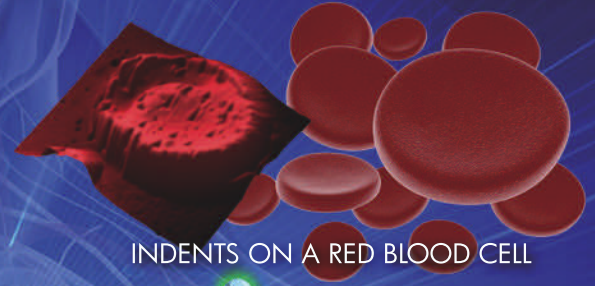
NANOMECHANICAL SENSING



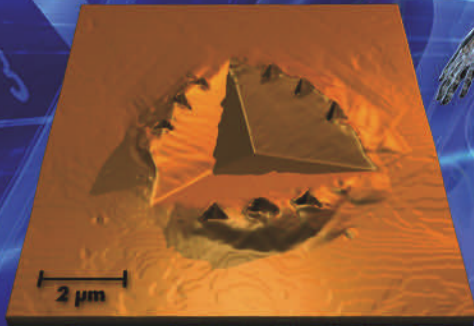
NANOINDENTATION

NANOSCRATCH

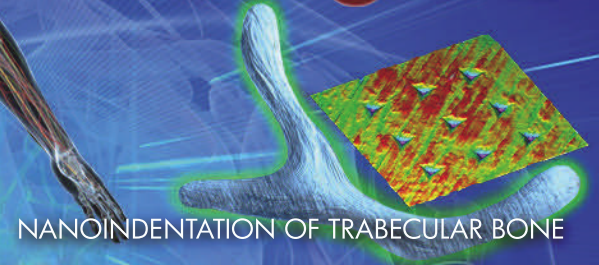
NANOWEAR



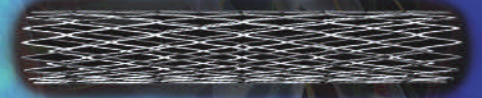
INDENTS ON A RED BLOOD CELL



IN-SITU SPM IMAGING



NANOINDENTATION OF TRABECULAR BONE



NANOSCRATCH ON A POLYMER STENT COATING

FOR **BIOLOGICAL** SYSTEMS

PI Series PicoIndenter™ and TI 950 TriboIndenter™

Once again redefining the world of nanomechanical testing

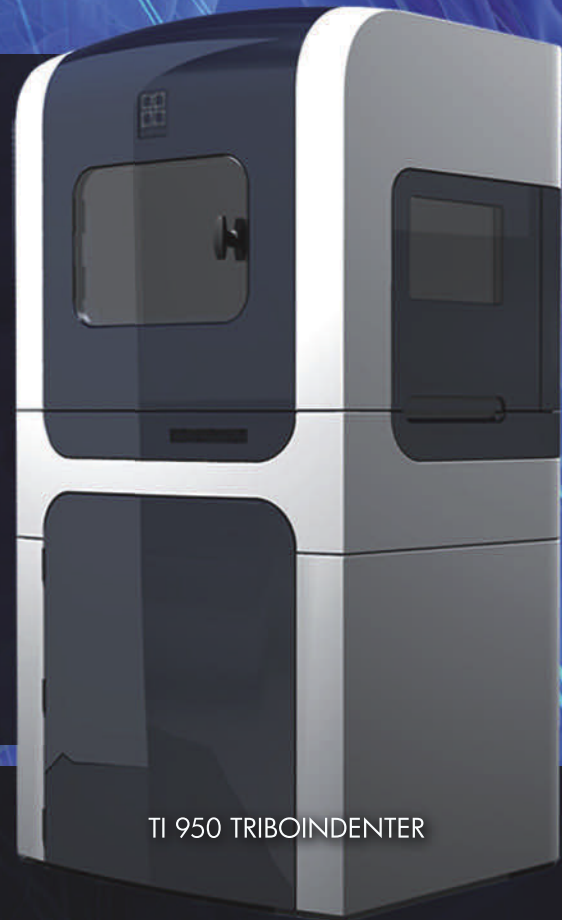
- PI Series PicoIndenter: In-situ nanomechanics in TEM/SEM
- TI 950 TriboIndenter: State-of-the-art nanomechanical testing platform
- Tissue properties; bio-mimetic structures; implant materials
- Material properties: Hardness, modulus, stiffness
- Thin films and coatings: Interfacial adhesion, wear resistance
- Friction, tribology, reciprocating wear/scratch
- Industry-leading force sensitivity with <30 nN noise floor
- Dual head capability for nano-micro scale connectivity



PI 95 TEM PICOINDENTER



PI 85 SEM PICOINDENTER



TI 950 TRIBOINDENTER



HYSITRON™

info@hysitron.com

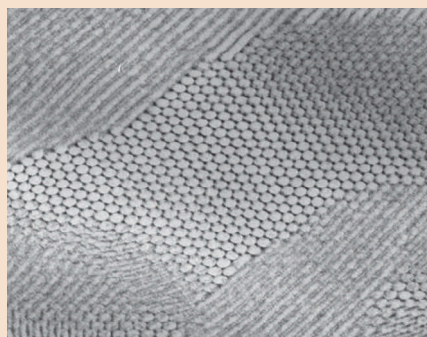
www.hysitron.com

New approach produces stimuli-responsive assemblies of nanoparticles

POLYMERS

New research has demonstrated how a blend of polymers and nanoparticles that react to different stimuli, such as heat and light, can be made by adding small molecules to the mixture. This straightforward approach could be a key development in applying such materials industrially, and could have potential for energy harvesting and storage, as well as optical devices and catalysis.

The group of scientists, from the University of California, Berkeley, the Berkeley National Laboratory, Kyoto Institute of Technology and Tohoku University, used small molecules that are attracted to the nanoparticles and certain parts of polymers. This combination orders the nanoparticles into complex shapes within the polymer material. Small molecules that change either their affinity for the polymers or their own shape in response to heat or light were then used, allowing the nanoparticle ordering within the polymers to be altered on demand. Published online in [Xu *et al.*, *Nature Materials*, doi: 10.1038/nmat2565], the study shows how this approach can be used with a variety of different blends to order the nanoparticles at different length scales with high precision. It also simplifies the material fabrication because



A blend of PS(40)-b-P4VP(5:6)(PDP)3 and 85:4nm PbS (87 vol%) nanoparticles, showing the PbS nanoparticles arranged in a hexagonal grid.

the nanoparticles can be used without further chemistry.

The main significance of the work can be seen in the use of small molecules to mediate particle-polymer interactions to selectively incorporate nanoparticles within block copolymer microdomains, the use of molecular ordering of small molecules to direct spatial arrangement of nanoparticles within copolymer microdomains, and the external stimuli-responsiveness – that is, using non-covalent interactions to direct the assembly.

The team worked on the basis that non-covalent interactions are both important and powerful, and that sophisticated structures can be obtained by blending various components and directing inter-molecular interactions. As the team's approach is essentially plug-and-play and each component can be readily switched, it may enable relatively rapid advances in these studies. The research also aids an understanding of multi-length assemblies in multi-component systems, how to measure various contributions from different components, and how to manipulate nanoscopic building blocks in a confined geometry.

The team are now examining the structure/property relationship of these nanocomposites in bulk, and are looking at how to manipulate the nanoparticle assemblies in thin films with control over their macroscopic alignment and inter-particle ordering, which should enable them to fabricate devices in a thin film setting. In addition, further research into the properties of nanoparticle assemblies may lead to some functional devices on a larger scale, especially as process used here is compatible with existing fabrication process in the microelectronic industry.

Laurie Donaldson

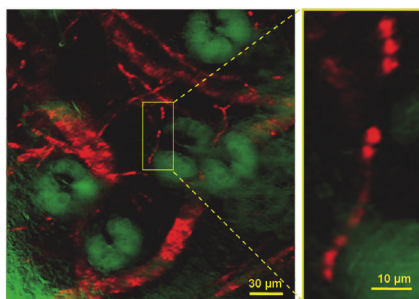
Casting a new light on chromophores

CHARACTERIZATION

Researchers from Harvard University in Massachusetts have devised a method to study non-fluorescent molecules using a technique called stimulated emission microscopy, an approach based upon a phenomenon first described by Albert Einstein in 1917 [Min *et al.*, *Nature* (2009) **461**, 1105].

Most molecules absorb parts of white light, allowing us to see them with the naked eye. However, absorption contrast is not widely used for optical imaging of molecules because of the poor sensitivity involved.

On the other hand, fluorescence microscopy, which is based upon emission rather than absorption, is a much more sensitive technique. When molecules or atoms absorb energy they enter an excited state then spontaneously decay back to lower energy levels, in some cases giving rise to fluorescence. The problem is, not all chromophores fluoresce upon decay and instead they may take a non-radiative pathway. Such molecules must either be studied using the



Ex vivo stimulated emission image of microcapillaries of a mouse ear (Image courtesy of Wei Min and Sijia Lu, Harvard University. © 2009 Nature Publishing Group.)

low sensitivity optical techniques or they need to be tagged using a fluorescent marker.

In a new technique, molecules of the sample are subjected to a pulse with the right energy and timing to enable another form of emission known as stimulated emission. In this case, emission competes with nonradiative decay such that it becomes the

dominant energy pathway back to lower, more stable energy levels. Stimulated emission offers a sensitivity that is several orders of magnitude higher than normally seen for molecules that do not fluoresce. Team leader Xiaoliang Sunney Xie explains the technique's potential in the future of medicine. "It allows spectroscopic identification of molecules in living organisms and is free from the complication of light scattering by the sample. This opens many new possibilities for biomedical imaging, such as label free mapping of drug distributions and blood vessels in tissues."

In fact, the team has already demonstrated proof-of-principle by imaging the delivery pathway of a drug that is normally difficult to study because its fluorescence is quenched on binding with tissues. The images obtained show the drug at different depths of the skin and can also confirm the hypothesis that the drug binds to cytoplasmic RNA to initiate cell death in cancerous cells.

Katerina Busuttill

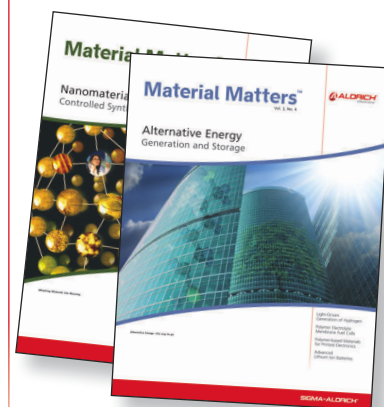
Renewable and Alternative Energy Web Portal



The Portal offers a comprehensive set of links about environmentally benign production, storage and conversion of energy.

- Solar Energy
- Hydrogen Economy
- Batteries
- Supercapacitors
- Alternative Fuels
- Relevant events and conferences are also highlighted.

We focus on materials, so you can focus on results. For more information, visit sigma-aldrich.com/renewable



Have you seen these Material Matters™ issues on Alternative Energy?

Get your complimentary subscription today:

sigma-aldrich.com/mm3

Processing nanotube fibers goes mainstream

NANOTECHNOLOGY

Rice University scientists today unveiled a method for the industrial-scale processing of pure carbon-nanotube fibers that could lead to revolutionary advances in materials science, power distribution and nanoelectronics [Rice *et al.*, *Nature nanotech.* (2009) doi:10.1038/nnano.2009.302]. The result of a nine-year program, the method builds upon tried-and-true processes that chemical firms have used for decades to produce plastics.

"Plastics is a \$300 billion U.S. industry because of the massive throughput that's possible with fluid processing," said Rice's Matteo Pasquali, a paper co-author and professor in chemical and biomolecular engineering and in chemistry. "The reason grocery stores use plastic bags instead of paper and the reason polyester shirts are cheaper than cotton is that polymers can be melted or dissolved and processed as fluids by the train-car load. Processing nanotubes as fluids

opens up all of the fluid-processing technology that has been developed for polymers."

The new process builds upon the 2003 Rice discovery of a way to dissolve large amounts of pure nanotubes in strong acidic solvents like sulfuric acid. The research team subsequently found that nanotubes in these solutions aligned themselves, like spaghetti in a package, to form liquid crystals that could be spun into monofilament fibers about the size of a human hair.

"That research established an industrially relevant process for nanotubes that was analogous to the methods used to create Kevlar from rodlike polymers, except for the acid not being a true solvent," said Wade Adams, director of the Smalley Institute and co-author of the new paper. "The current research shows that we have a true solvent for nanotubes – chlorosulfonic acid – which is what we set out

to find when we started this project nine years ago."

Following the 2003 breakthrough with acid solvents, the team methodically studied how nanotubes behaved in different types and concentrations of acids. By comparing and contrasting the behavior of nanotubes in acids with the literature on polymers and rodlike colloids, the team developed both the theoretical and practical tools that chemical firms will need to process nanotubes in bulk. "Kevlar, the polymer fiber used in bulletproof vests, is about five to 10 times stronger than the strongest nanotube fibers today, but in principle the Rice scientists should be able to make their fibers about 100 times stronger. If they can realize even 20 percent of their potential, they will have a great material, perhaps the strongest ever known.

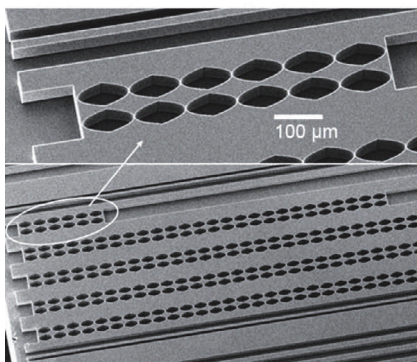
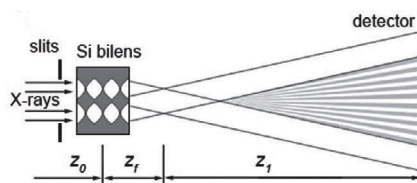
Jonathan Agbenyega

A hard X-ray interferometer

CHARACTERIZATION

A novel type of hard X-ray interferometer employing a bilens system with two parallel arrays of compound refractive lenses has been developed by scientists from France and Russia. Under coherent illumination, the bilens generates two diffraction limited mutually coherent beams. When the beams overlap they produce an interference pattern with a fringe spacing ranging from tens of nanometres to tens of micrometres. This simple way to create a X-ray standing wave in a paraxial geometry opens up the opportunity to develop new X-ray interferometry techniques to study natural and advanced man-made nanoscale materials, such as self-organised biosystems, photonic and colloidal crystals, and nanoelectronic materials.

[Snigirev *et al.*, *Phys. Rev. Lett.* (2009), **103**] present a new and simple way to generate an X-ray periodic interference field such as a standing wave with variable period ranging from tens of nanometres to tens of micrometres. The proposed interferometer thus occupies the place between crystal and grating interferometers. The silicon bilens can generate standing waves with a 40 nm period above 50 keV. If diamond lenses were employed, then we could expect the smallest pitch to be 30 nm at energies E less than 12 keV. Contrary to Bonse-Hart interferometers



SEM of a bilens interferometer.

and X-ray standing wave techniques, the bilens interferometer generates an interference pattern without the requirement of additional optics like crystals or multilayers. The interference occurs in air at a reasonable distance from the device itself allowing great flexibility in sample size and environment.

Such coherent spatially harmonic illumination can be used for new diffraction and imaging methods to study mesoscopic materials. A phase contrast imaging technique is feasible whereby a sample is inserted into one of the beams while they are separated, as in the case of a classical interferometer. Any interaction with that beam will induce significant changes in the interference pattern, allowing the extraction of high resolution information on the sample from the new phase pattern produced. A second technique would be Moiré imaging whereby the sample is placed behind the bilens within the interference field. Standing wave techniques are evident: a sample could be scanned across the periodic interference field and secondary processes (fluorescence, secondary electrons, etc.) would be detected by a detector placed to one side of the beam.

In addition to imaging applications, the bilens interferometer could also be used for coherence diagnostics at existing synchrotrons. Silicon bilenses are stable under extremely powerful beams and relatively insensitive to mechanical vibrations. We expect that they will also be widely used for beam characterisation for future free electron X-ray laser sources.

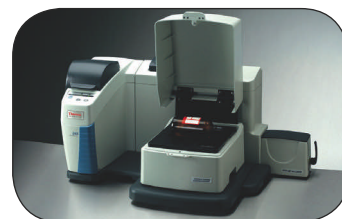
Jonathan Agbenyega

Now Anyone Can Have the Raman Touch Announcing a Breakthrough in Raman Spectroscopy

Enjoy all the benefits of Raman spectroscopy without a big investment in time, money or effort. The all-new Thermo Scientific DXR Raman systems make it possible.

DXR Raman systems allow you to focus on your own particular discipline, and not on mastering the instrument itself. Patented optics, revolutionary sampling accessories, and smart software work together to give you an intelligent analytical tool – one that eliminates the obstacles to applying Raman to everyday situations.

So, if you want Raman spectroscopy that's easy and affordable, don't compromise with trade-offs. Trade up instead, to the Thermo Scientific DXR. Visit www.spectroscopysimplified.com or call call 1-800-532-4752 or e-mail: analyze@thermo.com



**The Thermo Scientific
DXR Raman Microscope
and DXR SmartRaman
Spectrometer**

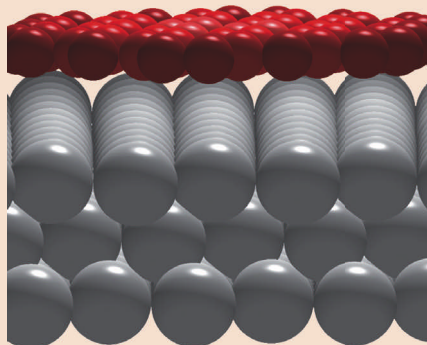
Graphene speeds up computers

CARBON

New research has shown how graphene-like structures designed on the nanoscale level – geodesic systems shaped like the Eden Project building in Cornwall, UK – could be used as building blocks for a new generation of electronic circuits, giving rise to faster computers, or mobile phones that send data at much higher rates.

Although graphene sheets are difficult and expensive to produce, their use is on the increase, especially in nanoelectronics, electrochemistry and gas sensing. Graphene, a sheet of carbon that is only one atom thick, is the thinnest known and strongest material ever measured, is thought to be about 200 times stronger than steel, and has the ability to carry one million times more electricity than copper.

While there are various methods for fabricating graphene films, such as through epitaxial growth or self-assembly procedures where graphene oxide films are transferred to a substrate and reduced to graphene by chemical reaction or heating, the approach that was taken by the research team was that of chemical vapor decomposition. This involves the deposition of hydrocarbon molecules onto an iridium surface



A perfect quasi-free standing graphene layer and our nanodomains.

that is heated between room temperature and 1,000 degrees.

The scientists, from the University of Trieste, the Synchrotron light laboratory in Trieste and the University College London, whose study has been published in [Lacovig *et al.*, *Physical Review Letters*, doi: 10.1103/PhysRevLett.103.166101], have shown how mechanisms of graphene growth have been found depending on the metal substrate, very different from those observed for two-dimensional metal islands on metals.

When these molecules hit the surface they lose their hydrogen atoms, leaving the remaining carbon atoms sticking to the iridium, where they start to self-assemble in small "nano-structures". The nano-structures eventually develop into fully formed graphene sheets; the researchers are now starting to understand how the process takes place, and therefore how it might be controlled. The study is concentrating on how the mechanism moves from a carbon-covered surface to the formation of a fully formed high-quality graphene sheet. As Alessandro Baraldi points out, "The growth of graphene starts with the formation of small islands of carbon with an unusual dome structure, in which only the atoms at the perimeter are bound to the iridium substrate while the central atoms detach from it, making the island bulge upwards at the centre."

The team also found that the size of these geodesic carbon nanodomains depended on the temperature of the metallic substrate, and the manipulation procedure, suggesting a number of possible ways of controlling the size of graphene sheets at the nanoscale.

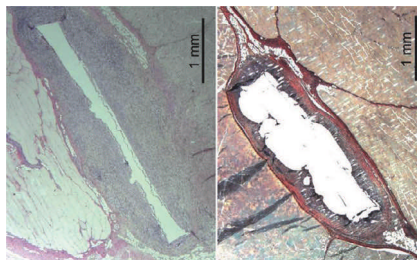
Laurie Donaldson

Innovative metallic glass shows promise for bone surgery

BIOMATERIALS

A team of scientists at the Swiss Federal Institute of Technology Zurich (ETH Zurich, www.ethz.ch), Switzerland, has developed an innovative biodegradable metallic glass that might one day replace the metal implants currently used to repair bone fractures [Zberg *et al.*, doi:10.1038/nmat2542]. The new material would make it unnecessary to undergo a second implant-removal surgery; it would also eliminate the side-effects of permanent implants by dissolving into the body, once the healing process of the bones has been achieved.

For several years, scientists have been working on the development of biodegradable implants that would exhibit strength, flexibility, durability and the ability to dissolve harmlessly in the body. Magnesium-based alloys have been found to be the most promising candidates for that purpose due to their mechanical stability, favorable dissolution properties and their ability to be absorbed by the human body without any toxicity. However, they present one major drawback: as they dissolve, they produce hydrogen gas bubbles



The new metallic glass produces no hydrogen bubbles in tissue (left). Traditional alloys form undesirable gas bubbles (right). (Image credit: LMPT/ETH Zurich.)

that linger around the implant and hinder the bone healing process.

The new metallic glass synthesized by Dr. Zberg and his colleagues, under the leadership of Prof. Jorg Löffler at the EHT Zurich, shows a fundamentally different behavior from previous materials synthesized in the past, and appears to eliminate the problem of hydrogen-forming gas. By producing a metallic glass structure, the researchers were able to develop

a magnesium-zinc-calcium alloy containing a high proportion of zinc (35%), far superior to the usual percentage used in traditional metals. Indeed, in traditional metals, undesirable crystalline phases precipitate in the magnesium matrix above a maximum amount of 2.4% zinc atoms. On the other hand, the amorphous structure of metallic glass, produced by rapid cooling of the combined mixture of molten materials, does not present such limitation. By producing a magnesium (60%)-zinc (35%)-calcium (5%) glass, the researchers were able to dramatically alter the corrosion behavior of the magnesium contained in the alloy, and therefore significantly reduce the formation of undesirable hydrogen gas in the body. In fact, animal studies performed by Zberg *et al.*, reported no clinically observable production of hydrogen-forming bubbles during the degradation process of the implant. Further studies and clinical tests will be needed to determine whether the new metallic glass fulfills all criteria for actual implementation in patients.

Elisabeth Lutanie



Bruker AXS



- Unique TWIN optics for primary and secondary beam path
- Push-button switch between Bragg-Brentano and parallel-beam geometries
- Superb LYNXEYE detector

● **The new D8 ADVANCE with TWIN/TWIN setup**

Ultimate flexibility and push-button ease of use

www.bruker-axs.com

think forward

XRD

If you need Metals & Materials...

Pure Metals, Alloys, Polymers, Ceramics, as well as many Composites and Compounds in various forms including foil, rod, tube, wire, powder, etc.

...you need
Goodfellow

Goodfellow Cambridge Limited, Ermine Business Park, Huntingdon, PE29 6WR

Tel: 0800 731 4653 OR +44 1480 424 800, Fax: 0800 328 7689 OR +44 1480 424 900

E-mail: info@goodfellow.com
www.goodfellow.com

Neuronal nanotubes

NANOTECHNOLOGY

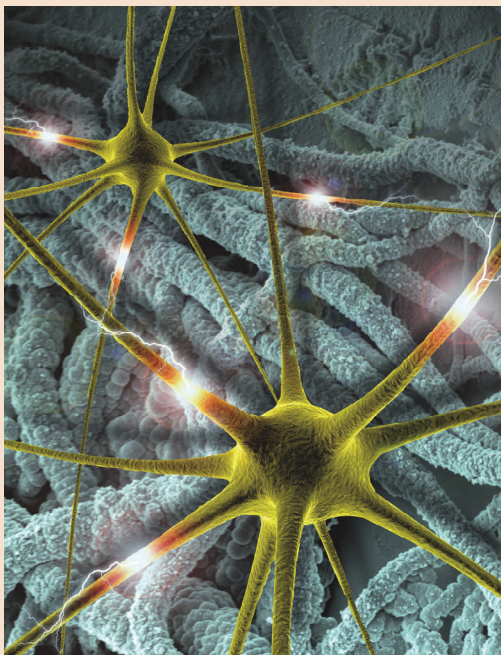
Could nanotechnology be the key to developing an interface between nerve cells and microelectronic circuitry? US scientists have recently demonstrated that signals can be recorded from rat neurons using conducting polymer nanotubes.

The research carried out at the University of Michigan might one day help in the development of sensors and treatments for neurological disorders including Parkinson's disease and paralysis.

Conventional neural electrodes can have operational times of hours or even years but all of them trigger an initial inflammatory response once they are inserted into the brain. After that, the brain settles into a chronic, wound-healing process, which can isolate the electrode from surrounding neurons as new tissue encapsulates it. Metal electrodes are obviously conducting but lack the biocompatibility that precludes this chronic wound-healing problem.

Now, nanotubes coated with the polymer poly(3,4-ethylenedioxythiophene) (PEDOT) have been used to record neural signals [Abidian *et al.*, *Adv. Mater.* (2009) 21, 3764-3770]. Mohammad Reza Abidian and colleagues explain that PEDOT is not only electrically conductive but is also biocompatible, which they hoped would prevent encapsulation.

"Microelectrodes implanted in the brain are increasingly being used to treat neurological disorders," explains Abidian. "Moreover, these



The image depicts neurons firing (green structures in the foreground) and communicating with nanotubes in the background. (Illustration courtesy of Mohammad Reza Abidian.)

electrodes enable neuroprosthetic devices, which hold the promise to return functionality to individuals with spinal cord injuries and neurodegenerative diseases." The challenge is to find ways to make robust and reliable

neural electrodes that could monitor symptoms and perhaps even deliver the appropriate medication automatically. The researchers have demonstrated the ability of PEDOT nanotubes to act as drug carriers previously.

The team has now tested their PEDOT nanotube electrodes in laboratory rats. In the experiment, they implanted two neural microelectrodes in the brains of three rats. They then monitored the electrical impedance of the recording sites and measured the quality of recording signals over a seven-week period. They found that not only was the signal-to-noise ratio of the coated electrodes 30% higher than with uncoated electrodes, but the coated electrodes operated with less electrical resistance. This meant that the electrodes could communicate more clearly with individual surrounding neurons.

"Conducting polymers are biocompatible and have both electronic and ionic conductivity," Abidian explains. "Therefore, these materials are good candidates for biomedical applications such as neural interfaces, biosensors and drug delivery systems." He adds that, "This study paves the way for smart recording electrodes that can deliver drugs to alleviate the immune response of encapsulation."

David Bradley

Magnetricity is taken for a spin

MAGNETISM

At long last there is experimental evidence that magnetic charges exist and that they have measurable currents or magnetricity, just like an electric charge [Bramwell *et al.*, *Nature* (2009) 461, 956].

A team from the UK and France used $Dy_2Ti_2O_7$, a material known as a spin ice, to test the new technique. Spin ices are predicted to have sharply defined magnetic point charge (magnetic monopole) excitations, making them good test materials.

In their recent paper, the researchers explained how they applied Onsager's theory of electrolytes,

which describes the conductivity of liquid and lattice electrolytes, to set up an experiment that can detect the magnetic monopoles in spin ice. They replaced the electrical quantities described in Onsager's theory with magnetic quantities, based on the assumption that there is equivalence between electricity and magnetism.

A spin ice sample was cooled to temperatures close to zero and then probed using muons, negatively charged elementary particles. Single crystals of spin ice were aligned parallel to the muon spin direction and a magnetic field was applied at right angles to this axis. The asymmetry of muon beta decay was then

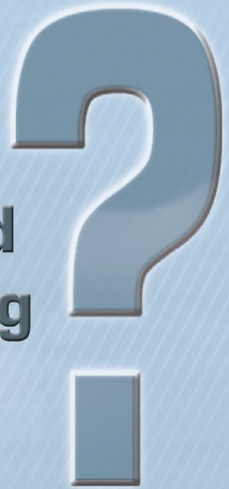
measured as a function of time, leading to information on internal magnetic fields.

Results so far have yielded a value of $5 \mu\text{B} \text{ \AA}^{-1}$ for the elementary unit of magnetic charge. The technique has not only been used to prove the existence of magnetic charges in spin ice but is also capable of measuring relative changes in magnetic conductivity. While the new technique is a good proof of theory, can be used to determine deviations from Ohm's law, and demonstrates good correlation between electricity and magnetism, it may also lead the way to controlling magnetic charges in the future.

Katerina Busuttill

Ask the experts -

‘How can I stop the edges of my polished sample from chipping in process’



James McAneny
Development Manager
30 years materials
processing experience

For the answer to this question and more common queries, visit -
www.logitech.uk.com/chipping



Now is the Time to **UPGRADE** from Basic to Automated In Situ Lift-out

- Navigate Along the SEM-FIB X, Y, Z Coordinates
- Continuous X, Y, Z Travel Over Large Distances
- Precision Closed Loop Feedback
- Save and Recall Positions
- Automation - 3D Image Recognition in the SEM-FIB
- Change Tips Without Breaking Vacuum
- Short-Cut™ for Backside Thinning and Tomography Samples



UPGRADE your Model 100.7 Nanomanipulator to an AUTOPROBE™

P: 214.572.6800 | F: 214.572.6801 | <http://www.omniprobe.com>





Optical nano-antennas and metamaterials

We review some recent approaches to transmission enhancement and light harvesting based on optical nano-antennas and metamaterials. Nano-cavity antennas are used to enhance the extraordinary transmission of TM-polarized light through vertical nano-slits in a metal film. The enhanced transmission of TE-polarized waves through an array of subwavelength-slits in a thin metal film at low frequencies (including microwave) is also investigated. Light harvesting with a metamaterial cloaking shell is also demonstrated.

Sailing He^{1,2,*}, Yanxia Cui¹, Yuqian Ye¹, Pu Zhang^{1,2}, and Yi Jin¹

¹ Centre for Optical and Electromagnetic Research, State Key Laboratory of Modern Optical Instrumentation, Zhejiang University; JORCEP (Joint Research Centre of Photonics of the Royal Institute of Technology (Sweden) and Zhejiang University), Zijingang Campus, Zhejiang University, China

² Division of Electromagnetic Engineering, School of Electrical Engineering, Royal Institute of Technology, S-100 44 Stockholm, Sweden

* E-mail: sailing@kth.se

Since its discovery¹, extraordinary optical transmission (EOT) through subwavelength apertures including single apertures²⁻⁹ and aperture arrays¹⁰⁻¹⁹ in an opaque metal film have attracted considerable attention. These nanoscale metallic structures possess a wide variety of extraordinary optical properties including beaming²⁰⁻²², local field enhancement²³, and total absorption^{24, 25}. Surface plasmons polaritons (SPPs)^{26, 27} play an essential role in this phenomenon and have opened up potential applications in lithography^{28, 29}, biophotonics^{30, 31}, Raman effect³², and other areas³³⁻³⁵. Besides at visible frequencies, these intriguing phenomena have also been found and investigated at terahertz³⁶⁻³⁸, microwave³⁹⁻⁴³, acoustic frequencies^{44, 45} and matter-waves⁴⁶.

Here we review some different approaches to transmission enhancement and light harvesting through nano-apertures, namely,

by utilizing optical nano-antennas⁹ (note that optical nano-antennas for many other applications have been studied very recently⁴⁷⁻⁵²) and metamaterials (including slow-light photonic crystal waveguides)⁵³. In this article, we will also harvest light with an invisibility metamaterial cloak shell. Metamaterials are composites with subwavelength unit cells dominating some homogenized electromagnetic properties which can not be found in a naturally occurring material⁵⁴⁻⁵⁶. Historically, the introduction of this novel concept was initiated decades ago by pursuing the theory of left-handed materials^{57, 58}. After the realization of metamaterials at microwave⁵⁹ and optical frequencies^{60, 61}, various predicted effects were demonstrated, such as evanescent wave amplification and subwavelength lensing^{62, 63}. We have also studied some potential applications⁶⁴⁻⁶⁶. Electromagnetic metamaterials with theoretically arbitrary parameters could be exploited⁶⁷. Similar methods and unit cells have also been developed to investigate single

negative, or zero-valued effective materials, where electric/magnetic plasmonic and perfect tunneling effects were observed^{68, 69}. Using metamaterials, people have studied other promising applications such as perfect absorbers⁷⁰, slow light⁷¹, polarization manipulation⁷², etc. The method of transformation optics⁷³ has greatly enlarged the potential application areas of metamaterials, enabling us to design devices according to required characteristics. Invisibility metamaterial cloak is a successful example. The ability to reduce total scattering dramatically has been predicted and verified in various ways, including rigorous analytical solution⁷⁴, numerical simulation⁷⁵, and proof-of-principle experiment^{76, 77}. Various simplified cloak designs⁷⁸⁻⁸⁰ have been proposed to avoid extreme material parameters. Similar to the widely studied electromagnetic cloaks, cloaks in other fields such as acoustics⁸¹ and matter-waves⁸², have also attracted considerable attention.

Enhance transmission of light through metallic nano-slits by utilizing optical nano-antennas

The EOT through a nano-slit in a metal film can be enhanced by introducing nano-antennas. By integration with some optical nano-antennas, the efficiency and spectral response of the EOT or a light-harvesting device could be greatly improved. Recently, Pillai *et al.*⁸³ put gold nanospheres on the surface of a Si solar cell to increase the spectral response of the thin-film cell. A gold nanorod (GNR) can work as an optical antenna whose resonant frequency can be tuned over a very broad spectrum. A GNR has two surface plasmon resonance (SPR) bands, namely the transverse and longitudinal bands. The longitudinal band is a strong one corresponding to the electron

oscillation along the long axis of the nanorod, and can be tuned from visible to near-infrared-red (NIR) region by increasing the aspect ratio (of the width to the length) of the nanorod. In our laboratory we have synthesized GNRs (see^{84, 85} and the references therein) according to the classic seed-mediated growth method and the TEM image of our synthesized GNRs is shown in Fig. 1a. GNRs with a SPR peak of 607 nm (corresponding to a GNR with an aspect ratio of 1.8), 650 nm (aspect ratio 2.4) and 710 nm (aspect ratio 2.8) were synthesized and their measured absorption spectra are shown in Fig. 1b (consistent with the results of our numerical simulation). From the photo of the three GNRs (inset in Fig. 1b), one sees that the colors of the three GNR solutions are distinct according to their different SPR resonant bands. We plan to utilize these GNRs to harvest light. Below we show how an appropriately designed plasmonic nanorod (or nano-strip in a 2D case) can be utilized to harvest light and improve the EOT.

First, we present the case of transmission enhancement with a single optical nano-antenna. Fig. 2a shows the two-dimensional (2D) schematic diagram for a metallic rectangular nano-strip (with thickness H_p and width W_p) over a metallic nano-slit of width W_s in a metal film of thickness t (with a distance of d). A plane wave of TM polarization (with the magnetic field perpendicular to the x - z plane) with wavelength $\lambda_0 = 1 \mu\text{m}$ impinges normally on the top of the structure. Intuitively, the metallic nano-strip over the nano-slit seems to block the incident light. However, through the formation of a resonant nano-cavity antenna, the metallic nano-strip can assist to couple more incident light into the nano-slit and thus enhance the transmission. Both the film and the nano-strip are made of silver, and all the results are calculated with a 2D finite element method (FEM). The transmission efficiency η is defined as the ratio of the integration

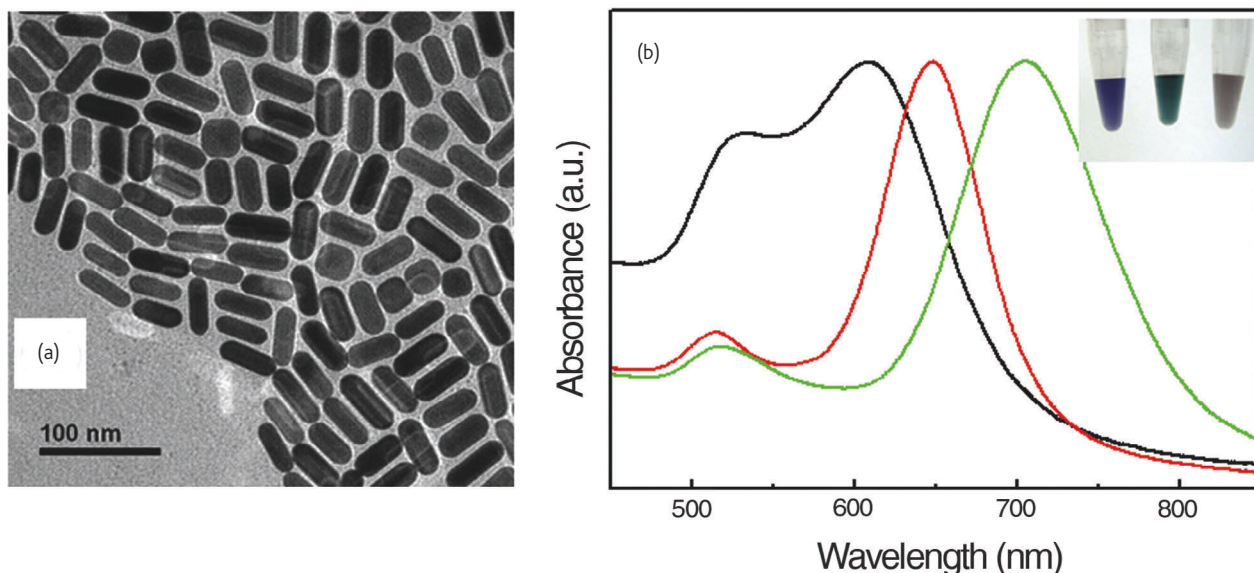


Fig. 1 (a) Measured absorbance spectra of three different types of gold nanorods with SPR peaks at 607 nm, 650 nm, and 710 nm. (b) TEM image of our synthesized gold nanorods with an SPR peak of 650 nm.

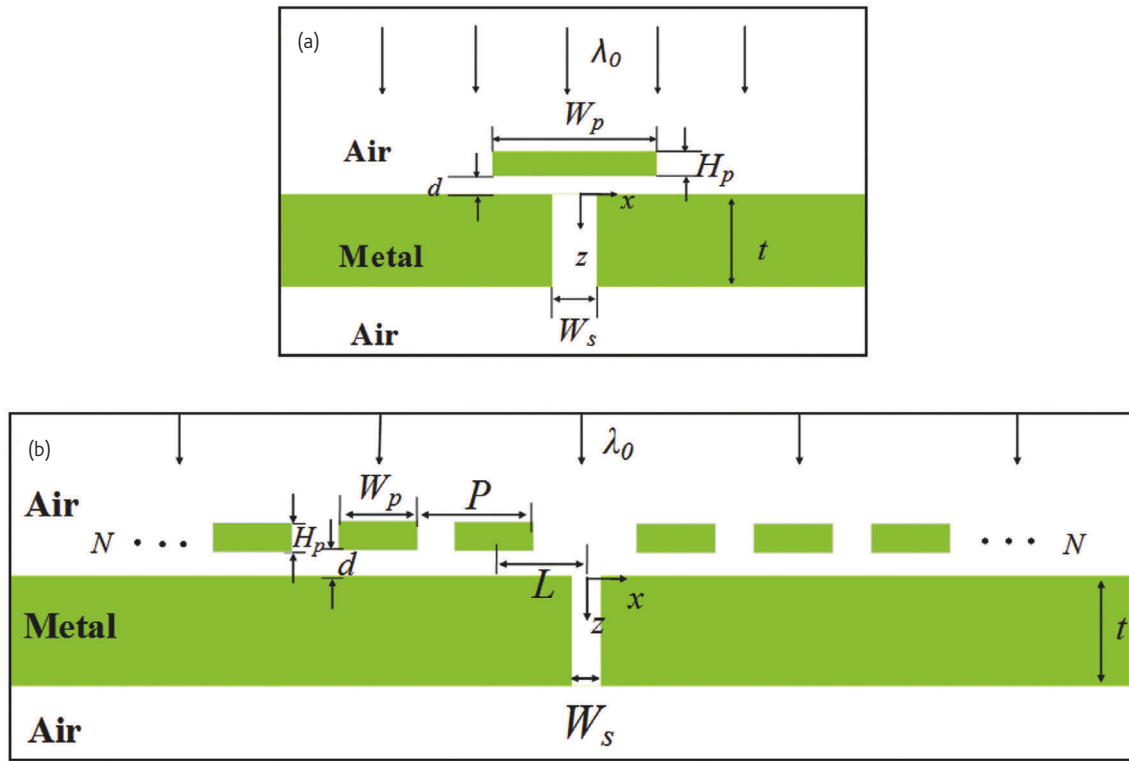


Fig. 2 Configuration of a nano cavity antenna (a) or an array of nano cavity antennas (b) placed a certain distance away from the input surface of a nano-slit aperture milled in a metal film.

of the z-component of the Poynting vector over the output opening (with or without the nano-strip) to that over the input opening of the bare slit (without the nano-strip).

A nano-slit milled in a metallic thin film can form a vertical metal-insulator-metal (MIM) waveguide of finite length, which can give Fabry-Pérot (F-P) resonance in the narrow slit region^{3, 5}. The transmission is maximal due to constructive interference for a length phase of even integer of $\pi/2$ (related to the effective wavelength in the MIM waveguide) and is minimal for a length phase of odd integer

of $\pi/2$ (due to destructive interference)³. A horizontal MIM waveguide cavity can also be formed by putting a metallic nano-strip over a metal film with an air gap in-between. Fig. 3a shows the distribution of the magnetic field modulus ($|H_y|$) when we put a silver nano-strip (with $W_p = 1 \mu\text{m}$ and $H_p = 300 \text{ nm}$) over the silver film (with $d = 44 \text{ nm}$) to form constructive interference of three peaks in the horizontal F-P cavity (close to a 3π phase length waveguide). One sees obviously that the metallic nano-strip collects the incident light effectively due to the resonance in the cavity below the nano-strip, and localized field of high

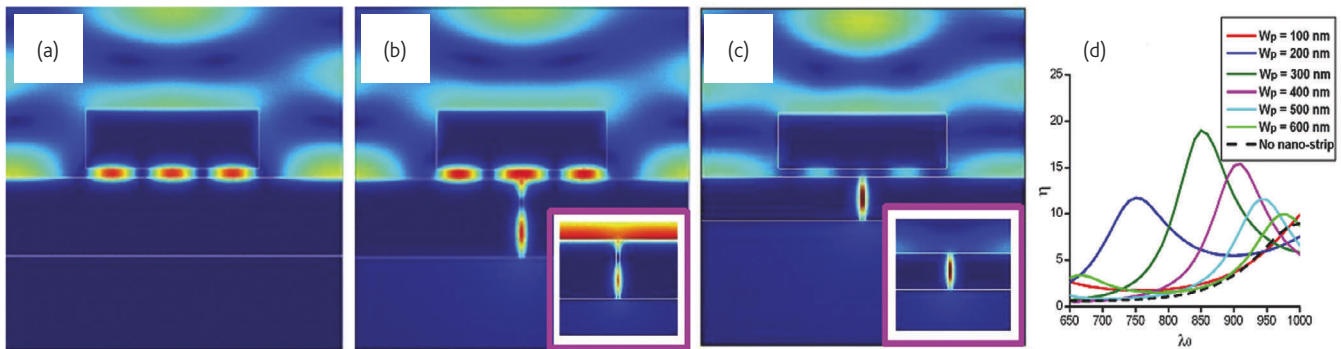


Fig. 3. Distributions of $|H_y|$ for a horizontal resonant MIM cavity ($W_p = 1 \mu\text{m}$) (a), and a horizontal resonant cavity over a non-resonant nano-slit (b) or a resonant nano-slit (c). The insets in (b) and (c) show the $|H_y|$ distributions for the corresponding cases of a bare nano-slit. (d) Transmission spectrum for various W_p when $H_p = 50 \text{ nm}$, $d = 44 \text{ nm}$, $W_s = 25 \text{ nm}$ and $t = 240 \text{ nm}$ (dashed curve is for the bare nano-slit).

magnitude is accumulated within the horizontal cavity. Then we make a nano-slit in the metal film at a position where the magnetic field in the horizontal resonant cavity is maximal and wish to enhance the extraordinary transmission through the nano-slit in the metal film. The influence of the nano-slit configuration to the field distribution in the horizontal cavity is small (large) when the vertical nano-slit is in a non-resonant (resonant) state. First we consider the case of a non-resonant vertical nano-slit with destructive interference. The inset of Fig. 3b shows the $|H_y|$ distribution for a bare nano-slit with opening width $W_s = 25$ nm (same in all simulations below) milled in a silver film of 390 nm thickness (as a vertical waveguide of $3\pi/2$ phase length). To see clearly, we plot the field distribution with doubled magnitude in this inset. The transmission efficiency for this bare nano-slit is very low ($\eta = 0.6$) and the nano-slit causes little distortion of the field reflected by the silver film. Fig. 3b shows the field distribution when there is a silver nano-strip over this non-resonant nano-slit (opened at the center where the magnetic field is maximal in the horizontal resonant cavity). The resonant cavity antenna over the non-resonant nano-slit brings an enhanced transmission, and the energy flowing out of the nano-slit aperture is enhanced by a factor of 5 as compared with that for the non-resonant bare nano-slit in the inset of Fig. 3b. The inset of Fig. 3c shows the $|H_y|$ distributions for a resonant bare nano-slit with $t = 240$ nm (corresponding to a vertical MIM waveguide of π phase length). An output transmission efficiency $\eta = 7.8$ is achieved, attributed to the constructive interference in the vertical MIM waveguide of finite length. When the silver nano-strip (same as Fig. 3a, b) is put over the resonant nano-slit as shown in Fig. 3c, the horizontal cavity can no longer keep its optimal internal field distribution for harvesting light and the cavity antenna does not work any more. Thus, the energy flowing into the nano-slit is small and η is only 3.6, lower than η in the inset of Fig. 3c. To achieve an efficient receiving antenna for harvesting light (from incident light to SPPs) and further enhancing transmission, the width of the metallic nano-strip should be carefully designed to form a resonant cavity and the

height of the nano-strip should also be small enough. When we choose $W_p = 1410$ nm and $H_p = 50$ nm, the transmission for the resonant nano-slit can be greatly enhanced to $\eta = 17.5$ (124% larger than $\eta = 7.8$ for a resonant bare nano-slit). Fig. 3d shows the transmission spectrum for various antenna widths (W_p) when $H_p = 50$ nm and $d = 44$ nm. This illustrates the tunability of the optical nano-cavity antenna for harvesting light of desired wavelength. This is quite similar to the tunability of the absorption peak of GNRs for different aspect ratios as shown in Fig. 1b. Some other properties can be found in our recent work⁹.

The light transmission enhanced by a single nano-antenna is still not high enough. This can be improved by replacing the single nano-antenna with an array of nano-antennas. Fig. 2b shows the schematic diagram for an array of nano-antennas formed by two metallic rectangular nano-strip arrays (of period P , width W_p , thickness H_p , and number N) on the left and right sides of the vertical nano-slit over a metal film. The distance between the nano-slit center and the nearest nano-strip center (slit-to-strip distance) is denoted by L . Fig. 4 shows the $|H_y|$ distribution after the resonant nano-slit ($t = 240$ nm) is assisted by a nano-cavity antenna array with $P = 900$ nm, $W_p = 700$ nm, $L = 450$ nm, $H_p = 60$ nm, $d = 50$ nm and $N = 6$. The enhanced transmission through the nano-slit is quite high ($\eta = 128.3$), which is 16.4 times of that for the bare resonant nano-slit ($\eta = 7.8$) and 6 times larger than that for the single nano-cavity antenna case ($\eta = 17.5$). The array of nano-strips could generate some strong surface plasmon wave (SPW) on the input surface. The nano-slit cavity can also generate some reflected SPW near its input opening, whose intensity is much smaller compared to the nano-strip-generated SPW. Thus, the influence of the nano-slit can be considered as a disturbance to the light distribution on the input surface. The vertical nano-slit configuration will influence the field distribution on the input surface quite differently, depending on whether the vertical nano-slit is in resonance or not^{3, 9}. Our numerical simulation results have shown that both the position of the nano-slit and distance L influence significantly

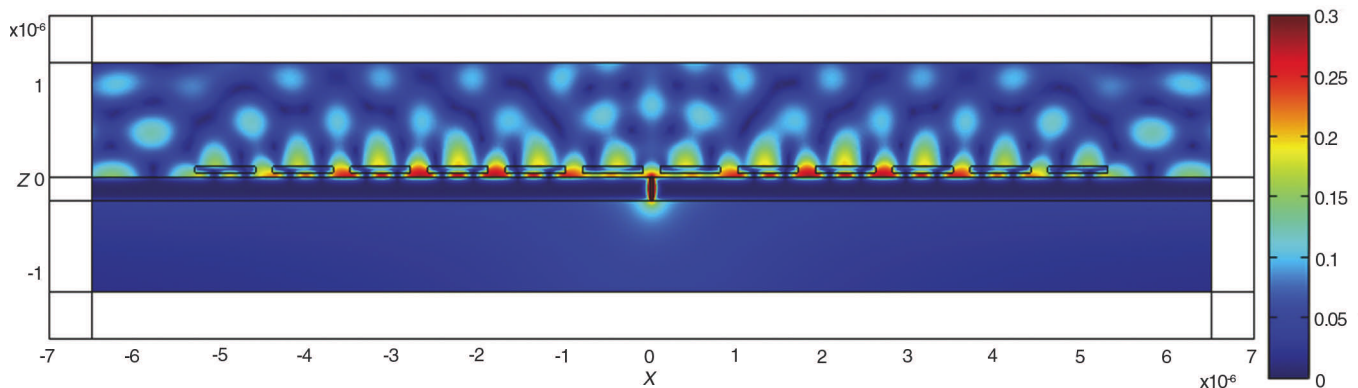


Fig. 4 Distributions of $|H_y|$ for the metallic nano-slit ($W_s = 25$ nm, $t = 240$ nm) assisted by an array of nano cavity antennas with $P = 900$ nm, $W_p = 700$ nm, $L = 450$ nm, $H_p = 60$ nm, $d = 50$ nm and $N = 6$.

the transmission of light through the nano-slit. Since non-resonant nano-slits give negligible influence to the local field distribution on the input surface, such an array of nano-cavity antennas can be combined easily with an array of non-resonant nano-slits and some potential applications can be envisaged.

Enhance transmission of low frequency TE waves through subwavelength slits in a metallic thin film by utilizing an array of electric dipole antennas

As mentioned before, many works have been carried out on enhanced transmission through subwavelength slits from optical frequencies to microwave frequencies³⁹⁻⁴³. However, most of them are for TM-polarized waves. Different from TM-polarized waves, transmission of a TE-polarized wave (with the electric field parallel to the slit wall) through a subwavelength slit has a cut-off frequency⁸⁶, below which no propagating modes exist. Thus, one would not expect a large transmission of low frequency TE-polarized wave (below the cut-off frequency) through subwavelength slits in a thin metallic film. Here we show how to utilize electric dipole antennas (metallic wires of finite lengths) to enhance the transmission of TE-polarized microwaves through the subwavelength slits at a resonant point below the cut-off frequency.

Fig. 5a shows the schematic diagram of a periodic array of subwavelength slits perforated in an aluminum film of thickness t . The slit width and the period of the slit array are denoted by g and p , respectively. Fig. 5b shows the cover layer composed of an array of broken metallic wires (electric dipole antennas) on a lossless dielectric layer with permittivity $\epsilon = 3.0$ and thickness t' . The width and length of the broken wires are w and l , respectively. The period of the broken wire array in the x and y directions are p and D , respectively. Fig. 5c shows a unit cell of the combined structure when the thin cover layer is put on the top of the metal film to enhance the transmission through the subwavelength slits.

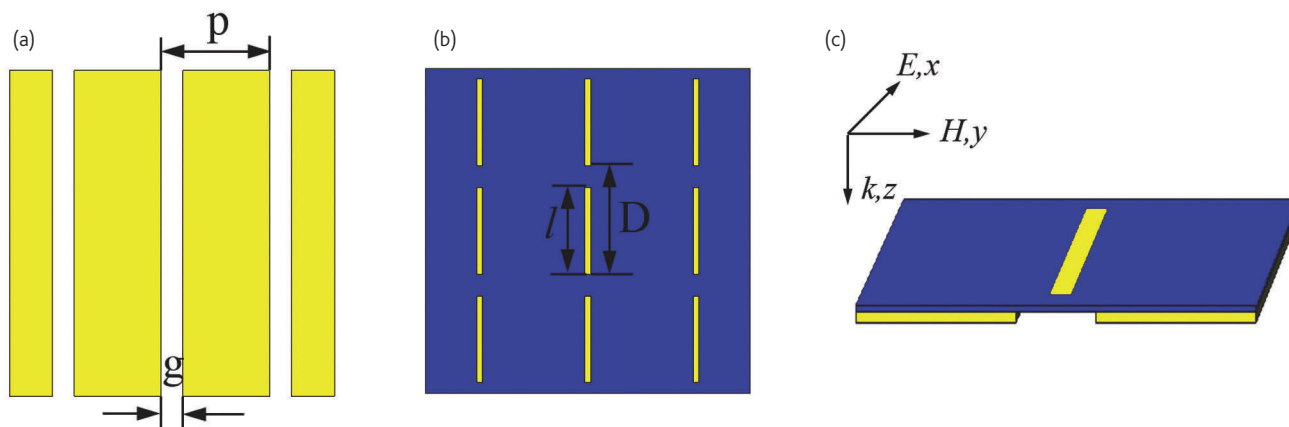


Fig. 5 Schematic diagram of (a) an aluminum film with an array of subwavelength slits; (b) a cover layer with an array of broken metallic wires; (c) unit cell for transmission calculation when the cover layer is put on the aluminum film to enhance the transmission.

By using the three-dimensional finite-difference time-domain (FDTD) method, the transmission spectrum of the slit array (without the cover layer) with $g = 5.5$ mm, $p = 30$ mm and $t = 0.5$ mm is calculated and shown by the dashed (blue) curve in Fig. 6a. Since the microwave wavelength we considered here ($\lambda > 30$ mm, corresponding to frequencies below 10 GHz) is much larger than the slit width ($g < \lambda/5$), no propagating mode can be excited in these subwavelength slits for TE-polarized waves⁸⁶. Thus the transmission can only rely on the evanescent tunneling process, and is quite low ($<0.5\%$) even for such a thin metallic film at microwave frequencies (note that the dashed curve for the transmission is magnified by 50 times to improve the visibility in Fig. 6a). However, by adding a cover layer (the parameters for the broken wire array are $l = 24$ mm, $w = 1.6$ mm, $D = 30$ mm, and $t' = 0.3$ mm) on this array of subwavelength slits, a resonant transmission peak appears at frequency $\omega = 4.88$ GHz ($\lambda = 61.5$ mm) with transmission up to 72% (see the blue curve in Fig. 6a), which is about 800 times larger than the transmission (at the same frequency) without the cover layer. The distribution of z -component electric field on a broken wire at the resonant frequency is shown in Fig. 6b, from which one sees charges of opposite signs accumulate at the two ends of the broken wire, indicating the excitation of a strong electric dipole resonance⁸⁷ on the broken wire. Based on the strong localized electric field near the input apertures of the slits, the incident wave is effectively coupled into evanescent waves, and then squeezed through the subwavelength slits. Consequently, a striking resonant transmission is achieved. The distribution of the corresponding electric field magnitude on the y - z plane at the edge of the broken wire is shown in Fig. 6c, from which one sees a highly localized electric field around the broken wire due to the electric dipole-like resonance. In fact, the metallic structure (shown in Fig. 6b) of the cover layer with broken wires can be regarded as a layer of metamaterial with electric resonance (which may give a negative value of the effective permittivity at a microwave frequency). Some detailed analysis will be published elsewhere.

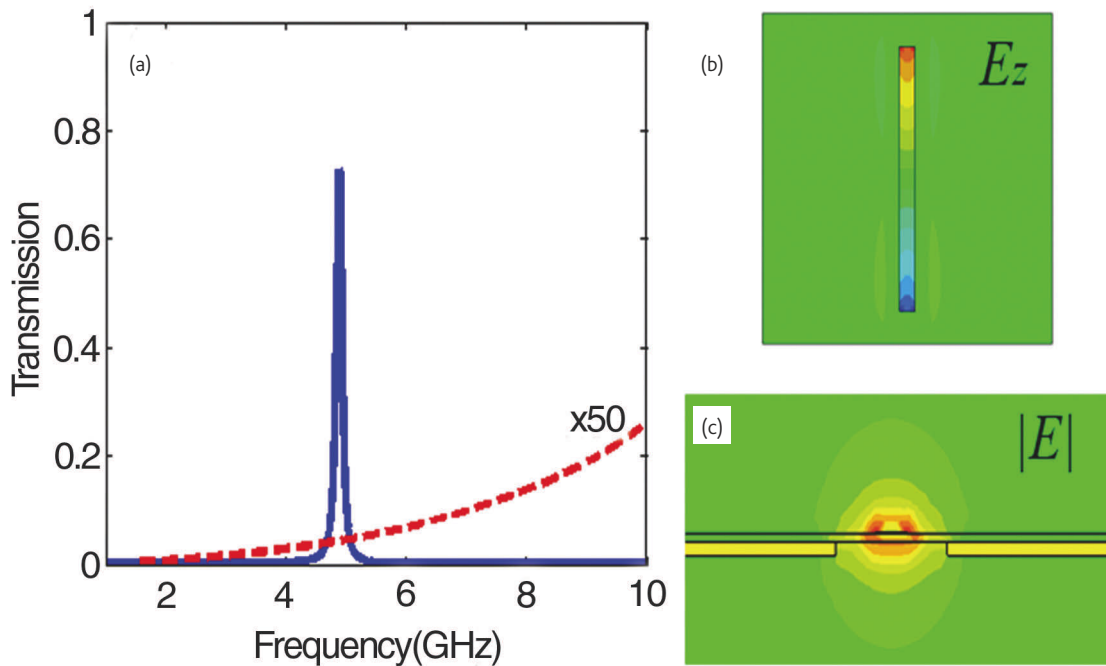


Fig. 6 (a) Transmission spectrum through the slit array without (red dashed curve) and with (blue solid curve) the cover layer. (b) Distribution of E_z on a broken wire at the resonant frequency. (c) Distribution of $|E|$ near the aperture of the subwavelength slit on the y - z plane at an edge of the broken wire.

Enhance transmission and harvest light with a horizontal slow-light photonic-crystal waveguide

As an example of enhanced transmission through an aperture in a dielectric material, we consider the resonant tunneling of a wide beam through a vertical subwavelength slow-light photonic-crystal (PC) waveguide⁵³. As an important application of PCs⁸⁸⁻⁹⁹, a slow-light PC waveguide (SPCW) can be used to enhance drastically the light-matter interactions⁹³⁻⁹⁶. In practice, efficient coupling of light into a subwavelength SPCW is an important subject^{98, 99}. When a SPCW is of finite length, large reflection at the two open ports makes the waveguide behave like a F-P cavity⁹⁴. At the resonance of a SPCW, a narrow beam can tunnel through the narrow vertical waveguide aperture efficiently. Such a resonance transmission is similar to the enhanced transmission of light through a subwavelength hole in a metal film. However, if the beam is quite wide, a large part of the beam will be directly reflected by the bulky PC (at the two horizontal side walls of the vertical SPCW) and the efficiency of the resonant tunneling is low. By utilizing an assistant horizontal SPCW, the resonant tunneling of a wide beam through the vertical SPCW can be enhanced drastically for light harvesting.

The SPCWs considered here are based on a square-lattice PC, which consists of dielectric cylinders with permittivity $\epsilon = 12.96$ and radius $r = 0.3a$ (a is the period) in air. By removing an array of cylinders along the Γ -M direction, a vertical single-line defect waveguide is formed as shown at the bottom part of the structure in Fig. 7a.

Fig. 7b gives the dispersion curve of this waveguide. At the band edge $\omega_{\text{edge}} = 0.26277(2\pi c/a)$ (near the Γ point), the dispersion curve is rather flat so that the group velocity $v_g = \partial\omega/\partial k$ is very small and the waveguide becomes a SPCW with a very small propagation constant. Large reflection exists on the interfaces between the SPCW (of finite length) and free space, and some slow guide modes satisfying the F-P resonance condition may resonate strongly inside the waveguide. The resonant frequency of the F-P resonant mode closest to ω_{edge} is $\omega = 0.26324(2\pi c/a)$. Due to the slow propagation of light, the F-P resonant mode has a large quality factor ($Q = 2.74 \times 10^3$) (the high intensity of light here can be utilized for e.g. some nonlinear applications). In our numerical simulation, we choose a wide beam with waist width $w = 13a$. From curve 2 in Fig. 7c, one sees the transmissivity is very low (only about 0.19) although the SPCW is in resonance at $\omega = 0.26324(2\pi c/a)$.

We can use an assistant horizontal SPCW to enhance drastically the transmission of the wide beam through the above vertical SPCW. To construct a horizontal asymmetric SPCW (of finite length), we put two finite-length lines of dielectric cylinders at distance $d = a$ away from the top of the vertical SPCW as shown in Fig. 7a. The resonant frequency of the composite structure becomes $\omega = 0.26329(2\pi c/a)$, shifting a bit away from that of the individual vertical SPCW due to the interaction of the two SPCWs. The Q value is reduced to 1.90×10^3 . At $\omega = 0.26329(2\pi c/a)$, a normally incident wide beam can be collected efficiently by the horizontal SPCW and then resonantly tunnels through the vertical SPCW. Curve 1 in Fig. 7c shows the drastically enhanced

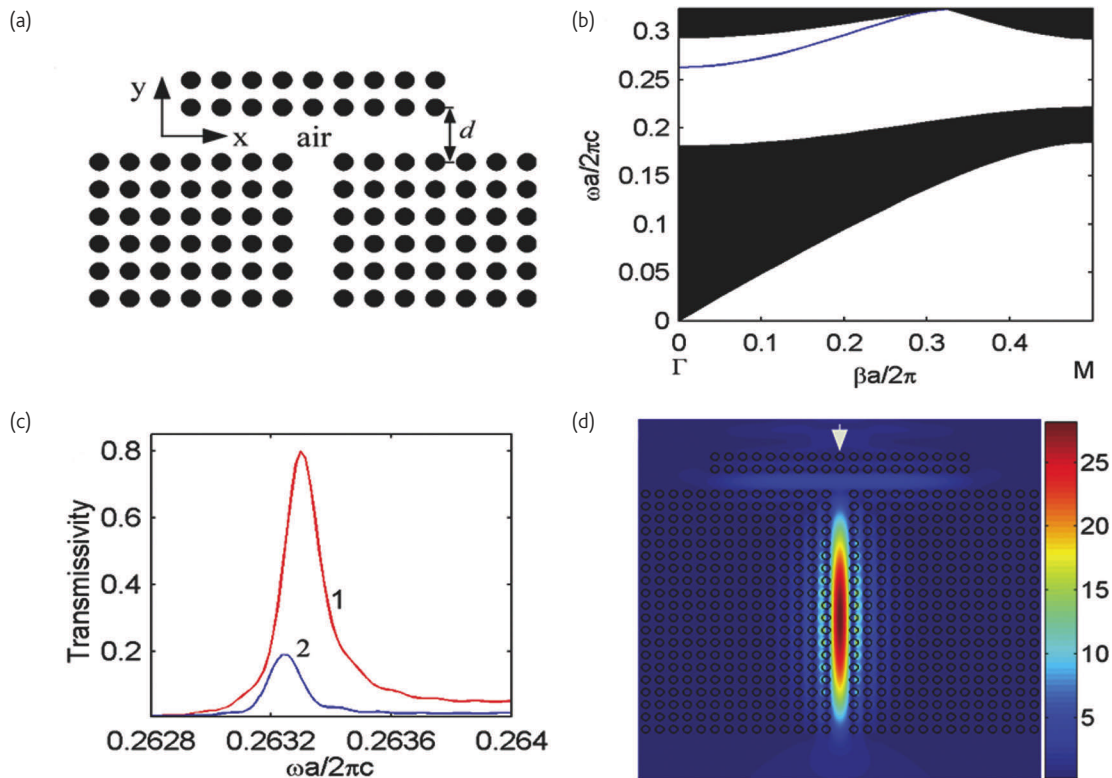


Fig. 7 (a) Harvesting light with a horizontal asymmetric SPCW (like a cavity antenna) in front of a vertical SPCW. (b) Dispersion curve of the vertical SPCW. (c) The transmissivity of a down-going wide beam (with waist $w = 13a$) through the vertical SPCW with (curve 1) or without (curve 2) the horizontal SPCW. The lengths of the horizontal SPCW and the vertical SPCW are $19a$ and $20a$, respectively. (d) Distribution of $|E_z|$ at the resonant frequency of curve 1 in (b).

transmissivity when the wide beam is normally incident on the top of the structure with the assistant horizontal SPCW (like the previous resonant cavity antenna in Fig. 2a). The largest transmissivity is about 0.80 at resonant frequency $\omega = 0.26329(2\pi c/a)$. Fig. 7d shows the distribution of $|E_z|$ at $\omega = 0.26329(2\pi c/a)$. The largest $|E_z|$ is about 28 times the amplitude of the incident beam.

To harvest light more efficiently, we can use a periodic array of vertical resonant tunneling SPCWs (instead of a single SPCW) and make the horizontal SPCW infinitely long (practically several periods wider than the beam would suffice), as shown in Fig. 8a. It is found that the transmissivity becomes nearly unity when the interval between two adjacent vertical SPCWs is $9a$. The periodic composite structure can act as a resonant cavity, and the resonant frequency and Q are $0.26311(2\pi c/a)$ and 2.15×10^3 , respectively. Fig. 8b shows the transmissivity curve (the largest transmissivity is about 0.95). Fig. 8c shows the corresponding distribution of $|E_z|$ (the strongest $|E_z|$ inside the air gaps of the vertical symmetric SPCWs is about 33 times of the amplitude of the incident plane wave). Without the horizontal SPCW, the transmissivity will be very small (less than 0.18, see curve 2 in Fig. 8b). Obviously light has been harvested efficiently with this dielectric structure. Some details can be found in our recent work⁵³.

Harvest light with a metamaterial cloaking shell

A transformation-based metamaterial cloaking shell can receive incident light efficiently (even 100% when perfectly matched), and then transport the light along the shell toward the other directions. Thus, if the light is impinged on an elliptic cloaking shell (with a very large aspect ratio) from its longer side, a great amount of light could be harvested at the two far ends of the cloaking shell. In our design example, the metamaterial cloak shell has a quasi-uniform thickness (of one wavelength). The aspect ratio is 3:1 for the inner ellipse, and 2:1 for the outer ellipse. The material parameters for the cloaking shell are calculated through the standard procedure of transformation optics⁷³, and shown in Fig. 9a. A down-going plane wave is used as an excitation in the FEM simulation. Magnetic field distribution (magnitude) in Fig. 9b shows that the light is harvested efficiently and concentrated at the two ends of the cloaking shell. One may use only the upper half of the cloaking shell and guide the harvested light to two vertical matched strips⁷⁵.

Outlook

We have reviewed and described some approaches of optical nano-antennas and metamaterials for transmission enhancement and light

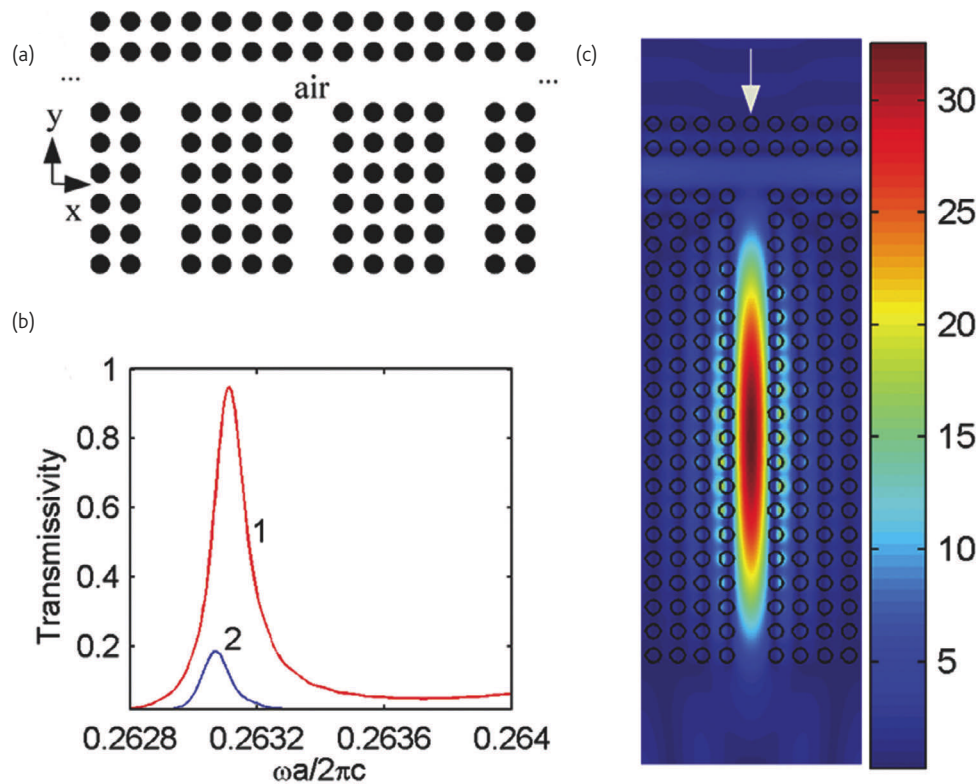


Fig. 8 (a) Harvesting light with a long horizontal asymmetric SPCW in front of a periodic array of vertical SPCWs. (b) The transmissivity of a down-going wide beam through the vertical SPCW with (curve 1) or without (curve 2) the horizontal SPCW. The length of the vertical SPCWs is $20a$ and the interval between two adjacent vertical SPCWs is $9a$. (c) Distribution of $|E_z|$ in a unit cell at the resonant frequency of curve 1 in (b).

harvesting. Enhanced transmission of light can be utilized in many near-field optics applications, whereas light harvesting is directly related to the efficiency of solar cells. In an organic solar cell, efficient light absorption in a thin film is crucial for efficiently converting sunlight to electricity. Optical antennas can be employed to harvest

external propagating light to a highly confined space for absorption in an organic solar cell. Optimally designed nano-antenna structures may improve solar cells' performances in conversion efficiency and spectral responses. We foresee that metamaterials can also play an important role in these emerging areas. [mt](#)

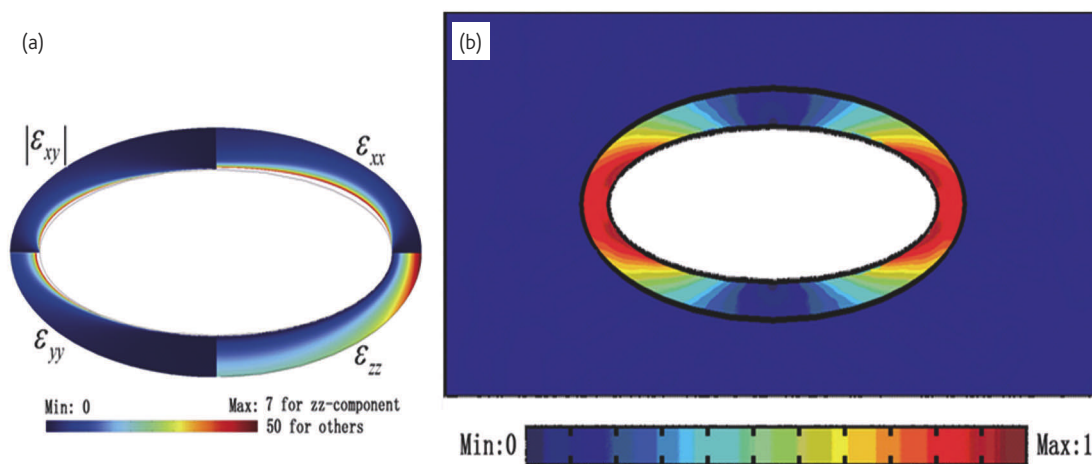


Fig. 9 (a) Non-vanishing components of the material parameters of the cloaking shell; (b) Distribution of the magnetic field magnitude (normalized) in the metamaterial cloaking shell.

Acknowledgment

This work is supported partially by the National Basic Research Program (973) of China (No. 2004CB719800), the National Science Foundation of China

(90101024 and 60688401) and the Swedish Research Council (VR) under Project No. 2006-4048 and AOARD.

References

- Ebbesen, T. W., et al., *Nature* (1998) **391**, 667.
- Thio, T., et al., *Opt. Lett.* (2001) **26**, 1972.
- Xie, Y., et al., *Opt. Express* (2004) **12**, 6106.
- Takakura, Y., *Phys. Rev. Lett.* (2001) **86**, 5601.
- Hideki, T. M., and Yoichi, K., *Phys. Rev. Lett.* (2006) **96**, 97401.
- García-Vidal, F. J., et al., *Phys. Rev. Lett.* (2003) **90**, 213901.
- Thio, T., et al., *Nanotechnology* (2002) **13**, 429.
- Degiron, A., and Ebbesen, T. W., *Opt. Express* (2004) **12**, 3694.
- Cui, Y. X., and He, S. L., *Opt. Lett.* (2009) **34**, 16.
- Ghaemi, H. F., et al., *Phys. Rev. B* (1998) **58**, 6779.
- Porto, J. A., et al., *Phys. Rev. Lett.* (1999) **83**, 2845.
- Popov, E., et al., *Phys. Rev. B* (2000) **62**, 16100.
- Xie, Y., et al., *Opt. Express* (2005) **13**, 4485.
- Gordon, R., et al., *Nano Lett.* (2005) **5**, 1243.
- Ruan, Z. C., and Qiu, M., *Phys. Rev. Lett.* (2006) **96**, 233901.
- Cao, Q., and Lalanne, P., *Phys. Rev. Lett.* (2002) **88**, 57403.
- Lezec, H. J., and Thio, T., *Opt. Express* (2004) **12**, 3629.
- Sturman, B., et al., *Phys. Rev. B* (2008) **77**, 75106.
- Liu, H., and Lalanne, P., *Nature* (2008) **452**, 728.
- Lezec, H. J., et al., *Science* (2002) **297**, 820.
- Martin-Moreno, L., et al., *Phys. Rev. Lett.* (2003) **90**, 167401.
- Yu, L. B., et al., *Phys. Rev. B* (2005) **71**, 41405.
- Perchec, J. L., et al., *Phys. Rev. Lett.* (2006) **97**, 036405.
- Teperik, T. V., et al., *Nat. Photon.* (2008) **2**, 299.
- Bonod, N., et al., *Opt. Express* (2008) **16**, 15431.
- Raether, H., *Surface Plasmons*, Springer, Berlin, (1988).
- Maier, S. A., *Plasmonics: fundamentals and applications*, Springer, New York, (2007).
- Srituravanich, W., et al., *Nano Lett.* (2004) **4**, 1085.
- Shao, D. B., and Chen, S. C., *Nano Lett.* (2006) **6**, 2279.
- Levene, M. J., et al., *Science* (2003) **299**, 682.
- Capoulade, J., et al., *Phys. Rev. Lett.* (2005) **95**, 117401.
- Kahl, M., and Voges, E., *Phys. Rev. B* (2000) **61**, 14078.
- Liu, C., et al., *Appl. Phys. Lett.* (2005) **86**, 143501.
- Bahriz, M., et al., *Opt. Express* (2007), **15**, 5948.
- Laux, E., et al., *Nat. Photon.* (2008) **2**, 161.
- Pendry, J. B., et al., *Science* (2004) **305**, 847.
- Miyamaru, F., et al., *Opt. Lett.* (2006) **31**, 1118.
- Isaac, T. H., et al., *Phys. Rev. B* (2008) **77**, 113411.
- Yang, F., and Sambles, J. R., *Phys. Rev. Lett.* (2002) **89**, 63901.
- Bravo-Abad, J., et al., *Phys. Rev. E* (2004) **69**, 26601.
- Hibbins, A. P., et al., *Science* (2005) **308**, 670.
- Ma, Y. G., et al., *Phys. Rev. B* (2007) **76**, 85413.
- Lockyear, M. J., et al., *Appl. Phys. Lett.* (2007) **91**, 251106.
- Lu, M. H., et al., *Phys. Rev. Lett.* (2007) **99**, 174301.
- Akimov, A. V., et al., *Phys. Rev. Lett.* (2008) **101**, 33902.
- Fernandez-Dominguez, A. I., et al., *Phys. Rev. A* (2008) **78**, 23614.
- Kuhn, S., et al., *Phys. Rev. Lett.* (2006) **97**, 17402.
- Schuck, P. J., et al., *Phys. Rev. Lett.* (2005) **94**, 17402.
- Muhlschlegel, P., et al., *Science* (2005) **308**, 1607.
- Tang, L., *Nat. Photon.* (2008) **2**, 226.
- Merlein, J., et al., *Nat. Photon.* (2008) **2**, 230.
- Taminiau, T. H., et al., *Nat. Photon.* (2008) **2**, 234.
- Jin, Y., and He, S. L., *Opt. Express*. (2008) **16**, 19550.
- Wood, B., *Laser Photon. Rev.* (2007) **1**, 249.
- Yu, K., et al., *Rev. Mod. Phys.* (2008) **80**, 1201.
- Soukoulis, C. M., et al., *J. Phys.: Condens. Matter.* (2008) **20**, 304217.
- Veselago, V. G., *Sov. Phys. Usp.* (1968) **10**, 509.
- Pendry, J. B., et al., *IEEE Trans. Micr. Theory & Tech.* (1999) **47**, 2075.
- Shelby, R. A., et al., *Science* (2001) **292**, 77.
- Linden, S., et al., *Science* (2004) **306**, 5700.
- Shalaev, V. M., et al., *Opt. Lett.* (2005) **30**, 3356.
- Pendry, J. B., *Phys. Rev. Lett.* (2000) **85**, 3966.
- Fang, N., et al., *Science* (2005) **308**, 534.
- Chen, L., et al., *Phys. Rev. Lett.* (2004) **92**, 107404.
- He, S. L., et al., *New J. Phys.* (2005) **7**, 210.
- Liu, L., and He, S. L., *Opt. Express* (2004) **12**, 4835.
- Sihvola, A., et al., *J. Comm. Tech. & Electron.* (2007) **52**, 986.
- Alu, A., et al., *IEEE Antenn. & Propag. Mag.* (2007) **49**, 23.
- Silveirinha, M., and Engheta, N., *Phys. Rev. Lett.* (2006) **97**, 157403.
- Landy, N. I., et al., *Phys. Rev. Lett.* (2008) **100**, 207402.
- He, J. L., and He, S. L., *IEEE Microw. & Wireless Compon. Lett.* (2006) **16**, 96.
- Hao, J. M., et al., *Phys. Rev. Lett.* (2007) **99**, 63908.
- Pendry, J. B., et al., *Science* (2006) **312**, 1780.
- Chen, H., et al., *Phys. Rev. Lett.* (2007) **99**, 63903.
- Cummer, S. A., et al., *Phys. Rev. E* (2006) **99**, 36621.
- Schurig, D., et al., *Science* (2006) **314**, 977.
- Liu, R., et al., *Science* (2009) **323**, 366.
- Yan, M., et al., *Opt. Express* (2007) **15**, 17772.
- Jiang, W. X., et al., *Phys. Rev. E* (2008) **77**, 66607.
- Zhang, P., et al., *Appl. Phys. Lett.* (2008) **93**, 243502.
- Cummer, S. A., and Schurig, D., *Phys. Rev. Lett.* (2008) **100**, 24301.
- Zhang, S., et al., *Phys. Rev. Lett.* (2008) **100**, 123002.
- Pillai, S., et al., *J. App. Phys.* (2007) **101**, 93105.
- Li, X., et al., *Nanotechnology* (2008) **19**, 355501.
- Li, X., et al., *Appl. Phys. Lett.* (2009) **94**, 063111.
- Kong, J. A., *Electromagnetic Wave Theory*, John Wiley and Sons, New York, (1986).
- Zhou, J., et al., *Opt. Express* (2007) **15**, 17881.
- Sakoda, K., *Optical Properties of Photonic Crystals*, Springer, Berlin, (2001).
- Krauss, T. F., *J. Phys. D: Appl. Phys.* (2007) **40**, 2666.
- Baba, T., *Nat. Photon.* (2008) **2**, 465.
- Mori, D., and Baba, T., *Appl. Phys. Lett.* (2004) **85**, 1101.
- Petrov, A. Y., and Eich, M., *Appl. Phys. Lett.* (2004) **85**, 4866.
- Soljačić, M., et al., *J. Opt. Soc. Am. B* (2002) **19**, 2052.
- Kiyota, K., et al., *Appl. Phys. Lett.* (2006) **88**, 201904.
- Beggs, D. M., et al., *Opt. Lett.* (2008) **33**, 147.
- He, J. L., et al., *Opt. Express* (2008) **16**, 11077.
- Vlasov, Y. A., et al., *Nature* (2005) **438**, 65.
- Vlasov, Y. A., and McNab, S. J., *Opt. Lett.* (2006) **31**, 50.
- Hugonin, J. P., et al., *Opt. Lett.* (2007) **32**, 2638.

Thermal Analysis Excellence



Mettler-Toledo AG, Analytical
CH-8603 Schwerzenbach
Tel. +41-44-806 77 11

► www.mt.com/ta
www.mt.com/ta-webinars

Innovative Technology
Versatile Modularity
Swiss Quality

METTLER TOLEDO sets
the standards in thermal
analysis as with its world-
class balances.

METTLER TOLEDO

SPIE Photonics West

23–28 January 2010
San Francisco, California, USA

Connecting minds for global solutions
Gain visibility at the essential photonics and laser conference.

Biomedical Optics • Integrated Optoelectronics • Lasers and Applications • Micro & Nanofabrication

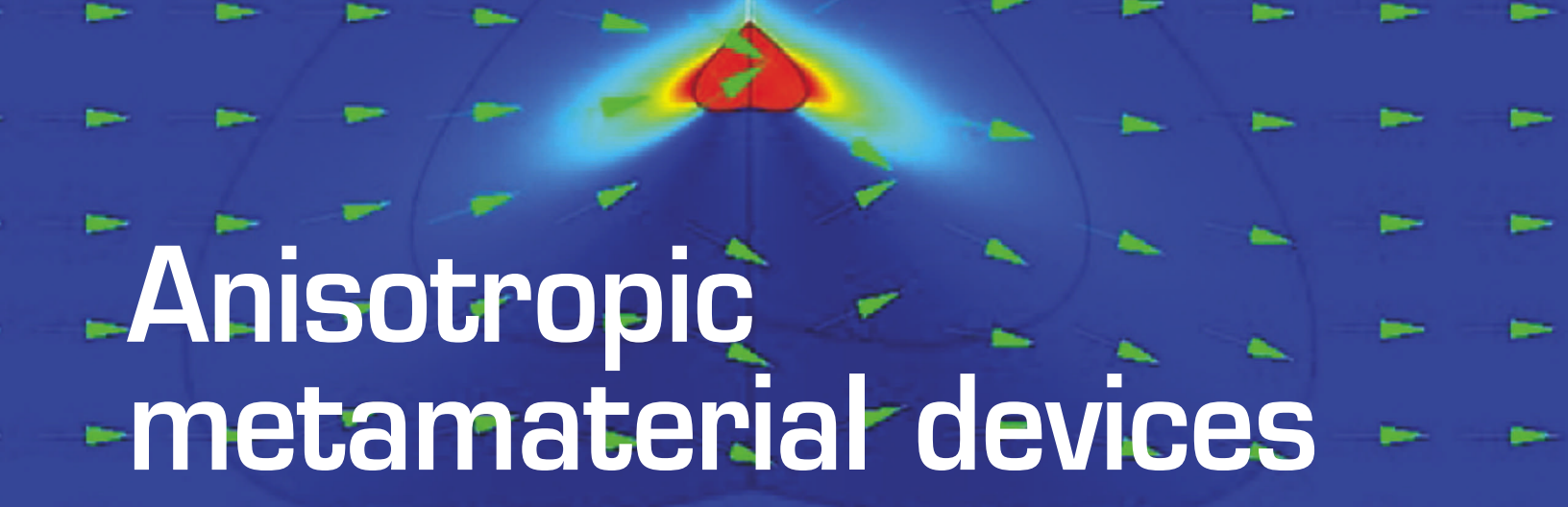
Register Today



SPIE

Connecting minds. Advancing light.

spie.org/pw



Anisotropic metamaterial devices

In the last few years, a rapid development has been achieved in a subject area, so called optical transformation, which is based on the property of metric invariance in Maxwell's equations. Optical transformation, also known as transformation optics, allows metamaterials to be tailor-made according to practical needs. In this paper, we have reviewed the recent progress on the parametric design of transformation devices, such as invisibility cloaks, electromagnetic (EM) concentrator, EM-wave converter, etc. The technique of optical transformation can also be applied when the sources are included in the transformed space.

Wei Xiang Jiang, Jessie Yao Chin and Tie Jun Cui*

State Key Laboratory of Millimeter Waves, Institute of Target Characteristics and Identification, Department of Radio Engineering, Southeast University, Nanjing 210096, People's Republic of China

*E-mail: tjcui@seu.edu.cn

In 2006, Pendry *et al.*¹ proposed a mathematical description of optical transformation, which was soon regarded as an efficient method to manipulate electromagnetic (EM) waves using artificial media. The required electric permittivity and magnetic permeability of such media can be derived from the optical transformation^{2, 3}. Alternatively, an optical conformal mapping method was used to design a medium that generated perfect invisibility in the ray-tracing limit^{4, 5}. The invisibility cloaks were analyzed in details using the optical transformation⁶, and verified numerically by full-wave simulations⁷ and experimentally by a two-dimensional (2D) near-field mapping configuration at the microwave frequency⁸. Inspired by the progress in both theoretical and experimental studies of the invisibility cloaks, more and more researchers have put their effort

into this subject area^{9–18}. In addition, other devices such as EM rotators^{19–24} have been proposed to illustrate the versatility of optical transformation.

Formulation of optical transformation

Starting from the general procedure of transformation optical design, we here restrict our discussion to transformations that are time invariant^{3, 6}, i.e. the media is only dependent of spatial coordinates. Suppose that the coordinate transformation between the original space (x, y, z) and the new transformed space (x', y', z') is

$$\begin{aligned}x' &= x'(x, y, z), \\y' &= y'(x, y, z), \\z' &= z'(x, y, z).\end{aligned}\tag{1}$$

With the above equations, we can obtain the Jacobian transformation matrix, which is defined as

$$\Lambda = \frac{\partial(x', y', z')}{\partial(x, y, z)} = \begin{pmatrix} \frac{\partial x'}{\partial x} & \frac{\partial x'}{\partial y} & \frac{\partial x'}{\partial z} \\ \frac{\partial y'}{\partial x} & \frac{\partial y'}{\partial y} & \frac{\partial y'}{\partial z} \\ \frac{\partial z'}{\partial x} & \frac{\partial z'}{\partial y} & \frac{\partial z'}{\partial z} \end{pmatrix}. \quad (2)$$

By the metric invariance of Maxwell's equations², the constitutive parameter tensors of the medium in the transformed space can be expressed as

$$\bar{\epsilon}' = \frac{\bar{\Lambda} \cdot \bar{\epsilon} \cdot \bar{\Lambda}^T}{\det(\bar{\Lambda})}, \quad \bar{\mu}' = \frac{\bar{\Lambda} \cdot \bar{\mu} \cdot \bar{\Lambda}^T}{\det(\bar{\Lambda})}, \quad (3)$$

in which $\det(\bar{\Lambda})$ is the determinant of the Jacobian matrix. Hence, the material parameters of the transformation medium can be obtained using the proposed method. Since the permittivity and permeability of the required media are often less than 1, generally, the transformation devices are composed of inhomogeneous and anisotropic metamaterials.

Invisibility cloaks

Based on the theory of optical transformation, a volume of free space can be transformed into a shell-type region, which can therefore hide the object inside the shell from incident EM waves. Further investigations have been conducted, based on pioneering work^{1, 6-8}. In order to provide more insights into the physics, several groups have developed analytical methods based on Maxwell's equations to reveal the nature of invisible cloaking¹³⁻¹⁸. In the earlier investigations, all theoretical analyses, numerical simulations and parameter designs were devoted to circularly cylindrical and/or spherical cloaks, which were relatively easy to design and analyze. Though the circularly cylindrical or spherical cloaks can wrap up any objects to be invisible, they are not efficient or convenient for long and thin objects. As a consequence, cylindrical cloaks with elliptical shapes were presented to design invisibility with generality²⁵⁻²⁸. Consider an elliptical-cylindrical object with an arbitrary axis ratio embedded in free space, which is covered by an elliptical cloak: the cross section of the cylindrical cloak is an elliptical shell, the inner and outer short semi-axes of which are a and b , respectively. The inner and outer ellipses have the same axis ratio k , which describes a horizontal elliptical cloak when $k > 1$, a vertical elliptical cloak when $k < 1$, and a circular cloak when $k = 1$ (see²⁵). Along the cylindrical axis (z axis), the transformation is an identity, hence we present the coordinate transformations for the elliptical cloaking in the xoy plane. Similar to the circularly cylindrical cloak, the transformation will compress the space from the outer elliptical region into the elliptical shell region. We can define the coordinate transformations as

$$\begin{aligned} x' &= \left(\frac{b-a}{b} + \frac{ka}{\sqrt{x^2 + k^2 y^2}} \right) x \\ y' &= \left(\frac{b-a}{b} + \frac{ka}{\sqrt{x^2 + k^2 y^2}} \right) y \\ z' &= z \end{aligned} \quad (4)$$

Based on Eq. (4), we can obtain the values of relative permittivity and permeability tensors for the cloak defined by Eqs. (2) and (3). Fig. 1 shows the comparison between the electric field distributions and the power-flow lines in the transformed space and the physical space. In the cloak, the power-flow lines propagate smoothly around the inner elliptical region and the equal-phase surfaces are warped smoothly in the predicted way. Outside the cloak, the transverse-electric (TE)-polarized plane waves are nearly unchanged as if there were no objects in the free space. Hence the invisible elliptical cloaking is well verified.

Similar to the invisibility cloak, constitutive tensors of EM masking arbitrarily shaped convex conducting objects have been derived²². Such a masking can be regarded as a partial cloaking layer. Only when the ratio between the maximum and minimum radii of the object approaches 1, i.e., the object is a sphere, could the masking be equivalent to an invisible cloak²². Invisible cloaks of different shapes including a square cloak were reported³⁰⁻³⁶, and a general method, namely, the non-uniform rational B-spline (NURBS)²⁹, has been applied to design arbitrarily shaped transformation devices.

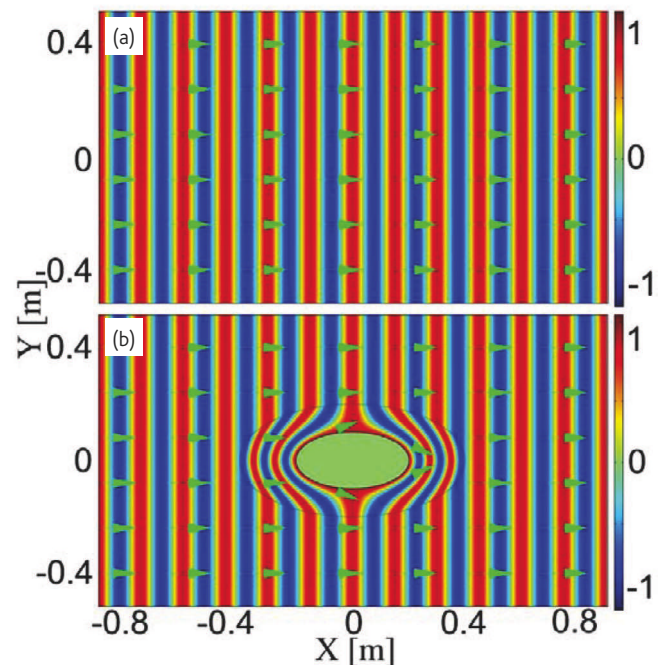


Fig. 1 (a) Transformed space. The figure shows the propagation of a plane wave. (b) Physical space. The cloaking layer makes the EM waves propagate around the invisible region and return to their original propagation directions without distorting the waves outside the elliptical cloak.

NURBS is one of the most common mathematical tools to represent curves in geometric modeling. It is possible to split an arbitrary curve represented by NURBS into a sequence of Bézier curves. By introducing NURBS to represent the geometric modeling of any objects, analytical formulas of the permittivity and permeability tensors for the arbitrarily shaped transformation devices can be expressed^{31, 53}. Moreover, the usage of NURBS will expand the generality of the transformation optics and could make a very general tool to interface with commercial softwares such as 3D STUDIOMAX and MAYA, and, hence the transformation optics can be made for the industrial use. Fig. 2 illustrates the simulation results of a heart-shaped cloak when the plane waves are incident from two different directions³¹. The geometric boundary of the cloak is represented by NURBS. In both cases, the power-flow lines within the cloak layer propagate smoothly around the heart-shaped object, making it invisible. It is even true when the incident waves travel toward the concave area of the cloak, as shown in Fig. 2b.

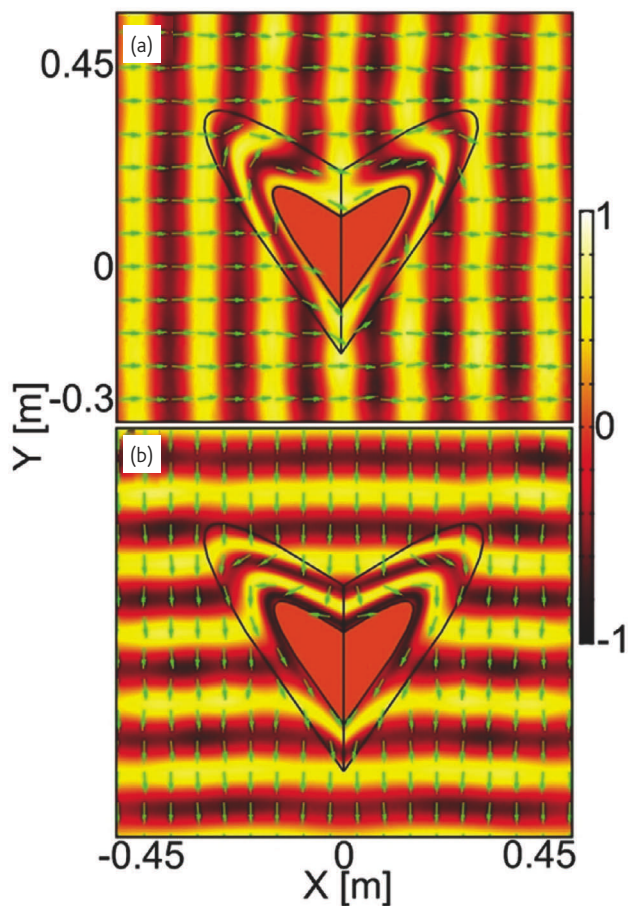


Fig. 2 The electric field distributions and power-flow lines in the computational domain for a heart-shaped cloak and a perfectly-electrical-conducting (PEC) object with different incident directions. (a) The plane waves propagate from the left to the right. (b) The plane waves propagate from the top to the bottom.

One of the challenges to realize the full-parameter cloak is that, at its inner boundary, there often exist singularities in the material parameters, which make the full-parameter cloak difficult to achieve even by using metamaterials⁸. In view of the difficulty to realize the full-parameter cloak and the imperfection of reduced-parameter cloak, a recently published theory has described a carpet cloak, which can cause anything swept under a conducting plane to seem to disappear³⁷. The great advantage of the carpet cloak is that it does not require singular values for the material parameters. The experimental validation of the carpet cloak design reported by Li and Pendry³⁷ has been recently achieved with a broadband property⁴⁰. A similar cloaking over a dielectric half-space using a singular cloak was proposed³⁸. More recently, the optical transformation of a curved, non-Euclidean space has been presented, which does not require the extreme properties of materials and can lead to invisibility in a broad band of the spectrum³⁹.

To avoid any singularity in the constitutive parameters, it was also proposed that an elliptical cloaking region can be crushed to a line

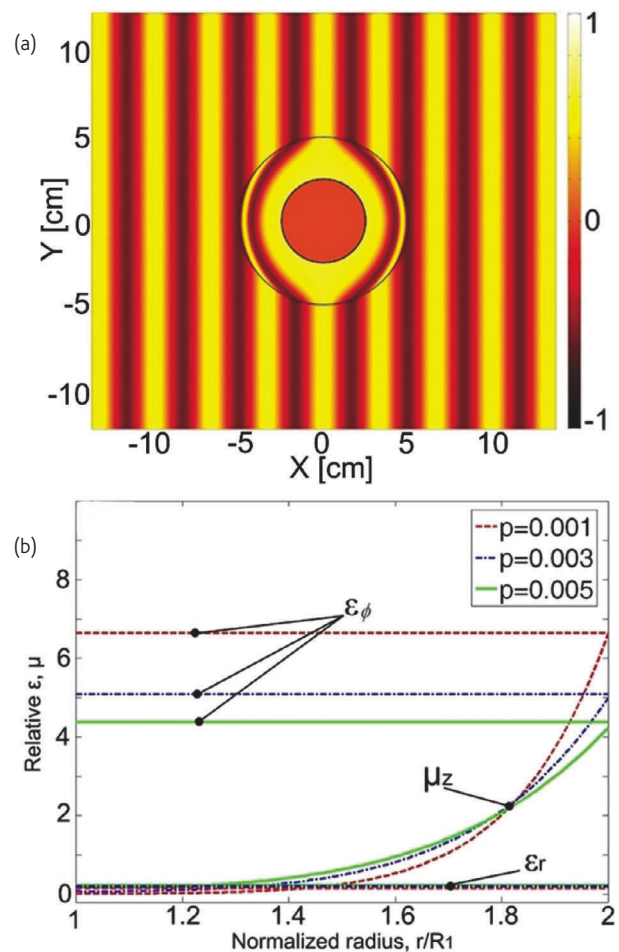


Fig. 3 (a) The distributions of the magnetic fields inside circular cloaks with an inner radius of 0.025 m, an outer radius of 0.05 m, and half of the focus $p = 0.001$ m. (b) The distributions of ϵ_r , ϵ_ϕ and μ_z components in the cloak region.

segment using the coordinate transformation in the classical elliptical-cylindrical coordinate system⁴¹, instead of being shrunk to a point. When the focus of the ellipse becomes very small, the elliptical cloak approaches a circular cloak. The advantage of such an invisible cloak is that none of the parameters is singular and the changing range of all parameters is relatively small. The full-wave simulation result for an approximately circular transverse-magnetic (TM) cloak⁴¹ is illustrated in Fig. 3a. One observes that the phase fronts are bent smoothly around the perfectly-electrical-conducting (PEC) object inside the cloak, and the fields are smoothly excluded from the interior region with the tiny scattering. All material parameters for the above circular cloaks have relatively small ranges. Fig. 3b illustrates the parameter distributions inside the approximate TM cloaks. Obviously, for each case, the electric permittivities ϵ_r and ϵ_ϕ are constant, and the magnetic permeability μ_z ranges from 0 to a small constant, all of which can be realized using metamaterials. From Fig. 3a, we clearly observe that the approximate cloak can achieve almost perfect cloaking performance because the cloaked object is crushed nearly to a point, which results in tiny scattered fields.

An approximate quantum cloaking was presented⁴², and some other designs of transformation functions and nonmagnetic cloaks were reported⁴³⁻⁵⁰. In above discussions, the transformation medium is a metamaterial shell with its interior and exterior boundary of the similar shapes. In reality, however, the shielded object may have an arbitrary shape and the interior boundary of the metamaterial shell is preferred to be the same as the shape of the shielded object. Meanwhile the shape of the exterior boundary has to fit the external environment. Hence the exterior shape of the metamaterial shell is not always the same as the interior shape. As a consequence, it is necessary to discuss the design of cloaks with different inner and outer boundaries by the method of optical transformation.

An invisible cloak with non-conformal interior and exterior boundaries using the technique of optical transformation⁵¹ was proposed. To illustrate its principle, we consider a shape with a square outer boundary and a circular inner boundary. The design of other cloaks with complicated and non-conformal interior and exterior boundaries can be achieved in a similar way⁵². Fig. 4 illustrates the numerical results of the distribution of the electric fields and power flows for the cloaks with a square outer boundary and a circular inner boundary. In Fig. 4a, the phase fronts of incident waves are parallel to the sides of the cloak. When the waves pass through the cloak, the cloaking effect is very clear as expected, although the cloak boundary possesses sharp corners. From Fig. 4a, the plane wave is almost unaltered, as if no scatterer were present. Inside the cloaking material, the power-flow lines and phase fronts are bent smoothly around the target. The fields are smoothly excluded from the interior region with the minimal scattering in any directions. Fig. 4b shows the electric fields and power-flow lines when the cloak is rotated by an angle of 45°. In such a case, the cloaking effect is also obvious, although the

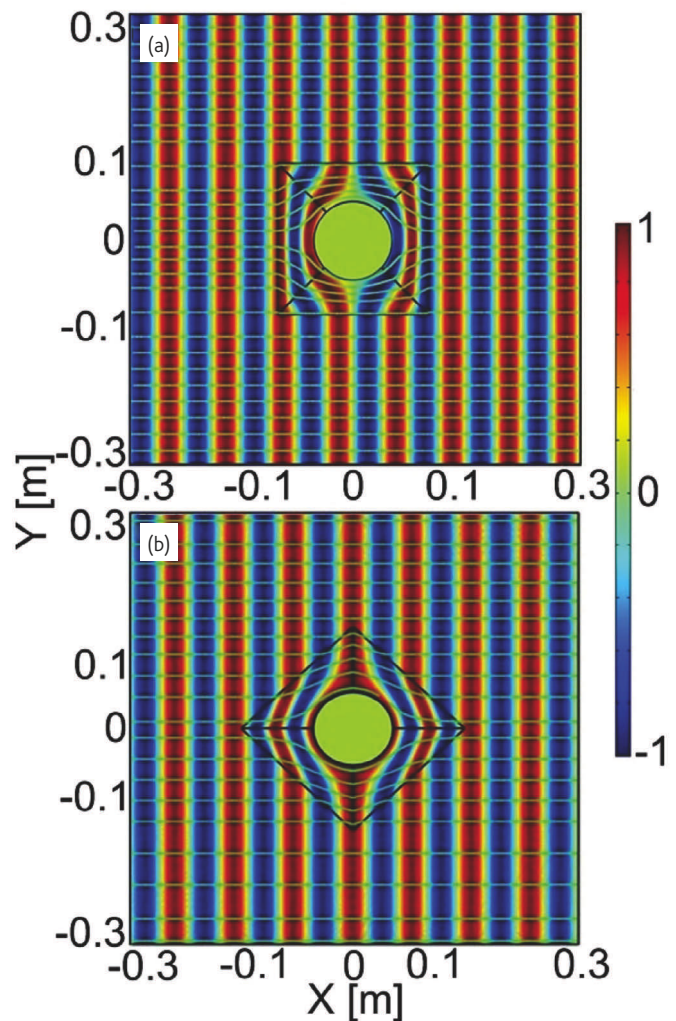


Fig. 4 The distributions of electric fields and power-flow lines for the invisible cloaks with different inner and outer boundaries. (a) The square outline of the cloak is parallel to the x direction. (b) The square outline of the cloak is rotated by $\pi/4$ with respect to the x direction.

phase fronts of incident waves are not parallel to any sides of the cloak boundary.

EM concentrators

The concept of EM concentrator was first proposed by Rahm *et al.*³⁰; it can concentrate electromagnetic waves into a small enclosed region. The concept of EM concentrators can be used to design efficient receiving antennas and efficient solar cells, etc. Arbitrarily-shaped EM concentrators were later presented using the coordinate transformation by using NURBS in representation of the geometrical boundary⁵⁴. Closed-form formulas for the transformation optics of the arbitrarily-shaped concentrators were obtained, and a square concentrator could be used to amplify plane waves⁵⁴.

Fig. 5 demonstrates the numerical result of a heart-shaped concentrator⁵⁴, when the TE wave propagates from the left to the

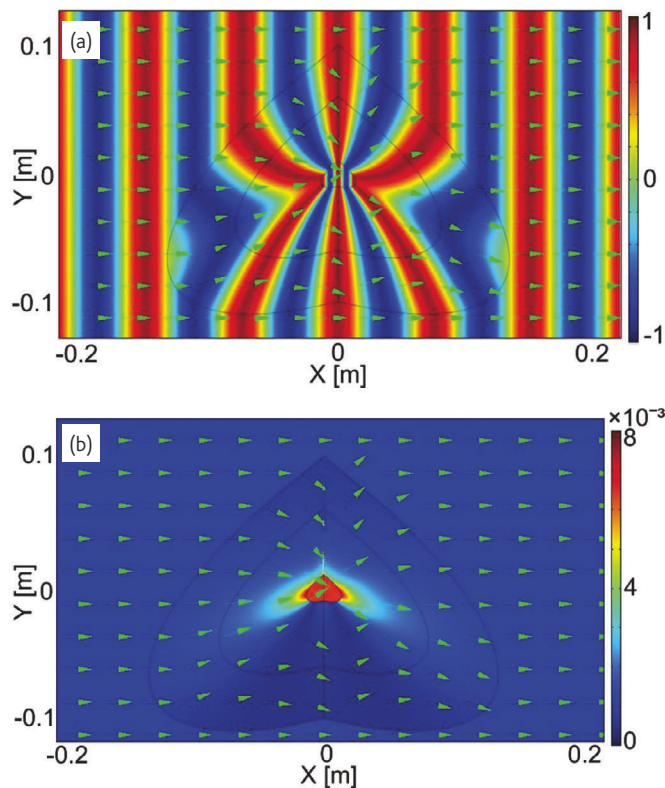


Fig. 5 (a) The electric field distributions and power-flow lines for a heart-shaped concentrator. The incident plane waves propagate from the left to the right. (b) Power flow distributions for the heart-shaped concentrator. Much stronger power flow enhancements can be observed.

right. The outer boundary of the concentrator is described by the Bézier curve. The ratio among the principal radii of the three “hearts” is 1:6:10. Clearly, the field intensities are strongly enhanced in the inner region of the concentrator. There are no reflected waves outside the concentrator due to the inherent impedance matching in the method of optical transformation. Fig. 5b illustrates the power-flow intensity distribution of the plane wave. It is obvious that the field intensities are strongly enhanced in the inner region within the concentrator material.

Similar to the cloak with non-conformal boundaries, one can also design EM concentrator with irregular boundaries⁵¹. Fig. 6 demonstrates the numerical results of the electric field and power-flow lines for concentrators with non-conformal inner and outer boundaries. It is obviously shown that the fields are concentrated from the larger circular region into the smaller one in both cases, which leads to enhanced field intensities inside the EM concentrator.

EM-wave converters

An approach to convert cylindrical waves to plane waves in a short range using the optical transformation was proposed^{54–55}. This can be used either as a four-beam antenna or a compact range for near-field measurement of plane waves. Fig. 7 illustrates the

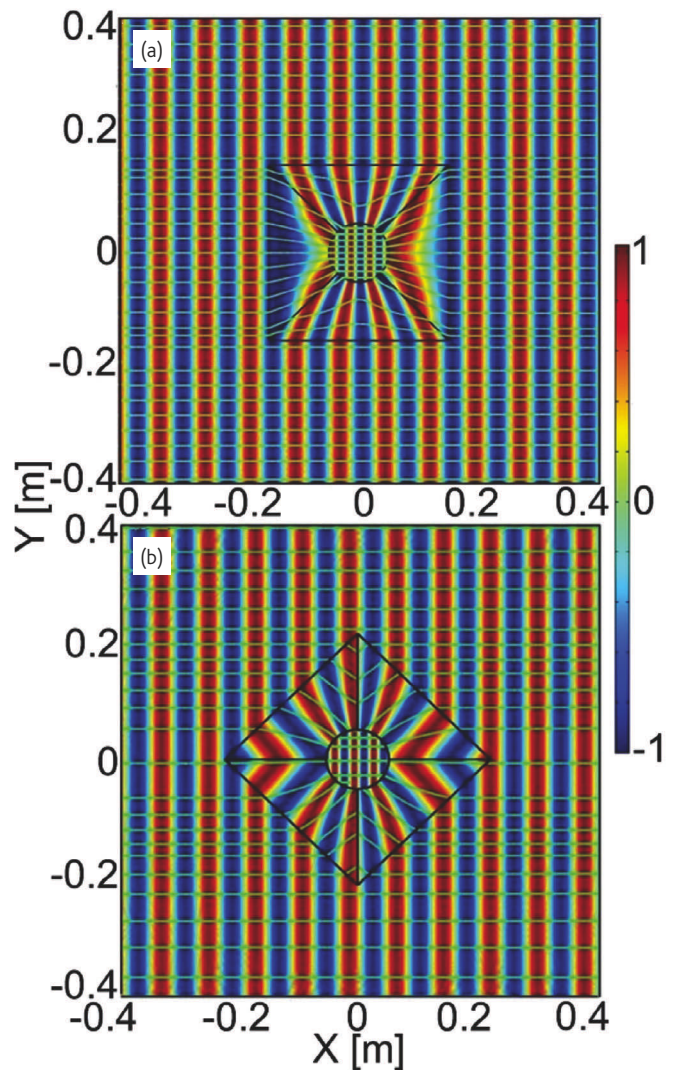


Fig. 6 The distributions of electric fields and power-flow lines for the concentrators with non-conformal inner and outer boundaries. (a) The square outline of the concentrator is parallel to the x direction. (b) The square outline of the concentrator is rotated by $\pi/4$ with respect to the x direction.

structure of the EM-wave converter and the distributions of electric fields inside and outside the converter. When the cylindrical waves propagate through the conversion metamaterial layer, four beams of plane waves emerge in the surrounding space. Hence, in a very short range, the cylindrical waves emitted from the line source are converted to plane waves in four directions. Clearly, the scattering effect at four corners of the square is quite small. In other words, the converter provides highly-directive radiation beams to four orthogonal directions, hence it can be used to design directive antennas or wave collimators⁶².

Similarly, the coordinate transformation theory was employed to realize substrates that can modify the emission of an embedded source⁵⁶. With proper transformations the energy radiated by a source

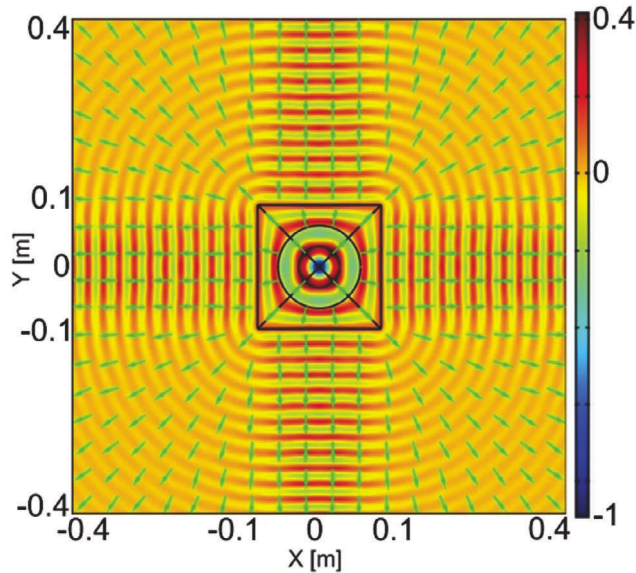


Fig. 7 The distributions of electric fields and power-flow lines for the conversion from cylindrical waves to plane waves via the finite embedded optical transformation.

embedded in these space variant media will be concentrated in a narrow beam. The technique of optical transformations is a powerful approach for highly directive antenna designs⁵⁷⁻⁵⁹.

EM-wave bending

Rahm *et al.*⁶⁰ expanded the class of transformation optical structures by introducing embedded coordinate transformations, which allow the EM waves to be shifted and split. The optical transformation can also be used to bend EM waves to the desired directions inside a waveguide or in free space without any reflections (or with tiny reflections) by designing proper inhomogeneous and anisotropic materials⁶¹⁻⁶⁶.

One can employ the finite embedded optical transformation to realize the wave bending. Define a mapping from the original space to the transformed space as

$$x' = x \cos \frac{\theta y}{h},$$

$$y' = x \sin \frac{\theta y}{h},$$

$$z' = z,$$

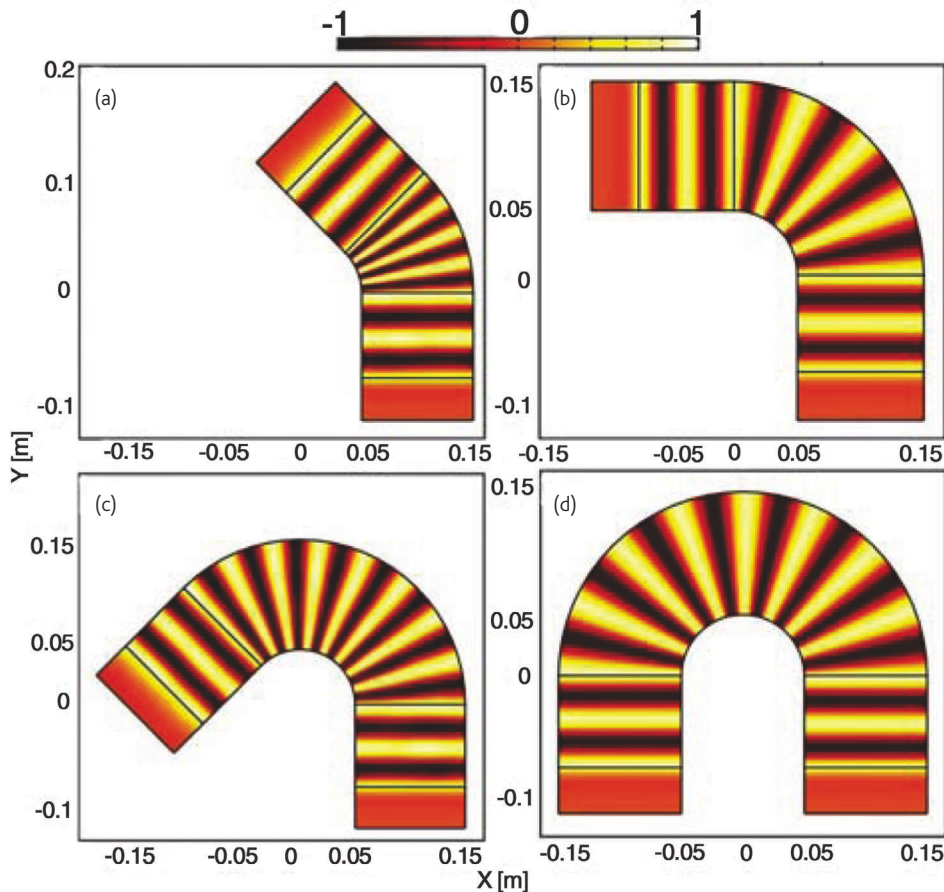


Fig. 8 The distribution of magnetic fields (components) inside the waveguide bends. (a) $\theta = \pi/4$ and $h = 4\lambda_0$; (b) $\theta = \pi/2$ and $h = 4\lambda_0$; (c) $\theta = 3\pi/4$ and $h = 8\lambda_0$; (d) $\theta = \pi$ and $h = 8\lambda_0$. λ_0 is the free-space wavelength.

where θ is the radian of the bending angle and h is an optional variable. Fig. 8 illustrates the magnetic-field distributions inside the waveguide bends with different bending angles and different values of h ⁶⁶. It is clear that incident waves travel through the waveguide bends with less reflection and keep their original field patterns in all cases.

The arbitrary wave-bending structure have been designed and analyzed using the optical transformation⁶⁶, which is composed of simple and realizable metamaterials. The reduced-parameter wave bender is uniaxial, and hence easy to realize using artificial structures. When such a “wave bender” is filled inside metallic waveguide bends, the incident waves will be guided through the bends with very small reflections. When such a “wave bender” is placed in the air, the incident waves will be bent to any designed directions. The discrete wave benders also have good performance in the wave bending.

Other optical transformation devices

The optical transformation can also be used to design a large number of other devices, such as high-performance antennas, EM-beam modulators, superscatterer, imaging devices, etc.⁶⁷⁻⁷⁶. As an example, we introduce a lens antenna realized by a discrete embedded optical transformation⁶⁷, which could find important applications in communications and other EM engineering. Using the discrete embedded optical transformation, a layered high-gain lens antenna has been designed. All layers of the lens antenna are composed of homogeneous and uniaxially anisotropic metamaterials, which are simple and realizable. When the layered lens is embedded in a horn antenna, the lens antenna provides a high-directivity radiation beam⁶⁷.

When the layered lens is placed in free space, the EM beam modulation can be realized⁶⁸.

While applying the method of discrete optical transformation, one divides the physical and virtual spaces into several layers in the same way⁶⁷. For each layer, one defines a separate mapping between the virtual space and the physical space. Hence the actual “physical space” is the staircase approximation of the trapezium obtained by stacking rectangles on top of each other. At this point, the larger the layer number is, the more accurate the transformation will be. As a comparison, the lens designed by continuous optical transformation is composed of inhomogeneous and strongly anisotropic metamaterials, which are much more difficult to manipulate in real applications.

To reveal the performance of the proposed lens antennas⁶⁷, full-wave simulation results are shown in Fig. 9. Fig. 9a illustrates the distribution of electric fields inside and outside the lens antenna designed by continuous optical transformation. Fig. 9b shows the electric-field distributions of the lens antenna designed by discrete optical transformation, in which the size of PEC horn and the number of layers are the same as those in Fig. 9a. Compared to Fig. 9a, fewer reflections are observed inside the lens antenna in Fig. 9b. Clearly, almost all EM powers are concentrated in a beam of plane waves in the front of the lens antennas.

For a comparison with the conventional lens, a horn antenna filled with a collimating lens is designed, which is made of traditional dielectrics in accordance with the method explained in⁷⁷. Fig. 9c demonstrates the electric field distribution inside and outside the

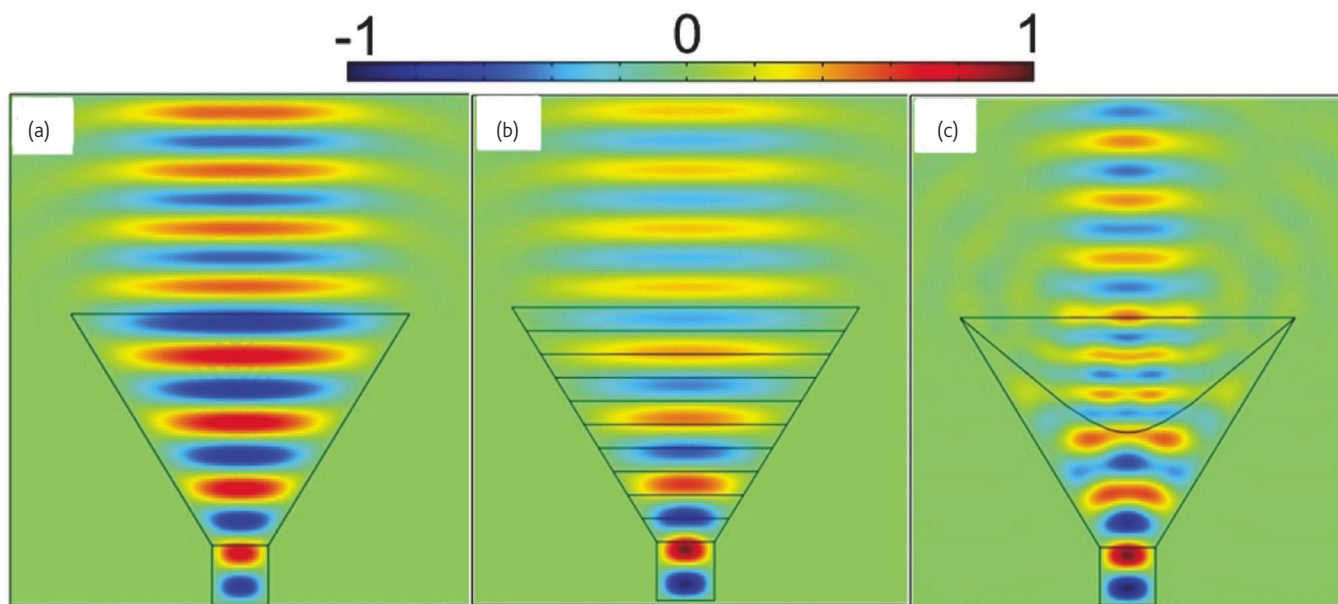



Fig. 9 The distribution of normalized electric fields inside and outside the lens structures, which are placed in a PEC horn antenna, under the excitation of a line-current source. (a) The lens is designed by continuous optical transformation. (b) The lens is designed by discrete optical transformation. (c) The collimating lens is made of regular dielectric.

regular lens antenna, in which the size of the PEC horn is the same as that in earlier lens antennas. Clearly, the newly proposed lens antennas based on the optical transformation have much better performance than the conventional lens. The directivity of the transformation lens antennas is above 30 and the regular lens antenna is about 20.

Summary

In this paper, we introduced several categories of transformation optical devices that have been developed in the past years. The optical transformation enables the direct manipulation of EM waves, and therefore it can be regarded as a powerful design tool for novel

microwave and optical devices. The optical transformation is expected to have further impact on real-life applications. 

Acknowledgments

This work was supported in part by a key project of the National Science Foundation of China, the Natural Science Foundation of Jiangsu Province under Grant No. BK2008031, the National Basic Research Program (973) of China under Grant No. 2004CB719802, the National Science Foundation of China under Grant Nos. 60871016, 60671015, and 60621002, and in part by the 111 Project under Grant No. 111-2-05. WXJ acknowledges the support from Graduate Innovation Program of Jiangsu Province under grant No. CX08B_074Z, and the Scientific Research Foundation of Graduate School of Southeast University under grant No. YBJJ0816.

References

- Pendry, J. B., *et al.*, *Science* (2006) **312**, 1780.
- Ward, A. J., and Pendry, J. B., *J. Mod. Opt.* (1996) **43**, 773.
- Leonhardt, U. and Philbin, T. G., *New J. Phys.* (2006) **8**, 247.
- Leonhardt, U., *New J. Phys.* (2006) **8**, 118.
- Leonhardt, U., *Science* (2006) **312**, 1777.
- Schurig, D., *et al.*, *Opt. Express* (2006) **14**, 9704.
- Cummer, S. A., *et al.*, *Phys. Rev. E* (2006) **74**, 036621.
- Schurig, D., *et al.*, *Science* (2006) **314**, 977.
- Zolla, F., *et al.*, *Opt. Lett.* (2007) **32**, 1069.
- Huang, Y., *et al.*, *Opt. Express* (2007) **15**, 11133.
- Cai, W., *et al.*, *Nat. Photon.* (2007) **1**, 224.
- Cai, W., *et al.*, *Appl. Phys. Lett.* (2007) **91**, 111105.
- Yan, M., *et al.*, *Opt. Express* (2007) **15**, 17772.
- Chen, H., *et al.*, *Phys. Rev. Lett.* (2007) **99**, 063903.
- Yan, M., *et al.*, *Phys. Rev. Lett.* (2007) **99**, 233901.
- Zhang, B., *et al.*, *Phys. Rev. B* (2007) **76**, 121101.
- Chen, H., *et al.*, *Phys. Rev. B* (2007) **76**, 241104.
- Ruan, Z. C., *et al.*, *Phys. Rev. Lett.* (2007) **99**, 113903.
- Ozgun, O., and Kuzuoglu, M., *Micro. Opt. Tech. Lett.* (2007) **49**, 2386.
- Greenleaf, A., *et al.*, *Phys. Rev. Lett.* (2007) **99**, 183901.
- Ozgun, O., and Kuzuoglu, M., *IEEE Micro. Wirel. Comp. Lett.* (2007) **17**, 754.
- Teixeira, F. L., *IEEE Antennas Wireless Prop. Lett.* (2007) **6**, 163.
- Chen, H., and Chan, C. T., *Appl. Phys. Lett.* (2007) **90**, 241105.
- Kong, F., *et al.*, *Appl. Phys. Lett.* (2007) **91**, 253509.
- Jiang, W. X., *et al.*, *J. Phys. D: Appl. Phys.* (2008) **41**, 085504.
- Kwon, D.-H., and Werner, D. H., *Appl. Phys. Lett.* (2008) **92**, 113502.
- Ma, H., *et al.*, *Phys. Rev. A* (2008) **77**, 013825.
- Kwon, D.-H., and Werner, D. H., *Appl. Phys. Lett.* (2008) **92**, 013505.
- Piegl, L., and Tiller, W., *The NURBS Book*, 2nd ed. Springer-Verlag, New York (1996).
- Rahm, M., *et al.*, *Photo. Nano. Fund. Appl.* (2008) **6**, 87.
- Jiang, W. X., *et al.*, *Phys. Rev. E* (2008) **77**, 066607.
- Ma, H., *et al.*, *Opt. Express* (2008) **16**, 15449.
- Yan, W., *et al.*, *New J. Phys.* (2008) **10**, 043040.
- You, Y., *et al.*, *Opt. Express* (2008) **16**, 6134.
- Ma, H., *et al.*, *Phys. Rev. E* (2008) **78**, 036608.
- Nicolet, A., *et al.*, *Opt. Lett.* (2008) **33**, 1584.
- Li, J., and Pendry, J. B., *Phys. Rev. Lett.* (2008) **101**, 203901.
- Zhang, P., *et al.*, *Opt. Express* (2008) **16**, 3161.
- Leonhardt, U., and Tyc, T., *Science* (2009) **323**, 110.
- Liu, R., *et al.*, *Science* (2009) **323**, 366.
- Jiang, W. X., *et al.*, *Appl. Phys. Lett.* (2008) **93**, 194102.
- Green, A., *et al.*, *Phys. Rev. Lett.* (2008) **101**, 220404.
- Cai, W., *et al.*, *Opt. Express* (2008) **16**, 5444.
- Yan, M., *et al.*, *Appl. Phys. Lett.* (2008) **93**, 021909.
- Xu, X., *J. Phys. D: Appl. Phys.* (2008) **41**, 215504.
- Luo, Y., *et al.*, *J. Phys. D: Appl. Phys.* (2008) **41**, 235101.
- Luo, Y., *et al.*, *Phys. Rev. B* (2008) **78**, 125108.
- Gallina, I., *et al.*, *Micro. Opt. Tech. Lett.* (2008) **50**, 3186.
- Luo, Y., *et al.*, *Appl. Phys. Lett.* (2008) **93**, 033504.
- Chen, H., *et al.*, *Opt. Express* (2008) **16**, 14603.
- Yu, G. X., *et al.*, *Eur. Phys. J. Appl. Phys.* (2008) **44**, 181.
- Li, C., *et al.*, *Opt. Express* (2008) **16**, 19366.
- Jiang, W. X., *et al.*, *Appl. Phys. Lett.* (2008) **92**, 264101.
- Lin, L., *et al.*, *Opt. Express* (2008) **16**, 6815.
- Jiang, W. X., *et al.*, *Appl. Phys. Lett.* (2008) **92**, 261903.
- Zhang, J., *et al.*, *Progr. Electro. Res.* (2008) **81**, 437.
- Zhang, J., *et al.*, *Opt. Express* (2008) **16**, 10962.
- Kundtz, N., *et al.*, *Opt. Express* (2008) **16**, 21215.
- Leonhardt, U. and Tyc, T., *New J. Phys.* (2008) **10**, 115026.
- Rahm, M., *et al.*, *Phys. Rev. Lett.* (2008) **100**, 063903.
- Rahm, M., *et al.*, *Opt. Express* (2008) **16**, 11555.
- Kwon, D.-H., and Werner, D. H., *New J. Phys.* (2008) **10**, 115023.
- Roberts, D. A., *et al.*, *Appl. Phys. Lett.* (2008) **93**, 251111.
- Donderici, B., and Teixeira, F. L., *IEEE Micro. Wirel. Comp. Lett.* (2008) **18**, 233.
- Huangfu, J., *et al.*, *J. Appl. Phys.* (2008) **104**, 014502.
- Jiang, W. X., *et al.*, *Phys. Rev. E* (2008) **78**, 066607.
- Jiang, W. X., *et al.*, *Appl. Phys. Lett.* (2008) **93**, 221906.
- Xu, X., *et al.*, *New J. Phys.* (2008) **10**, 115027.
- Wang, W., *et al.*, *Opt. Express* (2008) **16**, 21142.
- Kwon, D.-H., and Werner, D. H., *Opt. Express* (2008) **16**, 18731.
- Yang, T., *et al.*, *Opt. Express* (2008) **16**, 18545.
- Zhang, X., *et al.*, *Opt. Express* (2008) **16**, 11764.
- Yan, M., *et al.*, *Phys. Rev. B* (2008) **78**, 125113.
- Kildishev, A. V., and Shalaev, V. M., *Opt. Lett.* (2008) **33**, 43.
- Chen, H., and Chan, C. T., *Phys. Rev. B* (2008) **78**, 054204.
- Tsang, M., and Psaltis, D., *Phys. Rev. B* (2008) **77**, 035122.
- Kraus, J. D., and Marhefka, R. J., *Ant. For. All Appl.*, 3rd ed., McGraw-Hill, New York (2002).

Phononic crystals and acoustic metamaterials

Phononic crystals have been proposed about two decades ago and some important characteristics such as acoustic band structure and negative refraction have stimulated fundamental and practical studies in acoustic materials and devices since then. To carefully engineer a phononic crystal in an acoustic “atom” scale, acoustic metamaterials with their inherent deep subwavelength nature have triggered more exciting investigations on negative bulk modulus and/or negative mass density. Acoustic surface evanescent waves have also been recognized to play key roles to reach acoustic subwavelength imaging and enhanced transmission.

Ming-Hui Lu, Liang Feng* and Yan-Feng Chen†

National Laboratory of Solid-State Microstructures and Department of Materials Science and Engineering, Nanjing University, 210093, China

**Present address: Department of Electrical and Computer Engineering, University of California, San Diego, CA, 92093, USA*

†Email: yfchen@nju.edu.cn

Classical waves, including elastic waves (acoustic waves) and electromagnetic waves (optical waves and microwaves), are described by conventional wave-propagation functions. Elastic waves were the first waveforms to be understood in condensed matter and have a wide range of applications from industry to defense, from healthcare to entertainment. In 1987^{1,2}, the photonic crystal was proposed to describe the propagation of optical waves in refraction index-modulated periodic structures analogous to the propagation of electrons in real crystals. This situation recalls the classical work by Brillouin³. Brillouin considered elastic waves in periodic strings, electromagnetic waves in electrical circuits, and electrons in crystals as a system, resulting in some important common concepts, such as the Brillouin zone, band gap, etc., which are generally shared by the various forms of waves: electrons as scalar waves, optical waves

as vector waves, and elastic waves as tensor waves. Following on from photonic crystals, the concept of phononic crystals (PCs) was conceived with elastic waves propagating in periodic structures modulated with periodic elastic moduli and mass densities⁴.

Over the past two decades, the study of elastic waves in artificially structured materials has proved to be of great interest due to their novel and unique properties and effects, and their potential for acoustic applications in everyday life^{4–30}. A periodic structure with an elastic modulus and mass density modulated on a scale comparable to the wavelength of acoustic waves results in PCs that possess a number of important properties, such as band gaps^{4–6}, band edge states⁷, and the ability to slow the velocity of sound (slow wave effect)^{8,9}, analogous to electron propagation in real crystals. Furthermore, by creating artificially designed structures on a deep subwavelength scale, artificial acoustic ‘atoms’ can be purposely engineered into PCs to dramatically

change the excitation and propagation of acoustic waves, and thus give rise to subdiffraction-limited resolution and its related myriad novel effects, such as negative refraction^{10–19}, negative elastic modulus^{20–22}, and negative mass density^{23–27}. Another way to approach subdiffraction-limited resolution is to create acoustic surface waves that are confined two-dimensionally in a single acoustic ‘atom’ layer with such engineered PCs. The in-plane subwavelength properties are inherently associated with the evanescent nature of acoustic surface waves along the third dimension. These state-of-the-art, artificially structured bulk and surface PCs are called acoustic metamaterials (AMs). Acoustic metamaterials are a newly emerging field, which have inherently abnormal and interesting physical effects that are important to basic research, and offer potential for applications that might revolutionize acoustic materials.

A universally accepted definition of AMs does not yet exist. Some researchers define a metamaterial as an artificially structured medium that shows some novel and counterintuitive effects for wavelengths much greater than their periodicities. Others extend the concept of metamaterials to include PCs. We subscribe to the latter view, and hence have tried in this review to describe AMs and PCs in terms of structural evolution, and to provide some detailed understanding of the methods involved.

The phononic crystal and its novel properties

Phononic crystals are artificial periodic composite materials consisting of periodically distributed individuals (single acoustic functional scatterer) in a matrix with high impedance contrast of mass densities and/or elastic moduli, which can give rise to new acoustic dispersions and band structures due to the periodic Bragg scattering as well as localized Mie scatterings from the individuals. PCs can be classified into two categories: acoustic phononic crystals (APCs) with a fluid matrix, and elastic phononic crystals (EPCs) with an elastic solid matrix. In this article, we will mainly focus on APCs since most research has been conducted in this field.

The formation of band structures in PCs has been much investigated in physics, and comparisons made with other waves: while the electrons in a semiconductor can only occupy certain energy bands, a PC allows acoustic waves in specific frequency ranges to travel through via the pass band; other frequencies are inhibited by the band gap. This offers a very precise means to control and manipulate phonons, sound, and other waves.

Research into PCs initially focused on calculating the band structure and its mechanism of formation. Creating a PC with a full band gap, requires designing different topological structures with different geometric individuals or with different periodic lattices. The band structures of PCs can also be engineered and tailored by varying the filling ratio and using new materials with different elastic constants^{31, 32}. In general, individuals with a low mass density in a matrix with a high mass density readily form a full band gap, and

a high contrast in acoustic speeds also results in a full band gap. In the case of three-dimensional PCs, face-centered cubic structures more easily form a full band gap than body-centered cubic and PCs structures^{31, 32}.

In order to design PCs to satisfy specific requirements, several calculation methods have been developed, including plane wave expansion (PWE)^{3, 33}, the transfer matrix method (TMM)³⁴, multiple scattering theory (MST)^{35–37}, finite-difference time-domain (FDTD)^{38, 39}, and the finite element method (FEM)⁴⁰. All these methods have particular advantages and disadvantages. Recently, genetic algorithms have been found to provide a better approach for searching optimal structural parameters to design PCs^{41, 42}.

Careful design with accurate calculation of band structures has enabled many novel effects to be achieved in PCs. When PCs have some point defects and line defects within the band gap, elastic waves localize in the point defect cavity, or propagate in the line defects, similar to light in photonic crystals⁴³. In addition, the dynamic effects of PCs have also attracted much attention. Chan *et al.*^{44, 45} explored the tunneling effect in the band gap of a three-dimensional APC, and observed a supersonic velocity and anomalous phase shift associated with the resonant phenomena of slow waves. Recently, Zhang and Liu⁴⁶ have found that the maximum transmission and beating effect of acoustic waves occurs near the Dirac point in a two-dimensional APC. The transmission of acoustic waves through an APC is inversely proportional to its thickness, different from the tunneling effect, which is attenuated exponentially in the band gap of an APC.

Moreover, the focus of research on PCs has been also transferred from the band gap to the band edge states, where a number of new effects exist, such as bending of acoustic waves, strong dispersion of group velocity, and the superprism phenomenon^{8, 9}. More importantly, negative refraction, which was first proposed in optical metamaterials⁴⁷, has been achieved in acoustics both experimentally and theoretically by carefully designing acoustic dispersion in the Brillouin zones of APCs^{11, 14}. Acoustic negative refraction, and the resulting acoustic superlens effect, has become one of the most active topics of APC research, attracting the interest of many scientists^{10–19}. Negative refraction of acoustic waves in APCs occurs via two mechanisms: (i) strong Bragg scattering near the Brillouin zone boundaries in the first band without showing a negative refractive index¹⁴; (ii) band folding in the second band, causing backward negative refraction with a backward wave vector, which is similar to an AM with equivalent double-negative parameters¹⁶. Due to anisotropy, the propagation of acoustic waves in APCs is more complex than that in isotropic AMs as shown in Fig. 1¹⁶. Using the negative refraction effect, we used an APC to focus an acoustic wave in order to achieve acoustic point source imaging^{14–18}. As there is only one longitudinal polarization for acoustic waves in the fluid, the birefringence phenomenon can never occur for purely longitudinal acoustic waves. However, we have

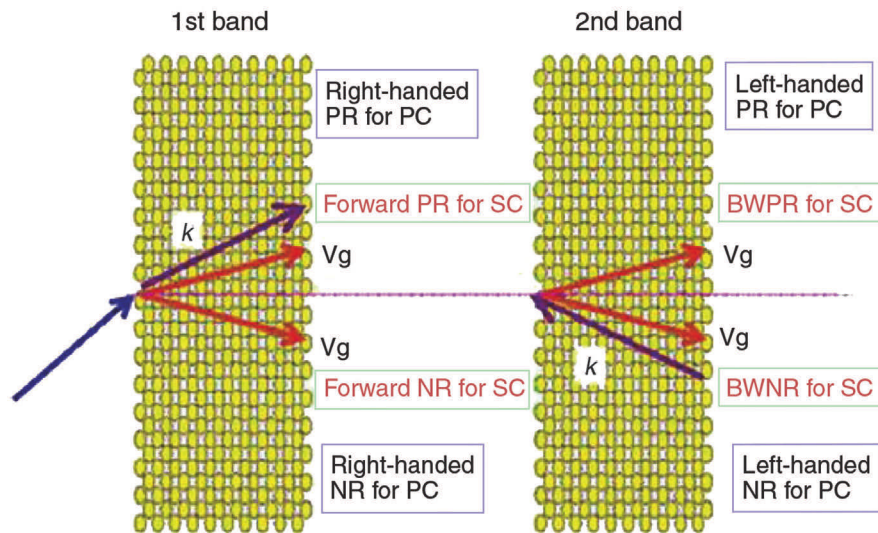


Fig. 1 Illustration of refractions in both the first and second bands of PCs, as well as their counterparts in photonic crystals.

successfully achieved negative birefracton and double-focusing of acoustic waves in an APC due to the overlap of two high Bloch bands as shown in Fig. 2¹⁷. In addition, tunable negative refraction and tunable acoustic imaging are also of great interest. By rotating the square rod inclusions of an APC, we were able to modulate the band structure and dispersion of acoustic waves in the APC, and then tune the refraction of acoustic waves from positive to negative¹⁸.

In order to study the propagation of acoustic waves in an APC, we must understand the nature of the eigen modes of the wave in the APC. As Bloch⁴⁸ pointed out, a wave propagating in a periodic structure is different from a plane wave only by a periodic modulation. In other words, the wave in a PC is a Floquet–Bloch wave, which is the superposition of many plane waves from all individuals. Hence, the velocity of the Bloch wave is different from that of each plane wave, and instead there are three velocities: group velocity, energy velocity, and phase velocity. Sakoda³⁰ has proved that the energy velocity of a Bloch wave is equivalent to the group velocity. Therefore we can express the velocity of the energy flow as the gradients of the equifrequency surface (EFS) as follows, where the direction of the normal line indicates the direction of propagation of the wave:

$$\vec{v}_e = \frac{c_0^2}{\omega_{n,\vec{k}} \vec{G}} \sum (\vec{k} + \vec{G}) u_G^2(\vec{k}, \omega_{n,\vec{k}}) = \vec{v}_g = \nabla_{\vec{k}} \omega \quad (1)$$

The occurrence of negative refraction thus suggests that the frequency increases as the EFSs assume a concave form. Hence the propagation of acoustic waves in an APC can be understood by examining the acoustic band structure and the EFS.

Development of PC research has shown that these materials have a wide range of potential applications. PCs can be used for sound insulation, shockproofing, slow wave effects, acoustic wave filtering⁴⁹,

as acoustic wave guides⁵⁰, for collimation of acoustic waves and directed beaming^{51, 52}, and in particular for high-resolution acoustic imaging^{53, 54}. Recently a PC has also been used to achieve acoustic cloaking via transformation acoustics⁵⁵.

Acoustic metamaterials

Although we introduced PCs by drawing an analogy with electrons in real crystals in which the atoms at crystal lattice sites are determined 'naturally', we can not only preserve the lattice symmetry of PCs but also engineer acoustic 'atoms' in the unit cells of PCs. It is therefore possible to extend the concept of PCs to the 'atomic' scale and design and fabricate new types of artificial acoustic materials called AMs in which an individual resonance from single 'atoms' and its interaction with the Bragg resonance from the lattice symmetry can lead to novel and exotic properties.

The optical counterpart of an AM is an optical metamaterial, which can be regarded as an effective medium with simultaneously negative permittivity and permeability, and thus an effectively negative refractive index. Optical metamaterials have many striking effects compared to normal refractive index material, such as left-handed backward effects, negative refractions, superlens, inverse Doppler effects, inverse Cherenkov effects, etc⁵⁶. Correspondingly it is highly desirable to achieve simultaneously negative mass density and elastic modulus as well as the resulting negative index with AMs. Although an equivalent negative index can be obtained with conventional PCs^{13–17}, the high anisotropy and lattice constant limited resolution of such materials may hinder their actual application. Thus, it is of great interest to engineer material properties on the atomic scale. Obviously, the artificial 'atom' dimension will greatly expand the properties and effects of a PC with simple 'atoms', and some abnormal phenomena beyond the well-known space periodicity related effects have been

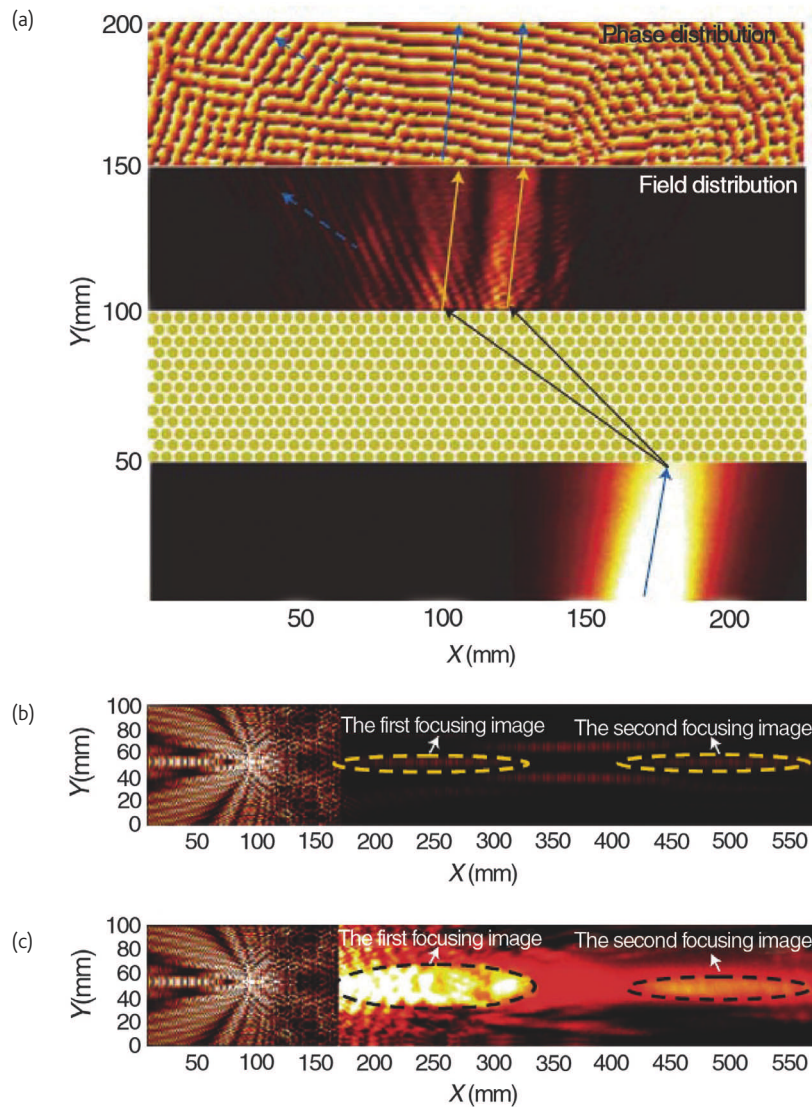


Fig. 2 (a) The spatial distributions of the intensity and the phase of the acoustic pressure field at 7° incidence and 73 kHz, which clearly shows the negative bi-refraction occurring. (b) The FDTD simulation of the field distribution of a point source 15 mm in front of the sonic crystal and its focusing images through the sonic sample with 16 layers at 73 kHz. (c) The experiment spatial intensity and phase distribution of its focusing images are measured at 73 kHz.

keenly anticipated. Analogous to optical metamaterials, AMs also show many intriguing phenomena for sound waves such as low-frequency band gap, negative refraction, superlensing, localized confined waves, etc.

For most PCs, conventional acoustic 'atoms' have neither a negative mass density nor a negative elastic modulus. For AMs, however, the special unit cell with locally resonant elements can be assigned as an artificial 'atom' with exotic effective acoustic parameters under the long-wavelength approximation. Various artificial 'atoms' have their own resonant frequencies and features. State-of-the-art artificial acoustic 'atoms' were classified as 'intrinsic'^{20, 21} and 'inertial'^{22–25} by Fok *et al.*⁵⁷ as the resonant frequencies of 'atoms' are dependent on the materials' intrinsic acoustic properties (phase velocity), or

correlated with the scale and geometry of the 'atoms', respectively. However, based on such a definition of 'atoms', these two different cases cannot be distinguished independently since 'atoms' can be designed to be sensitive both to geometries and intrinsic material properties.

There are several ways to design acoustic 'atoms' in AMs. Deep subwavelength local resonators with their own mechanical oscillator can serve as these artificial 'atoms' and exhibit new effective elastic parameters (i.e. modulus and mass density; be singly or simultaneously negative) and other exotic acoustic properties based on the long-wavelength approximation (see Fig. 3)^{20–26}. Negative elastic parameters can be obtained at a certain resonant frequency range if a proper local resonator is built into the structures. With the long-wavelength

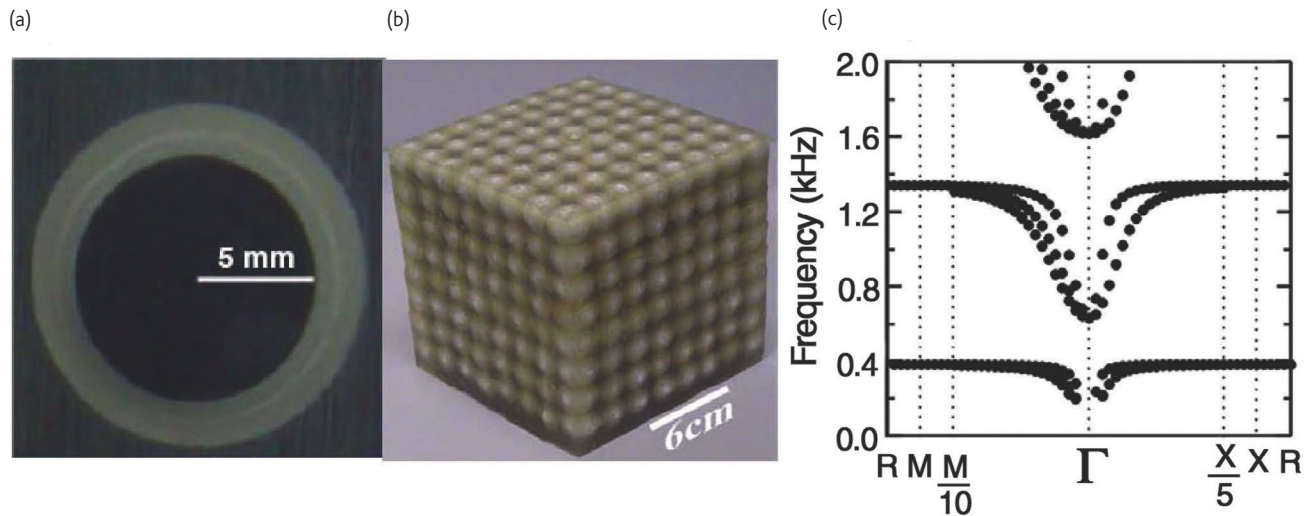


Fig. 3 (a) Cross section of a coated lead sphere that forms the basic man-made 'atom' with local resonance; (b) Unit cells arranged in an $8 \times 8 \times 8$ sonic crystal, which is the block of acoustic metamaterial that was experimentally tested; (c) A simple cubic structure of coated spheres from 200 to 2000 Hz. Three modes (two transverse and one longitudinal) are distinguishable in the $[110]$ direction, to the left of the Γ point. The two transverse modes are degenerate along the $[100]$ direction, to the right of the Γ point. Note the expanded scale near the Γ point.

approximation, the effective elastic parameters can be retrieved by further analysis of wave-scattering coefficients. These 'atoms' can locally and globally show either dipolar resonance or monopolar resonance. The resonance of some cylindrical and spherical resonance 'atoms' can be derived analytically with the coherent-potential approximation (CPA)^{58, 59}. Three-component PCs with locally cylindrical and spherical resonant structures have also been experimentally proved to exhibit a negative mass density due to dipolar resonance²⁷. For AMs consisting of air bubbles in water, different orders of Mie scatterings can lead to monopolar resonance and dipolar resonance at different frequencies, corresponding to negative effective bulk modulus and negative effective mass density, respectively²³. Recently, an effective negative bulk modulus at monopolar resonant frequency has been achieved by an AM consisting of an array of subwavelength Helmholtz resonators (HRs)^{22, 23, 26, 60, 61}. According to the transmission line theory⁶², some AMs with subwavelength HRs can be designed to realize backward effects such as left-handed transmission. Here, we reveal a low-frequency band gap due to monopolar resonance with negative stiffness in an AM consisting of HRs (Fig. 4). By using a two-step homogenization approach, the effective mass density and effective bulk modulus can be analytically derived for AMs of HRs in fluid and the format of these analytical solutions can thus be compared to those for three-component locally resonant elements⁶³. In addition, using the long-wavelength approximation, the effective mass density and elastic modulus can also be retrieved from the transmission and reflection coefficients^{64, 65}.

The effective negative refractive index of AMs is given by:

$$n = \sqrt{\frac{B_0 \rho_e}{\rho_0 B_e}}. \quad (2)$$

Here n is the refractive index, B_0 and ρ_0 are the reference bulk modulus and the reference mass density, respectively, and B_e and ρ_e are the effective bulk modulus and effective mass density, respectively. Although a negative index requires both negative modulus and mass density, the negative refraction of an acoustic energy flow can occur without double negativities. Similar to electromagnetically induced transparency⁶⁶, negative group velocity can be achieved with loss associated with coupling between two resonant modes⁶⁷. Two resonators with the same polar resonance can thus realize negative refractions of acoustic waves as long as the coupling of these resonances is strong enough. This offers a more feasible approach to construct AMs with monopolar resonant 'atoms' since it is in practice very difficult to create dipolar resonant elements.

Generally because of the deep subwavelength nature of its local resonant elements, an AM can be regarded as an isotropic and homogeneous material showing a local resonant response globally. As the artificial 'atoms' always contain mechanical oscillators with the proper resonant frequency, the AM is not a static acoustic material but a dynamically effective medium even though the size of the 'atoms' is comparably small. Although conventional PCs can also show equivalent negative elastic parameters^{68, 69}, as the validity of the effective-medium approximation can be rigorously analyzed via the single-mode approximation⁶⁹, AMs clearly provide greater opportunities to realize more fascinating acoustic phenomena by engineering materials through fundamental building blocks. Both acoustic and optical artificial metamaterials are unprecedented in nature and exhibit novel, abnormal and even counterintuitive features; the subwavelength characteristics of these metamaterials may well reduce the size and enhance the integration of devices, overcoming the deficiencies of PCs and photonic crystals.

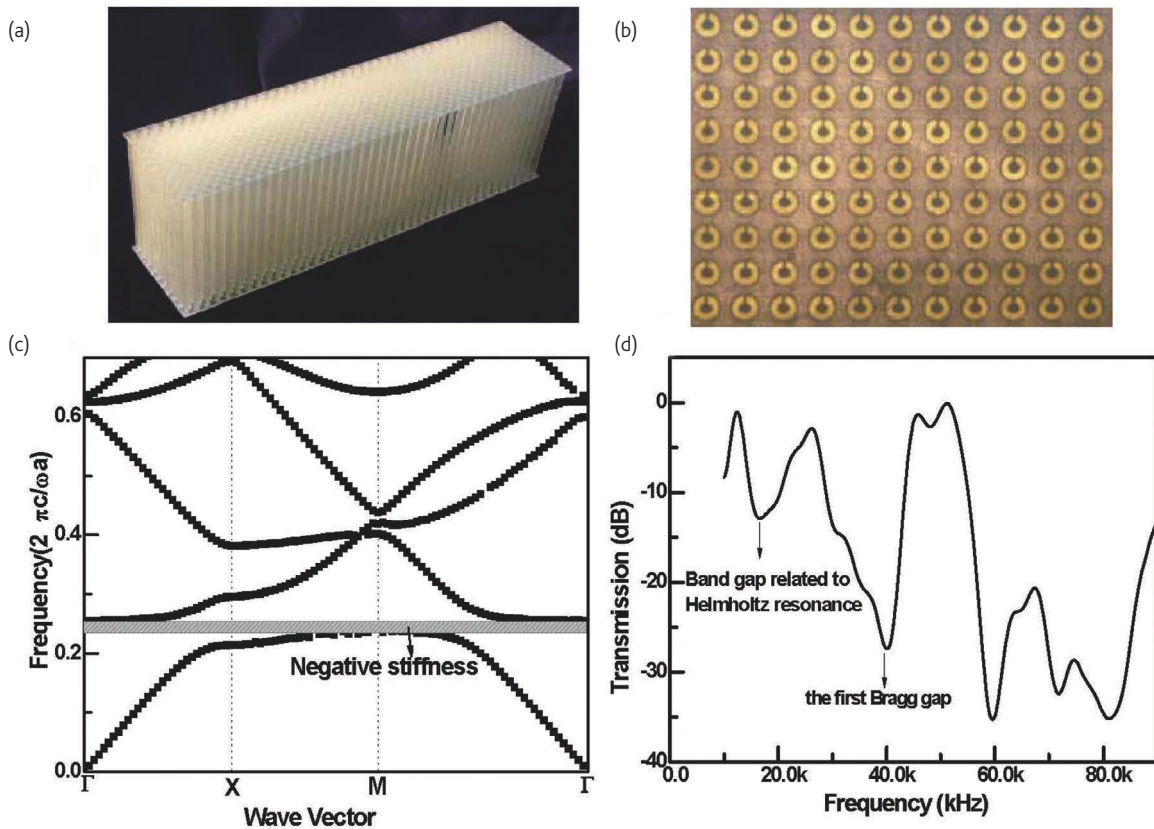


Fig. 4 The profile (a) and the platform (b) of the PC consisted of HRs formed by stereolithography. (c) the band structure of the PC consisted of HRs, clearly showing a low-resonant frequency gap with negative stiffness. (d) The amplitude transmission coefficient along the (ΓX) $[100]$ direction plotted as a function of frequency. The observed transmission characteristics correspond well with the calculated band structures. Here the period is 5 mm, so the normalized frequency f_0 is 69 kHz.

Acoustic surface evanescent waves on the surface of artificially structured metamaterials

In addition to the interesting acoustical physics and possible applications in bulk PCs and AMs discussed above, the existence of surface states of acoustic waves in artificial acoustic surface metamaterials (ASMs) and their unique properties are of great interest. Since the energy of acoustic waves is strongly confined to the surface, the amplitude of the acoustic surface wave decays exponentially along the third dimension. Hence, the associated larger in-plane wave vector can produce a shorter effective wavelength and a slower propagation speed, thus leading to promising chip-scale acoustic device applications.

In general there are two approaches to describing surface acoustic waves. An acoustic surface evanescent wave (ASEW)⁷⁰ can be excited in the interface between two semi-infinite homogeneous fluids with different signs of elastic parameters, as shown in Fig. 5a-b. The condition for the existence of such an ASEW is very similar to the equation governing the presence of surface plasmon polaritons (SPPs) at the interface between metal and dielectric media:

$$\frac{k_z^I}{\rho^I} + \frac{k_z^{II}}{\rho^{II}} = 0, \quad (3)$$

and its propagation wave vector can be expressed as follows:

$$k_y = \omega \left[\left(\frac{\rho^I \rho^{II}}{(\rho^{II})^2 - (\rho^I)^2} \right) \left(\frac{\rho^{II}}{B^I} - \frac{\rho^I}{B^{II}} \right) \right]^{1/2} \quad (4)$$

This equation is very similar to the dispersion equations of SPPs. SPPs, which are excited by the interaction between light and electron plasma on metal surfaces, have attracted much scientific interest, though the elementary excitation of such ASEWs remains a mystery. However, due to the similar nature of field distributions and high-energy confinement on the surface, it is highly desired to duplicate some of the exciting and exotic phenomena of SPPs, such as enhanced transmission⁷¹, superlensing^{72, 73}, enhanced absorption of light in molecules, and enhanced surface Raman scattering⁷⁴. Like SPPs, possible schemes for exciting ASEWs may include attenuated total reflection and grating coupling via phase-matching conditions.

As discussed above, however, it is difficult to design and fabricate AMs with double negative parameters. Therefore it is necessary to explore other methods to excite an ASEW. For example, we can reduce the thickness of a conventional PC to a single 'atomic' layer and thus achieve two-dimensional confinement using this single-layer PC. As anticipated, ASEWs be indeed excited on such single-layer

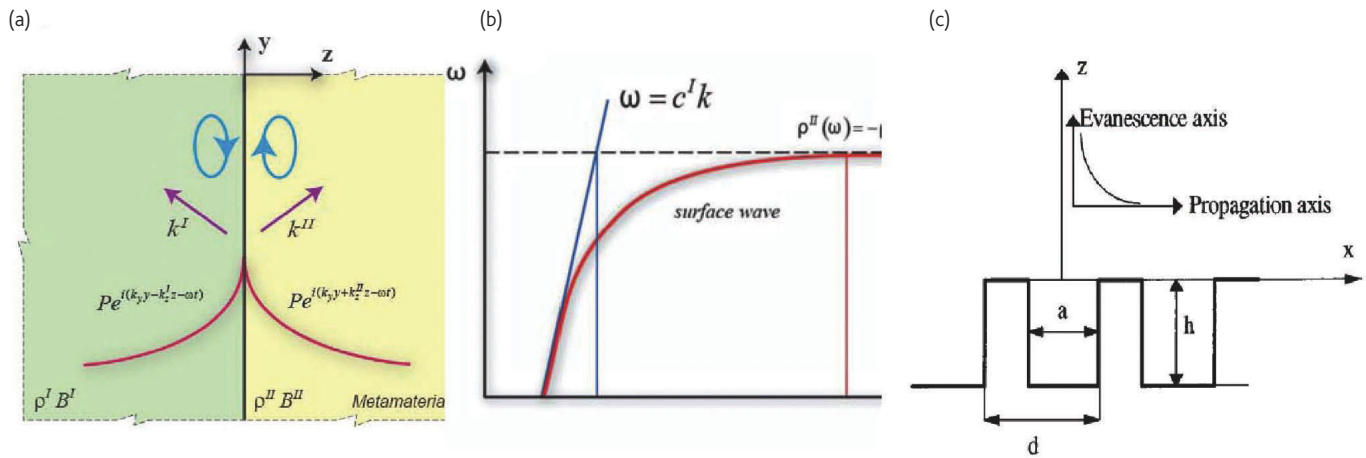


Fig. 5 (a) Schematic of the surface state at an interface separating two semi-infinite media. Medium I is considered to have positive material parameters whereas medium II is taken as an acoustic metamaterial with exotic material parameters. The pressure profile of surface bound states; it is maximum at the interface and decays exponentially normal to the interface. (b) Dispersion curve of the surface state at the interface between two semi-infinite media with mass densities of opposite signs. (c) A rectangular-groove grating, a surface wave that propagates along the periodic direction is represented over the structure.

structures. The rectangular-groove grating^{75, 76} ASEWs are different from conventional acoustic hybrid surface waves, such as Rayleigh waves and Lamb waves excited on the fluid–solid interface, as ASEWs are still purely longitudinal waves. In this case (Fig. 5c), the in-plane propagation wave vector and evanescent vertical wave vector are expressed, respectively, as follows:

$$k_x = k \left(1 + \frac{a^2}{d^2} \tan^2 k(h - a(\log 2) / \pi) \right)^{1/2}, \quad (5)$$

$$k_z = jk \frac{a}{d} \tan k((h - a(\log 2) / \pi)), \quad (6)$$

where a is the width of the groove, d is the period and h is the thickness of the groove.

As Eq. (5) indicates, since the propagation wave vector of an ASEW is larger than the wave vector in free space, it is necessary to use grating coupling to meet the phase-matching condition of the wave vector. From Eqs. (5) and (6), we find h to be the most important parameter; in other words, for longitudinal waves, the thickness h determines the localized Fabry–Perot resonance. We can thus draw the conclusion that the coupling between the incoming wave and the eigen mode of the local oscillation in the direction of vibration (i.e. the Fabry–Perot resonance) causes the excitation of ASEWs. The localized Fabry–Perot resonance makes the effective parameters exhibit single negative mass densities at certain frequencies.

ASEWs are not only excited on the surface between the grating and air, but can also be excited along the surface of a PC. Within the band gap, PCs may be regarded as effective media with a single negative parameter. The detailed surface resonant state has been calculated and elucidated by Liu *et al.*⁷⁷ using a supercell method. According to Liu *et*

al.'s theory, ASEWs can be excited on the surface of a finite PC within the band gap via a point wave source near the PC or a plane wave at a larger incidence angle.

ASEWs have already shown promise in several applications, including extraordinary acoustic transmission (EAT)^{78–81}, extraordinary sound shielding (EAS)⁸², acoustic collimation and direct beaming^{51, 83}, extraordinary tunneling through a metal plate⁸⁴, wave confinement and slow wave effects⁸⁵, and superlensing⁷⁰. Here we will focus on EAT since the physics behind EAT is the same as these other novel effects. EAT via ASEWs is very similar to extraordinary optical transmission (EOT), a hot topic since 1998⁷¹. EAT was investigated in a subwavelength system without any surface collective oscillation like plasma, which is helpful for understanding the possible mechanisms of EOT. We theoretically and experimentally elucidated the EAT phenomena through a one-dimensional grating with very narrow apertures⁷⁹, and revealed that the coupling between the diffracting wave and the wave-guide FP (Fabry–Perot) resonance mode plays a key role in EAT derived by the rigorous coupling wave approximation (RCWA) method (Fig. 6a). We believe that this work is consistent with Christensen's theory⁸⁰, which attributes EAT to the coupling between the leaky acoustic surface waves in the two sides of the gratings through narrow slits. As discussed above, the ASEW above the surface of the grating is due entirely to the coupling between the incoming wave diffracted by the narrow slits of the grating, and the eigen mode of the local resonance (i.e. the Fabry–Perot resonance). The localized Fabry–Perot resonance makes the effective parameters exhibit a single negative mass density at certain frequencies. The dispersion relations of the ASEW mode (which is not a guided mode) are also shown in Fig. 6b. Although the discrepancies between EAT and EOT are obvious (the zero-order propagating mode exists in narrow apertures for the acoustic system, but in optical subwavelength systems, the truncated evanescent mode exists in the metal slits), they also share

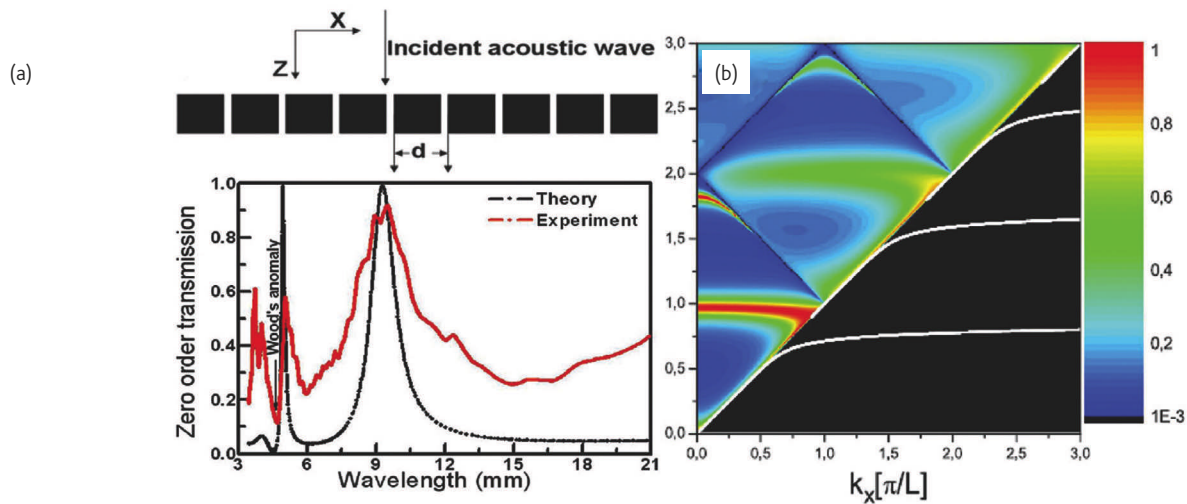


Fig. 6 (a) Numerical (black curve) and experimental (red curve) zero-order transmission spectra for a rectangular grating with the size of 4 mm and a period of 4.5 mm. The figure clearly shows the extraordinary transmission for acoustic sub-wavelength system. (b) Left: the amplitude transmission as a function of wave number and transverse wave vector k_x . Right: dispersion relation of the leaky acoustic surface evanescent waves.

some similarities: for transverse electromagnetic waves, the transverse surface charge oscillation coupling leads to SPPs, while for longitudinal acoustic waves, the longitudinal Fabry–Perot oscillation coupling results in ASEWs. We believe these studies provide the fundamental basis for the extraordinary transmission in subwavelength systems.


On the other hand, ASEWs also play key roles in some interesting phenomena in bulk AMs such as negative refraction and subdiffraction-limited focusing. According to Pendry's theory⁷², in order to obtain a higher resolution, beyond Rayleigh's prediction, we must collect as large a spectrum of evanescent waves as possible and use all of this in the imaging process. Great efforts have been made to explore such approaches. For instance, in a superlens made of an AM with double-negative parameters, ASEWs are excited on the air–AM interface, and thus contribute to the far-field imaging. Another method is to adopt a metamaterial with a highly anisotropic EFS for the magnification of subwavelength features in the far field for acoustic waves⁸⁶, like an electromagnetic hyperlens⁸⁷. Very recently, He *et al.*⁸⁸ have reported a method for obtaining subwavelength imaging of acoustic waves using a two-dimensional PC based on a canalization mechanism⁸⁸. By designing a PC with flat EFSs, the evanescent modes of the acoustic source can be canalized by the Bloch modes in the PC and hence transmitted through the PC to reach the image⁸⁸. It is therefore very important to explore significant improvements to achieve subwavelength imaging of acoustic waves, not only for the study of the basic theory, but also for ultrasonic applications, especially for medical photography. We believe the crucial step to reaching this target is knowledge of how to control and make use of ASEWs.

Prospects

While numerous exciting effects have been demonstrated, such as bulk acoustic waves, other forms of elastic waves, e.g. Lamb waves⁸⁹ and

Rayleigh waves⁹⁰, could in principle be controlled by the corresponding PCs and AMs when two-dimensional structures are prepared in the thin solid plate or on the surface of solid. These kinds of PC and AM would be better suited for chip integration to create devices that can exploit acoustic surface waves for signal processing and as sensors. However, since these surface waves are quasi-two-dimensional waves and have complicated eigen modes, the methods for calculating their band structures need further development. In the meantime, the fabrication of these PC and AM structures to experimentally explore the interesting effects described above is also a big challenge due to the relatively large thickness of several micrometers or more.

Another important aspect is to realize hypersonic PCs and AMs. Some examples have successfully been shown in colloidal crystal at THz frequencies^{91–93}. These frequency bands are important because they lie between the bulk vibration and heat vibration of atoms in real crystals, and correspond to the collective vibration of nanomaterials. These phenomena are thus crucial to understanding nanomaterials and related elementary excitation.

For the last two decades acoustic structured materials have developed side by side with optical ones. Although acoustic and optical waves are quite different, photonic crystals were followed by the proposal of PCs, optical metamaterials stimulated studies of AMs, and SPPs triggered studies of ASEWs. As the frequency of acoustic structured materials becomes higher and higher, and their size smaller and smaller, the two counterparts will meet, perhaps resulting in very different and extraordinary effects that would never occur without each of type of material participating. Phonon–photon interaction and coupling will play key roles in these artificial structures and provide a new platform for each to be manipulated by the other. 

Acknowledgments

Thanks to Prof. T. J. Cui. His kindness and efforts to organise the conference are gratefully acknowledged. The work was jointly supported by the National Basic Research Program of China (2007CB 613202) and the National Nature Science

Foundation of China (50632030). We also acknowledge the support from the Changjiang Scholars and Innovative Research Team in University (PCSIRT) and the Nature Science Foundation of Jiangsu Province (BK2007712)

References

1. Yablonovitch, E., *Phys. Rev. Lett.* (1987) **58**, 2059.
2. John, S., *Phys. Rev. Lett.* (1987) **58**, 2486.
3. Brillouin, L., *Wave Propagation in Periodic Structures* Dover, New York, (1953).
4. Kushwaha, M. S., et al., *Phys. Rev. Lett.* (1993) **71**, 2022
5. Martinez-Sala, R., et al., *Nature* (1995) **378**, 241.
6. Sigalas, M., and Economou, E. N., *J. Sound Vib.* (1992) **158**, 377.
7. Qiu, C. Y., *Appl. Phys. Lett.* (2006) **89**, 063106.
8. Page, J. H., et al., *Science* (1996) **271**, 634.
9. Schriemer, H. P., et al., *Phys. Rev. Lett.* (1997) **79**, 3166.
10. Zhang, X. D., and Liu, Z. Y., *Appl. Phys. Lett.* (2004) **85**, 341.
11. Yang, S. X., et al., *Phys. Rev. Lett.* (2004) **93**, 024301.
12. Imamura, K., and Tamura, S., *Phys. Rev. B* (2004) **70**, 174308.
13. Qiu, C., et al., *Phys. Rev. B* (2005) **71**, 054302.
14. Feng, L., et al., *Phys. Rev. B* (2005) **72**, 033108.
15. Ke, M., et al., *Phys. Rev. B* (2005) **72**, 064306.
16. Feng, L., et al., *Phys. Rev. Lett.* (2006) **96**, 014301.
17. Lu, M. H., et al., *Nature Mater.* (2007) **6**, 744.
18. Feng, L., et al., *Phys. Rev. B* (2006) **73**, 193101.
19. Hu, X. H., et al., *Phys. Rev. E* (2004) **69**, 030201.
20. Liu, Z., et al., *Science* (2000) **289**, 1734.
21. Li, J., and Chan, C. T., *Phys. Rev. E* (2004) **70**, 055602.
22. Fang, N., et al., *Nat. Mater.* (2006) **5**, 452.
23. Cheng, Y., et al., *Appl. Phys. Lett.* (2008) **92**, 051913.
24. Mei, J., et al., *Phys. Rev. Lett.* (2006) **96**, 024301.
25. Ding, Y. Q., et al., *Phys. Rev. Lett.* (2007) **99**, 093904.
26. Hu, X. H., and Chan, C. T., *Phys. Rev. E* (2005) **71**, 055601.
27. Liu, Z. Y., et al., *Phys. Rev. B* (2005) **71**, 014103
28. Soukoulis, C. M., *Photonic Band Gap Materials*, Kluwer Academic, Dordrecht (1996).
29. Joannopoulos, J. D., et al., *Photonic Crystals*, Princeton University Press, Princeton, (1995).
30. Sakoda, K., *Optical Properties of Photonic Crystals*, Springer-Verlag Berlin Heidelberg, 2nd ed. (2005)
31. Economou, E. N., and Sigalas, M., *Phys. Rev. B* (1993) **48**, 13434.
32. Kushwaha, M. S., and Halevi, P., *J. Acoust. Soc. Am.* (1997) **101**, 619.
33. Vasseur, J. O., et al., *Phys. Rev. Lett.* (2001) **86**, 3012.
34. Li, Z. Y., and Ho, K. M., *Phys. Rev. B* (2003) **68**, 155101.
35. Li, L. M., et al., *Phys. Rev. B* (1998) **58**, 9587.
36. Kafesaki, M., and Economou, E. N., *Phys. Rev. B* (1999) **60**, 11993.
37. Liu, Z. Y., et al., *Phys. Rev. B* (2000) **62**, 2446.
38. Tanaka, Y., et al., *Phys. Rev. B* (2000) **62**, 7378.
39. Vasseur, J. O., et al., *Phys. Rev. Lett.* (2001) **86**, 3012.
40. Goffaux, C., and Sanchez-Dehesa, J., *Phys. Rev. B* (2003) **67**, 144301.
41. Shen, L. F., et al., *Phys. Rev. B* (2003) **68**, 035109.
42. Sigmund, O., and Hougaard, K., *Phys. Rev. Lett.* (2008) **100**, 153904.
43. Torres, M., et al., *Phys. Rev. Lett.* (1999) **82**, 3054.
44. Sanchis-Alepuz, H., et al., *Phys. Rev. Lett.* (2007) **98**, 134101.
45. Yang, S. X., et al., *Phys. Rev. Lett.* (2002) **88**, 104301.
46. Zhang, X. D., and Liu, Z. Y., *Phys. Rev. Lett.* (2008) **101**, 264303.
47. Luo, C., et al., *Phys. Rev. B* (2002) **65**, 201104.
48. Kittel, C., *Introduction to Solid State Physics*, John Wiley & Sons, New York (1996), p. 175.
49. Kushwaha, M. S., *Appl. Phys. Lett.* (1997) **70**, 3218.
50. Khelif, A., *Phys. Rev. B* (2003) **68**, 024302.
51. Chen, L. S., et al., *Appl. Phys. Lett.* (2004) **85**, 1072.
52. Ke, M. Z., et al., *Appl. Phys. Lett.* (2007) **90**, 083509.
53. Li, J., et al., *Phys. Rev. B* (2006) **73**, 054302.
54. Sukhovich, A., et al., *Phys. Rev. B* (2008) **77**, 014301.
55. Torrent, D., and Sanchez-Dehesa, J., *New J. Phys.* (2008) **10**, 063015.
56. Veselago, V. G., *Sov. Phys. Uspekhi* (1968) **10**, 509.
57. Fok, L., et al., *MRS Bull.* (2008) **33**, 931.
58. Sheng, P., *Introduction to Wave Scattering, Localization and Mesoscopic Phenomena*, Academic, New York, 1995
59. Ye, Z., and Hsu, H., *Appl. Phys. Lett.* (2001) **79**, 1724.
60. Wang, Z. G., et al., *J. Appl. Phys.* (2008) **103**, 064907.
61. Cheng, Y., et al., *Phys. Rev. B* (2008) **77**, 045134.
62. Lai, A., et al., *Microwave Mag. IEEE* (2004) **5**, 34.
63. Hu, X. H., et al., *Phys. Rev. B* (2008) **77**, 172301.
64. Fokin, V., et al., *Phys. Rev. B* (2007) **76**, 144302.
65. Hou, Z., et al., *Phys. Rev. E* (2005) **71**, 037604.
66. Papanikolaou, N., et al., *Phys. Rev. Lett.* (2008) **101**, 253903.
67. Chen, Y. F., et al., *Phys. Rev. Lett.* (2005) **95**, 067402.
68. Decoopman, T., et al., *Phys. Rev. Lett.* (2006) **97**, 073905.
69. Smigaj, W., and Gralak, B., *Phys. Rev. B* (2008) **77**, 235445.
70. Ambati, M., et al., *Phys. Rev. B* (2007) **75**, 195447.
71. Ebbesen, T. W., et al., *Nature* (1998) **391**, 667.
72. Pendry, J. B., *Phys. Rev. Lett.* (2000) **85**, 3966.
73. Fang, N., et al., *Science* (2004) **308**, 534.
74. Raether, H., *Surface Plasmons on Smooth and Rough Surfaces and on Gratings*, Springer-Verlag, Berlin Heidelberg, New York, London (1986).
75. Kelders, L., et al., *J. Acoust. Soc. Am.* (1998) **103**, 2730.
76. Kelders, L., et al., *J. Acoust. Soc. Am.* (1998) **104**, 882.
77. Zhao, D., et al., *Phys. Rev. B* (2007) **76**, 144301.
78. Zhang, X. D., *Phys. Rev. B* (2005) **71**, 241102.
79. Lu, M.-H., et al., *Phys. Rev. Lett.* (2007) **99**, 174301.
80. Christensen, J., et al., *Phys. Rev. Lett.* (2008) **101**, 014301.
81. Hou, B., et al., *Phys. Rev. B* (2007) **76**, 054303.
82. Estrada, H., et al., *Phys. Rev. Lett.* (2008) **101**, 084302
83. Christensen, J., et al., *Nature Phys.* (2007) **3**, 851
84. Ke, M., et al. *Phys. Rev. Lett.* (2007) **99**, 044301.
85. Christensen, J., et al. *Appl. Phys. Lett.* (2008) **93**, 083502.
86. Ao, X. Y., and Chan, C. T., *Phys. Rev. E* (2008) **77**, 025601.
87. Liu, Z. W., et al., *Science* (2007) **315**, 1686.
88. He, Z. J., et al., *Appl. Phys. Lett.* (2008) **93**, 233503.
89. Bonello, B., et al., *Appl. Phys. Lett.* (2007) **90**, 021909.
90. Tanaka, Y., and Tamura, S. I., *Phys. Rev. B* (1998) **58**, 7958.
91. Gorishnyy, T., et al., *Phys. Rev. Lett.* (2005) **94**, 115501.
92. Cheng, W., et al., *Nature Mater.* (2006) **5**, 830.
93. Akimov, V., et al., *Phys. Rev. Lett.* (2008) **101**, 033902.

materialstoday

See your work on the cover of
Materials Today!

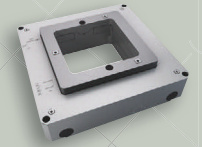
Materials Today invites you to submit your best materials-research related image to be considered for publication on the cover for one of the 2010 monthly issues.

The winning images last year made a real impact on our covers. Unlike last year there will be one overall winner which will appear on a cover during the year and 2 runners up which will appear in another format within *Materials Today* magazine during the year.

Closing date for submission
of images is 14th December 2009

Please visit our website for further information:
www.materialstoday.com

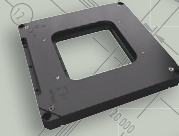
Nanopositioning Systems



Piezo Drivers & Controllers

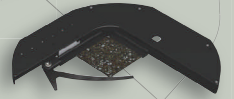


OEM Design



Visit us at MRS
Booth # 607

Integrated Solutions



Next Generation Scanning
Technology

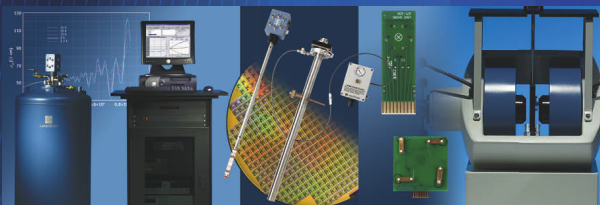


Tools for Research & Industry

Phone • (608) 204.8756
E-mail • info@npoint.com
Web • npoint.com



L A K E S H O R E H A L L E F F E C T M E A S U R E M E N T S Y S T E M S



10 $\mu\Omega$ to 200 G Ω resistances ■ 2 K to 800 K temperatures

Fields to 9 T ■ Easy sample access

Accommodate up to one 6-inch or four 1 cm² samples

QMSA® resolves individual carriers in multi-carrier devices

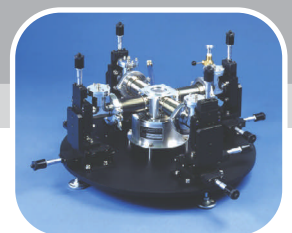
AC current for low resistance, high resolution measurement

 **LakeShore**®

575 McCorkle Boulevard Westerville OH 43082
Phone: (614) 891-2244 Fax: (614) 818-1600
info@lakeshore.com www.lakeshore.com

JANIS

Cryogenic Products for Materials Characterization



Janis has a wide range of products geared towards the materials scientist, covering nearly any temperature range or application.

Typical techniques include: VSM, MOKE, FTIR, ESR, EPR, NMR, Hall effect, DLTS, Mössbauer, STM, AFM and more

Typical applications include:

- Microscopy
- UV-Vis-IR optical measurements
- Nanoscale electronics
- Spintronics
- High frequency measurements
- Non-destructive device and wafer testing
- Photovoltaics
- High T_c superconductors
- Terahertz detectors and devices

Janis Research Company

2 Jewel Drive Wilmington, MA 01887 USA
TEL +1 978 657-8750 FAX +1 978 658-0349 sales@janis.com
Visit our website at www.janis.com

Electromagnetic wave in 2D photonic crystals

In this article, we have reviewed recent progresses on the negative refraction and the abnormal transmission of electromagnetic wave in two-dimensional photonic crystals. The physical mechanisms related to these phenomena have been analyzed, and the focusing properties of the point source through the photonic-crystal-based flat lens have been discussed. Recent investigations on the abnormal transmission and Zitterbewegung effect of wave transport near the Dirac point in two-dimensional photonic crystals have also been introduced.

Xiangdong Zhang

Department of Physics, Beijing Normal University, Beijing 100875, China

E-mail: zhangxd@bnu.edu.cn

During the past two decades, a significant effort has been devoted to the study of photonic crystals (PCs) both theoretically and experimentally¹⁻³. The PCs are regular arrays of materials with different refractive indices, which are classified mainly into one-, two-, and three-dimensional structures according to the dimensionality of the stack. Since the PCs can have spectral gaps in which electromagnetic wave propagation is forbidden in all directions, they offer the possibility of controlling the flow of photons in a way analogous to electrons in a semiconductor⁴⁻⁸. Thus, it can have profound implications for quantum optics, high-efficiency lasers, optoelectronic devices, and other areas of applications¹⁻¹¹. In the first decade, studies have focused on the materials with large gaps. Various photonic band-gap structures have been successfully fabricated for frequencies in both microwave and near-infrared regions^{1-3, 12-18}. Based on them, some wave guides, optical fibers, cavities, optical switches, low-threshold lasers and high-efficient light-emitting diodes have

been designed^{1-3, 19-22}. It is also proposed that such PCs may hold the key to the continued progress towards all-optical integrated circuits²³.

In contrast to the study of gaps in the PCs, wave transport in band regions can also exhibit some different properties in comparison with those in general homogeneous media²⁴. For example, negative refraction can occur at the interface between a PC and a positive (conventional) medium^{25, 26}. In the past decade, there has been a great deal of interest in studying the negative refraction and left-hand materials (LHMs)²⁷⁻⁴⁰. In fact, the phenomena of negative refraction of waves at interfaces have been analyzed theoretically by Mandel'shtam in the early 1940s⁴¹, but they have only been recently demonstrated experimentally²⁸. As was shown by Veselago⁴², the LHMs possess a number of unusual electromagnetic effects including negative refraction, inverse Snell's law, reversed Doppler shift, and reversed Cerenkov radiation. These anomalous phenomena have also been observed in the PCs^{25, 26, 43-52}.

Negative refraction and focusing by 2D photonic crystals

Negative refraction in the PCs was first observed by Kosaka *et al.*²⁵ in 1998. Subsequently, there have been a number of reported experimental demonstrations and theoretical studies in this field^{26, 43-66}. The physical principles that allow negative refraction in the PCs arise from the dispersion characteristics of wave propagation in a periodic medium, which can be well described by analyzing the equipfrequency surface (EFS) of the band structure^{26, 43-50}. Fig. 1 shows a typical branch of a dispersion surface in reciprocal space. The curvature of the dispersion surface turns from downward to upward, and incident light comes from the top of the figure. The direction of propagation light in the PCs is normal to the dispersion surface. Due to different shape of the curvature, the flux directions of the propagation wave at various points are different, which can be obtained by the group velocity, $v_g = \nabla_{\kappa} \omega(\kappa)$, where ω is the optical frequency at the wave vector κ . This means that there are various transport properties of the wave in the PCs, for example, divergent propagation as in a concave lens (point A), collimated propagation (point B) and negative refraction (point C). Therefore, the negative refraction is only one kind of way for the wave transport in the PCs. It is determined by the shape of the EFS or the structure of the PCs. Thus, we can tune it by choosing the various structures of the PCs⁵³. Because the phenomena and the physical origin for the negative refraction in 2D and 3D PCs are similar⁴⁴⁻⁷², in the following we will focus our discussion on the negative refraction in the 2D PCs.

Fig. 2b describes several constant frequency contours for the second band of the 2D PC with a triangular lattice for the S wave. The corresponding band structure is plotted in Fig. 2a. It is clear from the figure that the frequencies increase inwards, meaning that $\vec{S} \cdot \vec{k} < 0$ and the group velocities v_g are opposite to the phase velocity. Here, \vec{S} and \vec{k} represent the Poynting vector and wave vector, respectively. This indicates that the transmitting features of the wave in such a PC structure have a left-handed behavior. At the same time, we also notice

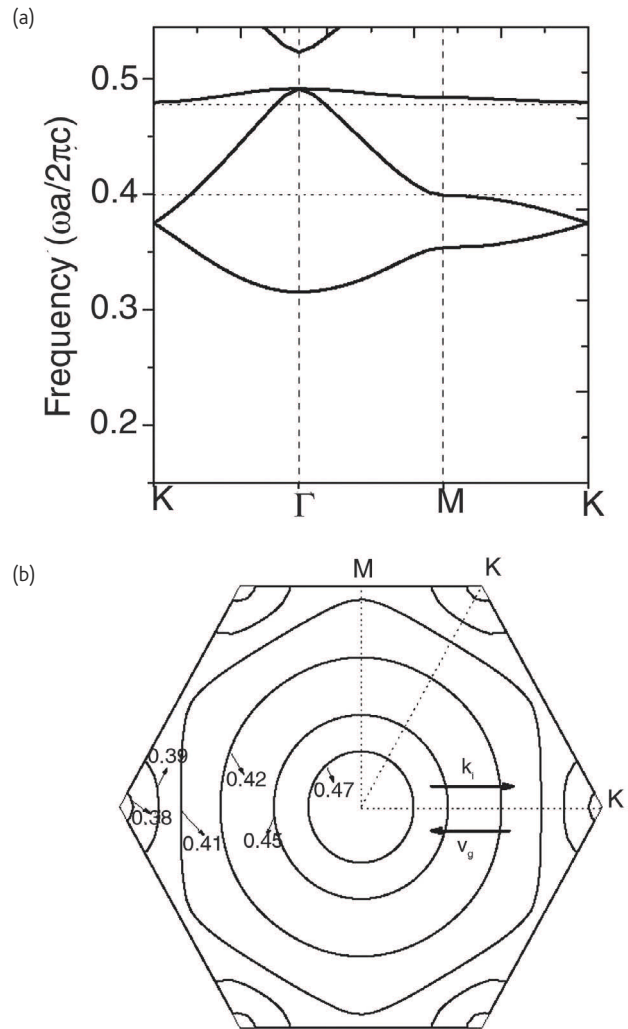


Fig. 2 (a) The calculated photonic band structure of a triangular lattice of coated cylinder in air for the S wave. The radii of the dielectric cylinder and inner metallic cylinder are $R=0.45a$ and $r=0.25a$, respectively. The dielectric constant of the cylinder is taken as 11.4. (b) Several constant frequency contours for the corresponding structure.

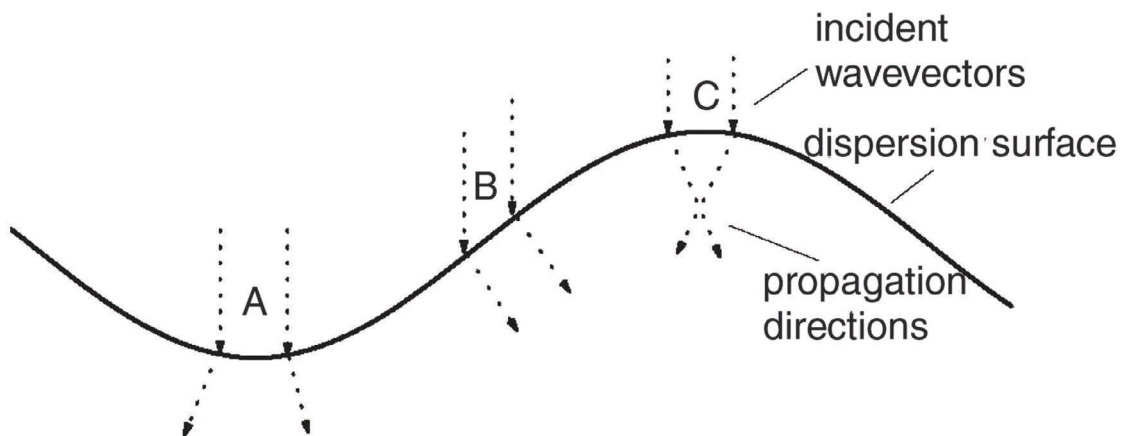


Fig. 1 A schematic illustration of wave transmitting through the PC. Arrows above the dispersion surface indicate incident wavevectors in reciprocal space. Arrows below the dispersion surface indicate the energy flow in real space.

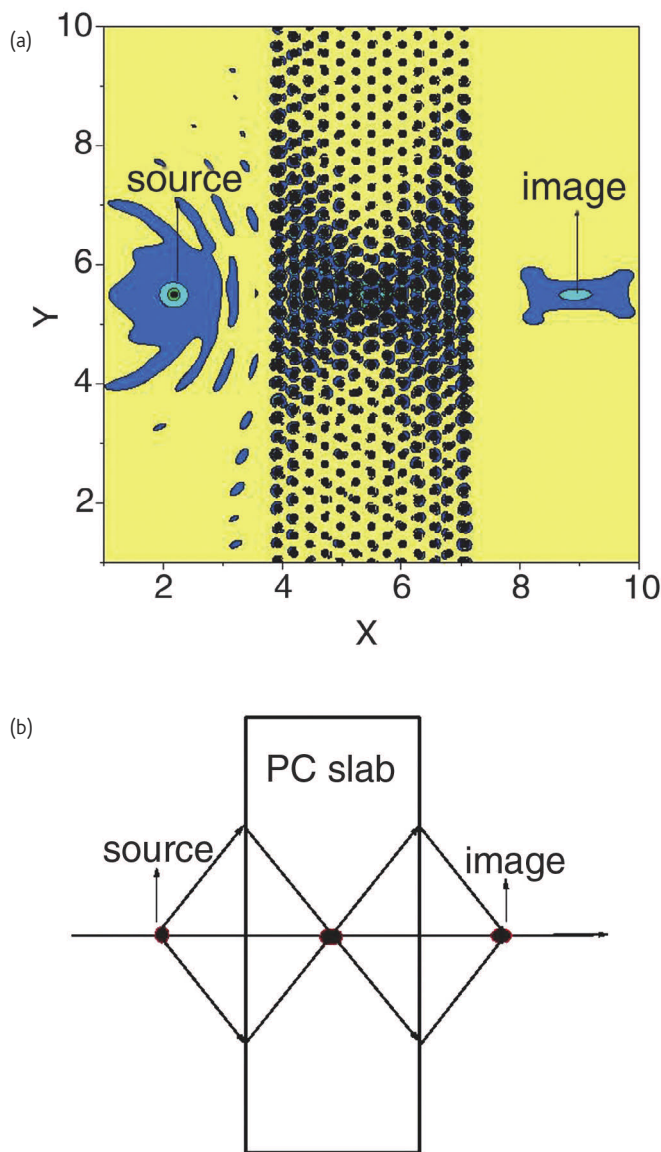


Fig. 3 (a) The intensity distribution of point source and its image across a $11a$ 2D PC slab at $\omega = 0.42 - 0.47(2\pi a/c)$ for the S wave. The structure and parameters are identical with those in Fig. 2. (b) Schematic picture depicting the lensing of a source by a PC slab to an image are shown on top of the figure.

that some EFS contours such as $\omega = 0.42 - 0.47(2\pi a/c)$ are very close to a perfect circle, indicating that the crystal can be regarded as an effective homogeneous left-handed medium at these frequencies^{26, 56}.

By using such a PC, we can design a flat lens to focus a point source on one side of the lens into a real point image on the other side⁵⁴⁻⁶². Fig. 3 represents the typical field intensity pattern for such a lens. X and Y are vertical and transverse directions of the wave propagating, respectively. The field intensity in the figure is over a $30a \times 30a$ region around the center of the sample (here a is the lattice constant of the structure). The geometry of the PC slab is also displayed for clarity. The high quality image in the opposite side of the slab and the focusing in

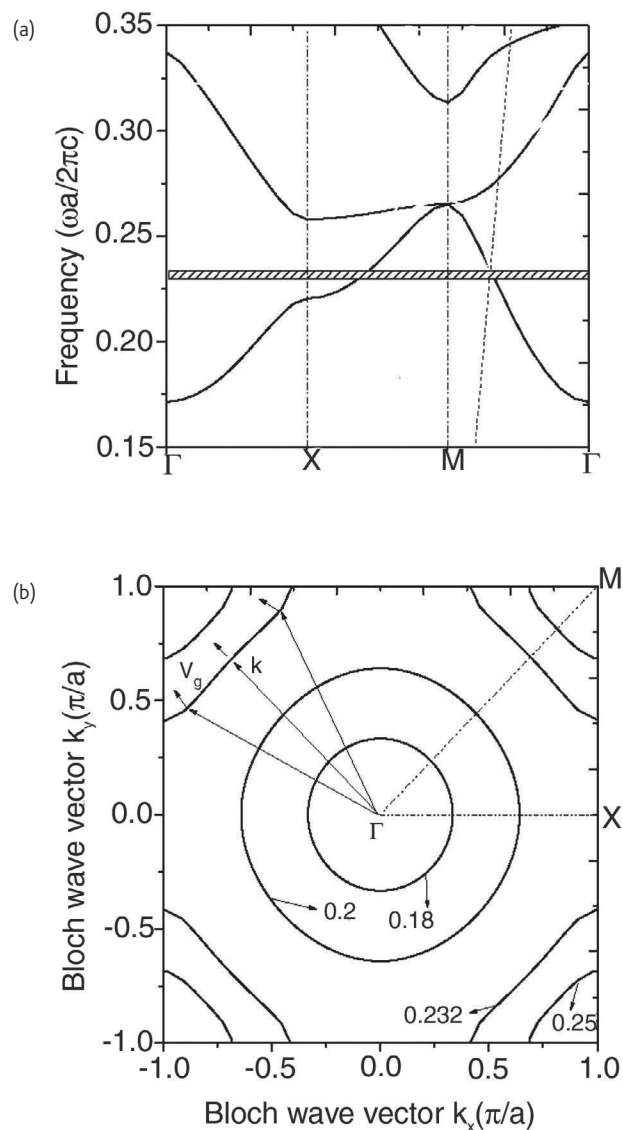


Fig. 4 (a) The calculated photonic band structure of a square lattice of coated cylinder in air for the S wave. The radii of the dielectric cylinder and inner metallic cylinder are $R=0.45a$ and $r=0.15a$, respectively. The dielectric constant of the cylinder is taken as 14. (b) Several constant frequency contours for the corresponding structure.

the middle of the slab are clearly observed. If we move the position of the source, the image distance changes simultaneously. The relation between the length of the object and the image distance explicitly follows the well-known wave-beam negative refraction law. This means that the image is non-near-field. Such a theoretical result has been demonstrated experimentally⁶².

The above example shows that the maximum of the dispersion curve is located at the Γ point of the Brillouin zone and the negative refraction comes from the backward wave effect. In fact, the negative refraction can also be realized without employing the backward wave effect by using the PCs^{45, 46, 63-69}. Fig. 4a-b display the band structure

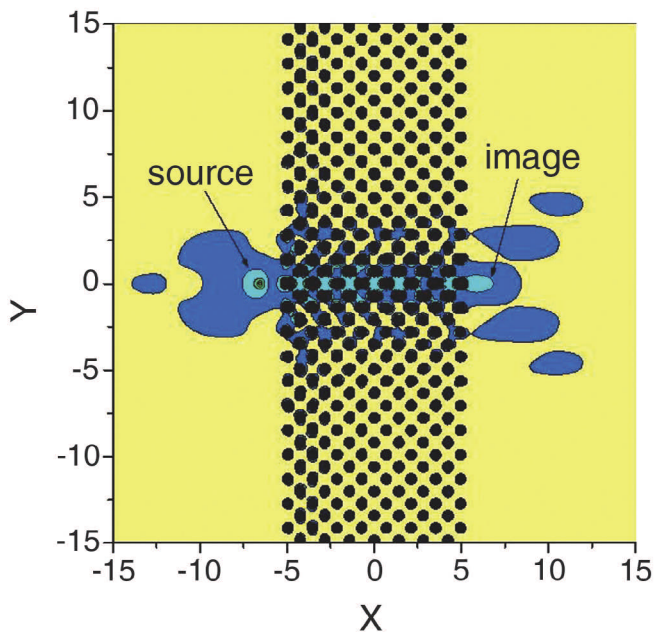


Fig. 5 The intensity distribution of a point source and its image across a 11a 2D PC slab at $\omega = 0.231 (2\pi a/c)$. The structure and parameters are identical with those in Fig. 4.

and several constant frequency contours for the first band of the 2D PC with a square lattice for the *S* wave. We find that the lowest bands have $\vec{S} \cdot \vec{k} > 0$ everywhere within the first Brillouin zone, meaning that the group velocities are never opposite to the phase velocity. However, some low frequency contours such as $0.232(2\pi a/c)$ are significantly distorted from a circle, being convex around points M. The conservation of the *k* component along the surface of refraction will also result in the negative refraction effect. The advantages of the negative refraction in the lowest valence band are single-mode and high transmission. In the high frequency case, the left-handed and the right-handed behaviors are easily produced simultaneously due to the excitations of the multiple-mode⁴⁴. The single-mode and all-angular negative refraction are very important to some applications in designing optical devices.

The two seemingly rather different situations (Fig. 2 and Fig. 4) do share one common feature; the photonic effective mass near a local maximum of the dispersion curve is negative-definite. From such a point of view, they rely on the same mechanism that the relative wave vector of a local frequency maximum is pointed opposite to the group velocity. There is also the same usefulness for them. For example, they all can be applied to design the flat lens and realize the focusing of the wave. Fig. 5 describes the intensity distributions of the flat lens realized by the PCs with a square lattice. In such a case, the position of the image does not change while moving the source, and the image is located in the near-field region. This is due to the anisotropy of the dispersion or the self-collimation effect⁶⁵. However, the self-collimation effect can in principle be suppressed by changing

the scatters, and the positions of the focusing (in the near-field region or the non-near-field region) can be tuned^{53, 60}. The focusing in the near-field region or the non-near-field region have the same origins. All come from the negative refraction.

It is well known that the electromagnetic wave can be decomposed into *E* polarization (*S* wave) and *H* polarization (*P* wave) modes for the 2D PC structures. However, the above discussions focus on a certain polarized wave, *S* wave or *P* wave. It is interesting that a complete negative refraction region for all polarized waves can also be realized by engineering the 2D PC structure^{60, 64}. Therefore, the same structure and parameters yield the relative refractive index of $n=-1$ at the same frequency for both polarized waves. Thus the focusing of unpolarized electromagnetic waves can be realized by the same PC slab⁶⁰.

There are two aspects relating to the focusing. One is position (in the near-field region or the non-near-field region), and the other is resolution (full width at half maximum of the focus spot). The position of the image depends on the effective refractive index of the sample and the homogeneity of the materials, and it does not depend on whether or not the evanescent waves are amplified. The focus and image can still be observed if only the propagating waves are considered. In such a case, the image resolution cannot beat the diffraction-limit. In contrast, the superlensing effect comes from the evanescent waves (or resonance transmission). Several studies^{46, 67, 69} have shown that the surface termination within a specific cut of the structure can excite surface waves and allow the reconstruction of evanescent waves for a better focus. In fact, apart from the surface termination, the other methods such as changing the dielectric constants of interface layers, adding symmetric cap layers and introducing optical gain in the surface layers can also improve the image resolution⁶¹. In contrast, the effect of disorder always reduces the image resolution (including image peaks and full width at half maximum of the focusing). The role of the disorder is similar to that of material absorption⁶¹.

In addition, we would like to point out that the negative refraction not only exists in the periodic PCs, but also in some high-symmetric photonic quasicrystals (PQC). This has been demonstrated both theoretically and experimentally⁷³⁻⁷⁵. Similar to the periodic PCs, we can also use the PQC to design the flat lens and realize the focusing of the wave. Although the flat lens consisting of the PQC is not better than the periodic PCs in all aspects, it has some advantages in producing the non-near-field images due to their higher rotational symmetry. For example, it is very difficult to construct a flat lens by using pure dielectric cylinder of periodic structure to realize the non-near-field focus for the *S* wave, but it is easy to complete by high symmetry PQC slab. Thus, the investigation of the negative refraction and the focusing of the PQC can open a new window in the realistic application of such a phenomenon.

The above introduction about the application of the negative refraction is only for the flat lens and focusing. In fact, the negative

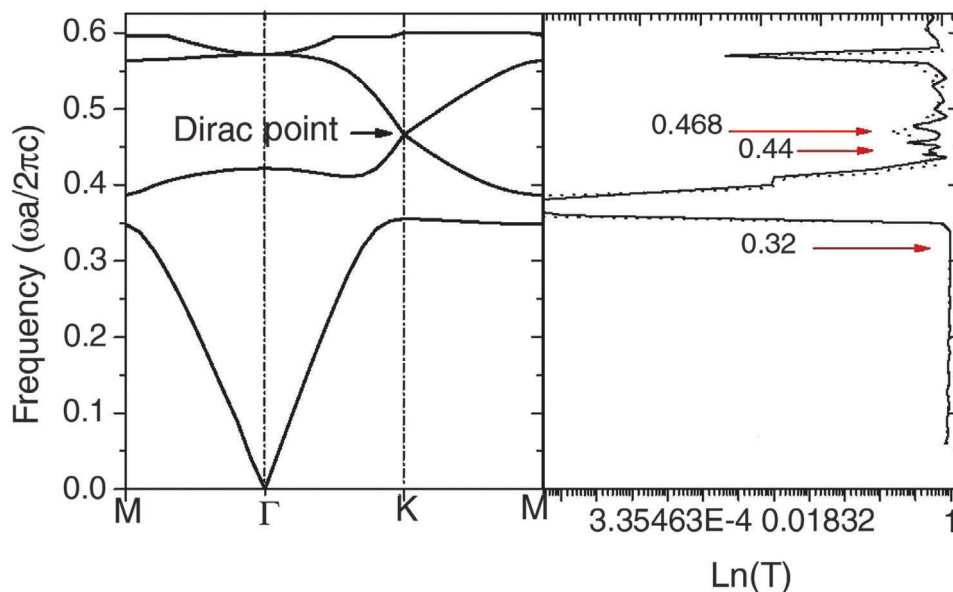


Fig. 6 Calculated photonic band structure of P wave for a triangular lattice of dielectric cylinder with $R/a=0.3$ and $\epsilon = 11.4$ in an air background.

refraction can also play important roles in other areas such as open cavity⁷⁶, slow light^{77, 78} and so on.

Abnormal transmission of electromagnetic wave through 2D PC slab

In general, there are two kinds of regime for the electromagnetic wave transport in the PCs¹⁻³. One is at the gap regions; the transmission is

suppressed exponentially with the increase of the sample thickness. The other is at the band regions; the transmission does not depend on the thickness of the sample and exhibits the standard ballistic behavior. The transport of the wave in the band regions is similar to the case of an effective medium. Thus, the PCs behave as the materials having an effective refractive index controllable by the band structure. The effective refractive index can vary from negative

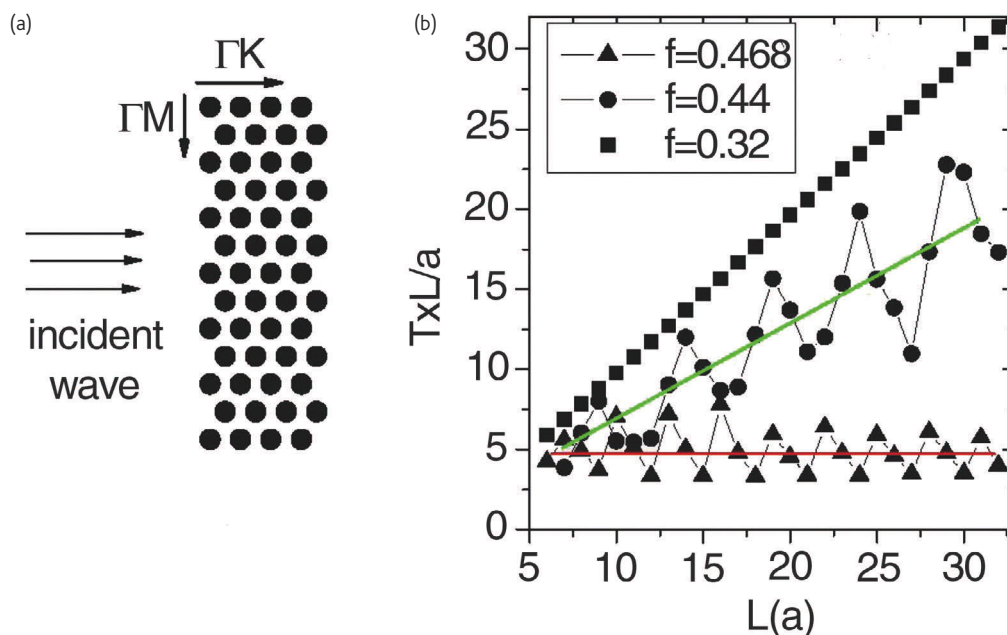


Fig. 7 (a) Schematic picture depicting simulation processes. (b) The product of T and L as a function of sample thickness at different frequencies. The frequencies are in unit of $\omega a/2\pi c$. Red line and green line are plotted only for view. The other parameters are identical to those in Fig. 1.

to zero and then to positive with frequency. Fig. 6 describes the band structure of P wave for the system with a 2D triangular lattice of cylinders immersed in air background. The key feature of this band structure is that the band gap may become vanishingly small at corners of the Brillouin zone at $f = 0.466\omega a/2\pi c$, where two bands touch as a pair of cones in a linear fashion. Such a conical singularity is referred to as the Dirac point^{79, 80}. Above the Dirac point, the effective refractive index of the PC is positive. In contrast, it becomes negative below the point. The negative refraction and focusing of the wave transport in such a case have been discussed in the above part. At the Dirac point, the effective refractive index is zero. Recent investigations show that the transmission properties of the wave near the Dirac point are different from the above two kinds⁸¹⁻⁸⁴. It can be regarded as a new transport regime, which is similar to the properties of electron transport at the Dirac point of the graphene^{85, 86}.

According to analyses^{79, 80}, wave transport near the Dirac point in the PCs can be described by the Dirac equation. For such a PC slab with thickness L in air background, we can obtain the transmission $T \propto 1/L$ by applying the resolution of Dirac equation and boundary condition of flux conservation⁸¹. The transmission of the wave through 2D PC slab is inversely proportional to its thickness. Such a theoretical result has been demonstrated by the exact numerical simulations⁸²⁻⁸⁴.

The triangular dots in Fig. 7 represent the numerical result for the product of T along the ΓK direction and L as a function of the sample thickness at $f = 0.468\omega a/2\pi c$ (near the Dirac point). For comparison,

we also give the results at $f = 0.44\omega a/2\pi c$ (away from the Dirac point) and $f = 0.32\omega a/2\pi c$ (another band) in Fig. 7 as circle dot and square dot, respectively. They exhibit different feature although all these frequencies are in band region. At $f = 0.468\omega a/2\pi c$, $T \times L$ keeps constant (red line) with the increase of L although it oscillates around red line. Here the red line is drawn only for view. The oscillating characteristic depends on the interface and the thickness of the sample, but the red line remains unaffected. This indicates that the transmission is inversely proportional to the thickness of the sample, which is similar to diffusion behavior of the wave transport through a disordered medium even in the absence of any disorder in the PCs. This is completely different from the case at $f = 0.32\omega a/2\pi c$. The transmission is near constant and $T \times L$ increases linearly with the increase of L , which exhibits the standard ballistic behavior characteristic. The change feature of the transmission at $f = 0.44\omega a/2\pi c$ is in between the above two cases. It oscillates around green line (drawn only for view) and the average values increase with the increase of L , but the slope of green line is smaller than that of square-dot line ($f = 0.32\omega a/2\pi c$). This means that the transmission possesses both the ballistic and diffusion behaviors in this case. The numerical results are in agreement with the theoretical analysis based on the Dirac equation⁸¹⁻⁸⁴.

Zitterbewegung effect of wave near the Dirac point

After the new transport regime of the wave in the PCs has been demonstrated, the dynamic behavior of wave transport near the Dirac

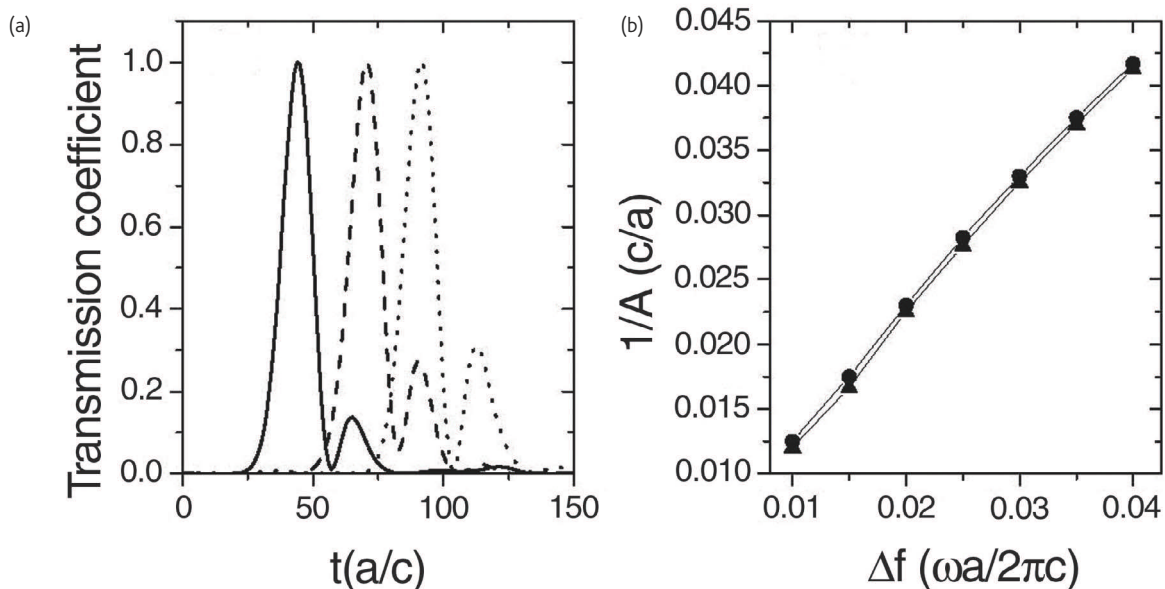


Fig. 8 (a) After the injection of a Gaussian pulse with center frequency $f_c = 0.466\omega a/2\pi c$, we show the time dependence of the transmission coefficient for the samples with different thicknesses. Solid line, dashed line and dotted line correspond to the results with $L=14a$, $24a$ and $32a$, respectively. (b) The inverse values of oscillation period ($1/A$) as a function of pulse width Δf . Circle and triangles correspond to the cases with $L=14a$ and $L=32a$, respectively. The other parameters are identical to those in Fig. 6.

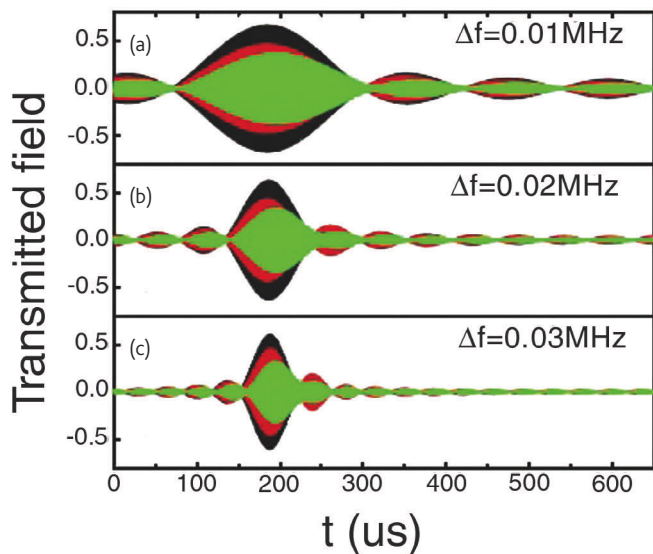


Fig.9 Experimental data of the transmission after the injection of a Gaussian pulse with center frequency $f = 0.55\text{MHz}$ (Dirac point) into the sample, which consists of a hexagonal array of steel cylinders immersed in water with a lattice constant $a = 1.5\text{mm}$ and a filling ratio 0.403. Dark, red and green correspond to the cases with $L = 14a$, $19a$ and $24a$, respectively. (a), (b) and (c) correspond to the cases with the filter frequency widths $\Delta f = 0.01\text{MHz}$, 0.02MHz and 0.03MHz , respectively.

point has been discussed^{87, 88}. Fig. 8a shows the numerical results for the transmission coefficients as a function of time for the samples with different thickness, when a Gaussian pulse is injected into the PCs. The center frequency of the pulse is taken as that at the Dirac point. The results show unusual oscillation features. (1) The period of the oscillation (A) depends weakly on the thickness of the sample. (2) The ratios of the intensity between the second peak and the first peak increase considerably. For the thin sample, the second peak basically disappears. No oscillation can be observed. This is due to the finite size effect of the sample. When the thickness of the sample is very small, the wave transport exhibits a ballistic behavior. With the increase of the sample thickness, the diffusion behavior appears gradually. When the thickness of the sample is bigger than several wavelengths, the diffusion behavior plays a leading role. In such a case, remarkable oscillations can be observed. (3) The period of oscillation is linearly dependent on the pulse width and is not determined by the central frequency (Fig. 8b). These features are completely different from the oscillation of the wave in a dielectric slab or cavity originating from the interface reflection or Fabry-Perot effect, in which the oscillation period is determined by the thickness of the sample and the central frequency of the pulse. In addition, the features are also not related to the localization effect, because wave transport exhibits diffusion behavior.

Such an inherent oscillation is directly related to the Zitterbewegung (ZB) effect. ZB represents an oscillatory motion of free electrons described by the Dirac equation in the absence of external


fields, which is caused by the interference between the positive and negative energy states⁸⁹. It was believed that the experimental observation of the effect is impossible since one would confine the electron to a scale of the Compton wavelength. Although many theoretical investigations have shown that such a phenomenon can also be found for non-relativistic electrons in solid systems, it has not been observed directly from the numerical simulation or experimental measurement.

According to the theory of the ZB, the time-dependent displacement ($\bar{x}(t)$) of a wave packet with time in the systems can be obtained analytically. After the average displacement is obtained, the velocity of the wave packet can be calculated by $\bar{v}(t) = d\bar{x}(t) / dt$. The velocity of the wave packet $\bar{v}(t)$ is proportional to the energy flux ($j(t)$) of the wave ($j(t) \propto \bar{v}(t)$). At the same time, $j(t)$ is a time-derivative of the pulse intensity ($I(t)$) ($j(t) = dI(t) / dt$). The intensity ($I(t)$) or transmission coefficient can be obtained from the numerical simulation or the experimental measurement. Thus, we can obtain $j(t)$ from the numerical simulation and quantitatively compare it with the theoretical result for $\bar{v}(t)$. These have been done⁸⁷ and the agreement between the numerical simulation and the theoretical results of the ZB has been found. The numerical simulation shows that an optical analogue effect to ZB of the relativistic electron can be found.

In fact, such a phenomenon not only exists for electromagnetic wave in the PCs, but also appears for acoustic wave in sonic crystals (SCs)⁸⁸. In order to test such a phenomenon experimentally, a series of SC slabs with different thicknesses has been fabricated⁸⁸. The dynamic behavior of the acoustic wave transport near the Dirac point in the above SC samples has been investigated experimentally. The measured results for filter frequency widths $\Delta f = 0.01\text{MHz}$, 0.02MHz and 0.03MHz are plotted in Fig. 9a-c. The dark, red and green curves correspond to the results with $L = 14a$, $19a$ and $24a$, respectively. It is obvious that all of them are oscillating and the period of the oscillation depends weakly on the thickness of the sample, while it is linearly dependent on the filter frequency widths. Comparing them with the theoretical results of the ZB, the agreements between them have been demonstrated⁸⁸. This means that an acoustic analogue effect to the ZB of relativistic electrons has been observed from experimental measurements. We anticipate the work to be a starting point for more experimental investigations on the phenomena of relativistic quantum mechanics by using classical waves.

Summary

After providing a brief historic of the study of photonic band gap materials, we have reviewed recent progresses on the negative refraction and the focusing of electromagnetic wave through 2D PCs. The physical principles causing such a phenomenon have also been analyzed. Different kinds of focusing by 2D PC slabs have been

summarized. The abnormal transmission of the electromagnetic waves near the Dirac point in the 2D PCs has been discussed. Recent investigation on observing Zitterbewegung effect of wave transport near the Dirac point has also been introduced. 

Acknowledgments

This work was supported by the National Natural Science Foundation of China at No. 10825416 and the National Key Basic Research Special Foundation of China at No. 2007CB613205 and No. 2004CB719804.

REFERENCES

- Joannopoulos, J. D., et al., *Photonic Crystal-Molding the Flow of Light*, Princeton University Press, Princeton, NJ, (1995)
- Soukoulis C. M., *Photonic Band Gap Materials*, Kluwer Academic, Dordrecht, (1996)
- Sakoda, K., *Optical properties of photonic crystals*, Springer, (2001)
- Yablonovitch, E., *Phys. Rev.Lett.* (1987) **58**, 2059
- John, S., *Phys. Rev. Lett.* (1987) **58**, 2486
- Ho, K. M., et al., *Phys. Rev.Lett.* (1990) **65**, 3152
- Leung, K. M., and Liu, Y. F., *Phys. Rev. Lett.* (1990) **65**, 2646
- Zhang, Z., and Satpathy, S., *Phys. Rev. Lett.* (1990) **65**, 2650
- John, S., and Wang, J., *Phys. Rev. Lett.* (1991) **64**, 2418
- Petrov, E. P., et al., *Phys. Rev. Lett.* (1998) **81**, 77
- Megens, M., et al., *Phys. Rev. Lett.* (1999) **83**, 5401
- Yablonovitch, E., et al., *Phys. Rev. Lett.* (1991) **67**, 2295.
- Anderson, C. M., and Giapiis, K. P., *Phys. Rev. Lett.* (1996) **77**, 2949
- Li, Z. Y., et al., *Phys. Rev. Lett.* (1998) **81**, 2574
- Zhang, X. D., et al., *Phys. Rev. B* (2000) **61**, 1892
- Chan, Y. S., et al., *Phys. Rev. Lett.* (1998) **80**, 956
- Zoorob, M. E., et al., *Nature* (2000) **404**, 740
- Zhang, X. D., et al., *Phys. Rev. B* (2001) **63**, 081105
- Mekis, A., et al., *Phys. Rev. Lett.* (1996) **18**, 3787
- Kwan, K.-C., et al., *Appl. Phys. Lett.* (2003) **82**, 4414
- Knight, J. C., et al., *Science* (1998) **282**,1476
- Scalora, M., et al., *Phys. Rev. Lett.* (1994) **73**, 1368
- Joannopoulos, J. D., et al., *Nature* (1997) **386**, 143
- Kosaka, H., et al., *Appl. Phys. Lett.* (1999) **74**, 1212
- Kosaka, H., et al., *Phys. Rev. B* (1998) **58**, 10096
- Notomi, M., *Phys. Rev. B* (2000) **62**, 10696
- Pendry, J. B., *Phys. Rev. Lett.* (2000) **85**, 3966
- Shelby, R. A., et al., *Science* (2001) **292**, 77
- Smith, D. R., et al., *Phys. Rev. Lett.* (2000) **84**, 4184
- Smith, D. R., and Kroll, N., *Phys. Rev. Lett.* (2000) **84**, 2933
- Markos, P., and Soukoulis, C. M., *Phys. Rev. E* (2002) **65**, 036622
- Marques, R., et al., *Phys. Rev. Lett.* (2002) **89**, 183901
- Foteinopoulou, S., et al., *Phys. Rev. Lett.* (2003) **90**, 107402
- Smith, D. R., and Schurig, D., *Phys. Rev. Lett.* (2003) **90**, 077405
- Houck, A. A., et al., *Phys. Rev. Lett.* (2003) **90**, 137401
- Parazzoli, C. G., et al., *Phys. Rev. Lett.* (2003) **90**, 107401
- Grbic, A., and Eleftheriades, G. V., *Phys. Rev. Lett.* (2004) **392**, 117403
- Chen, L., et al., *Phys. Rev. Lett.* (2004) **92**, 107404
- Zhang, Y., et al., *Phys. Rev. Lett.* (2003) **91**, 157404
- Agranovich, V. M., and Gartstein, Y. N., *Phys. Usp.* (2006) **49**, 1029
- Mandel'shtam, L. I., *Zh. Eksp. Teor. Fiz.* (1945) **15**, 475
- Veselago, V. G., *Sov. Phys. Usp.* (1968) **10**, 509
- Gralak, B., et al., *J. Opt. Soc. Am. A* (2000) **17**, 1012
- Foteinopoulou, S., and Soukoulis, C. M., *Phys. Rev. B* (2003) **67**, 235107
- Luo, C., et al., *Phys. Rev. B* (2002) **65**, 201104
- Luo, C., et al., *Phys. Rev. B* (2003) **68**, 045115
- Luo, C., et al., *Appl. Phys. Lett.* (2002) **83**, 2352
- Cubukcu, E., et al., *Nature* (2003) **423**, 604
- Parimi, P. V., et al., *Nature* (2003) **426**, 404
- Cubukcu, E., et al., *Phys. Rev. Lett.* (2003) **91**, 207401
- Reed, E. J., et al., *Phys. Rev. Lett.* (2003) **91**, 133901
- Luo, C., et al., *Science* (2003) **299**, 368
- Zhang, X. D., *Appl. Phys. Lett.* (2005) **86**, 121103
- Berrier, A., et al., *Phys. Rev. Lett.* (2004) **93**, 073902
- Wang, X., et al., *Optics Express* (2004) **12**, 2919
- Zhang, X. D., *Phys. Rev. B* (2004) **70**, 195110
- Wang, X., et al., *Phys. Rev. B* (2005) **71**, 085101
- Hu, X., and Chan, C. T., *Appl. Phys. Lett.* (2004) **85**, 1520
- Zhang, X. D., *Phys. Rev. E* (2005) **71**, 037601
- Zhang, X. D., *Phys. Rev. B* (2005) **71**, 235103
- Zhang, X. D., *Phys. Rev. B* (2005) **71**, 165116
- Feng, Z., et al., *Phys. Rev. B* (2006) **73**, 075118
- Decoopman, T., et al., *Phys. Rev. Lett.* (2006) **97**, 073905
- Zhang, X. D., *Phys. Rev. B* (2004) **70**, 205102
- Li, Z. Y., and Lin, L. L., *Phys. Rev. B* (2003) **68**, 245110
- He, S. L., et al., *Phys. Rev. B* (2004) **70**, 115113
- Xiao, S., et al., *Appl. Phys. Lett.* (2004) **85**, 4269
- Belov, P., et al., *Phys. Rev. B* (2005) **71**, 193105
- Moussa, R., et al., *Phys. Rev. B* (2006) **74**, 115111
- Ao, X. Y., and He, S. L., *Opt. Lett.* (2004) **29**, 2542
- Lu, Z., et al., *Phys. Rev. Lett.* (2005) **95**, 153901
- Ren, K., et al., *Phys. Rev. B* (2007) **75**, 115108
- Feng, Z., et al., *Phys. Rev. Lett.* (2005) **94**, 247402
- Zhang, X. D., *Phys. Rev. B* (2007) **75**, 024209
- Zhang, X. D., et al., *Opt. Express* (2007) **15**, 1292
- Ruan, Z., and He, S., *Opt. Lett.* (2005) **30**, 2308
- Krauss, T. K., *Nature photon.* (2008) **2**, 448
- Baba, T., *Nature photon.* (2008) **2**, 465
- Haldane, F. D. M., and Raghu, S., *Phys. Rev. Lett.* (2008) **100**, 013904
- Raghu, S., and Haldane, F. D. M., *Phys. Rev. A* (2008) **78**, 033834
- Sepkhanov, R. A., et al., *Phys. Rev. A* (2007) **75**, 063813
- Zhang, X. D., *Phys. Lett. A* (2008) **372**, 3512
- Sepkhanov, R. A., and Beenakker, C. W. J., *Opt. Commun.* (2008) **281**, 5267
- Diem, M., et al., *arXiv*: (2008) 0807.3351
- Novoselov, K. S., et al., *Science* (2004) **306**, 666
- Ando, T., *J. Phys. Soc. Jpn.* (2005) **74**, 77.
- Zhang, X. D., *Phys. Rev. Lett.* (2008) **100**, 113903
- Zhang, X. D., and Liu, Z. Y., *Phys. Rev. Lett.* (2008) **101**, 264303
- Schrodinger, E., *Sitzungsber. Preuss. Akad. Wiss. Phys. Math. Kl.* (1930) **24**, 418

Resonance properties of metallic ring systems

We review our recent efforts in understanding the resonance properties of metallic ring systems using a rigorous mode-expansion theory. In the quasi-static limit, we established a matrix-form circuit equation to calculate the frequencies and current distributions for all resonance modes in a ring system. We then applied the theory to study different split ring resonators (SRR). We show that the circuit equations can be analytically solved in the thin-wire limit. Our theoretical results were all successfully verified by finite-difference-time-domain simulations on realistic systems and available experiments.

Lei Zhou^{1*}, Xueqin Huang¹, Yi Zhang¹, Siu-Tat Chui²

¹Surface Physics Laboratory (State Key Laboratory) and Physics Department, Fudan University, Shanghai 200433, P. R. China

²Bartol Research Institute, University of Delaware, Newark, Delaware 19716, USA

* Email: phzhou@fudan.edu.cn

Introduction

In 1968, Veselago¹ proposed that a medium with simultaneously negative permittivity and permeability possesses a negative refractive index, and exhibits many unusual electromagnetic (EM) properties. This proposal did not attract immediate attention since it is well accepted that a natural material shows no magnetism at high frequencies². A breakthrough appeared in 1999 when Pendry³ showed that a split ring resonator (SRR) could provide magnetic responses at any desired frequency. People then successfully fabricated metamaterials by combining magnetic resonators and electric wires, and demonstrated many unusual EM phenomena based on metamaterials, such as the negative refraction⁴⁻¹⁰, the super focusing¹¹⁻¹⁴ and the subwavelength cavity¹⁵⁻¹⁷. Scientists continued to explore other extraordinary EM phenomena related to metamaterials, including the unusual

photonic bandgap effects¹⁸⁻²⁰, the invisibility cloaking²¹⁻²³, the unusual nonlinear effects²⁴⁻²⁹, etc. When the concept of metamaterial was pushed to optical frequencies, other magnetic resonant structures were proposed, such as the rod-pair structure^{30, 31}, the fishnet structures^{9, 32, 33}, and a circular array of nano-spheres³³⁻³⁵.

As the first realization of artificial magnetism, the SRR structures naturally attracted the most extensive attention. People have studied the circular SRRs^{3, 4, 6, 36-53}, the rectangular SRRs^{5, 54-68}, SRRs with different cross-sections, metal line widths, metal thicknesses, and substrates^{6, 36, 55, 60, 61}, SRRs with different numbers of splits^{36, 37, 56}, and different numbers of rings^{48, 64}, and so on. Some applications were also proposed for the SRR. For instance, researchers proposed to use SRRs as antennas⁶⁹ and as couplers for channel dropping⁷⁰, inserted SRRs into a cut-off waveguide to enhance transmissions^{71, 72},

and used SRRs as lenses for imaging^{73, 74}. Some groups attempted to scale down the size of SRR to realize artificial magnetism at higher frequencies^{4-6, 57, 58, 63, 75}. However, the scaling does not always work, and the increase of resonance frequency will saturate under certain conditions^{56, 60}. Some other groups tried to tune the resonance frequency of a SRR, by inserting additional capacitance in the ring gaps^{36, 39}, using photocapacitance of the semi-insulating GaAs in the gap³⁸, and combining the SRRs with nematic liquid crystals⁶². Recently, the designs and fabrications of isotropic metamaterials based on SRRs began to draw intensive attentions⁷⁶⁻⁸².

Many theoretical efforts were devoted to understanding the exotic EM wave properties of the SRR structures. In a pioneering paper, Pendry *et al.*³ analyzed the resonance properties of a SRR by assuming a metallic ring as a single lumped element with empirical circuit characteristics. Later, Shamonin *et al.*⁴² considered more inductive/capacitive effects by assuming the SRR to consist of an infinite number of lumped circuit elements. Many other analytical methods were developed to study the properties of the SRRs^{41, 43-46, 48, 49, 64, 65} from various aspects. However, in all these approaches, the inductive/capacitive effects in the rings were not completely considered. In addition, all these approaches need a set of empirical circuit parameters that cannot be calculated rigorously. Those empirical parameters were usually determined under some approximations^{3, 42}. The SRR systems were also studied by numerical calculations^{54, 55, 61, 62, 66-68}. Although such full-wave studies contain all relevant field information, it is sometimes difficult to extract useful properties of a SRR, such as the bi-anisotropy polarizabilities, from the obtained information.

In reviewing these efforts, we find that an analytical approach on more rigorous ground is highly desirable to study the metallic ring systems. In this paper, we review our recent efforts to establish such a theory, with inductive/capacitive effects fully included and all circuit parameters calculated rigorously, to study the EM properties of various metallic ring systems⁵⁰⁻⁵³. We first briefly review the theoretical developments in next section, and then present the applications of our theory to several typical SRR systems. We finally summarize our results in the last section.

Theoretical developments of the mode-expansion theory

Basic theory for a single-ring

We consider a single ring of radius R in the xy -plane, as shown in Fig. 1a⁵⁰. In what follows, a common time-varying factor $\exp(i\omega\tau)$ is omitted for every quantity. In the quasi-static limit, the inductive field $\vec{E}_L(\vec{r})$ and the capacitive field $\vec{E}_C(\vec{r})$ can be expressed as

$$\vec{E}_L(\vec{r}) = -i\omega\mu_0 \int \vec{j}(\vec{r}') d\vec{r}' / (4\pi |\vec{r} - \vec{r}'|),$$

$$\vec{E}_C(\vec{r}) = \frac{1}{i\omega} \frac{1}{4\pi\epsilon_0} \nabla \int [\nabla' \cdot \vec{j}(\vec{r}')] d\vec{r}' / |\vec{r} - \vec{r}'|$$

where $\vec{j}(\vec{r}')$ describes the current flowing in the wire.

Suppose that the wire has a circular cross-section with a radius a and $a \ll R$, the current distribution can be written as $\vec{j}(\vec{r}') = \vec{e}_\phi I(\phi) \sin\theta \delta(\cos\theta) \delta(r' - R) / R$ with $\vec{e}_\phi = -\sin\phi \vec{e}_x + \cos\phi \vec{e}_y$. We expand every physical quantity as a Fourier series,

$$I(\phi) = \sum_{m=-\infty}^{+\infty} I_m e^{im\phi}, \quad \vec{E}_{L,C}(\phi) \cdot \vec{e}_\phi = \sum_{m=-\infty}^{+\infty} E_{L,C}^m e^{im\phi}. \quad (1)$$

Then we carry out the integrations in $\vec{E}_L(\vec{r}), \vec{E}_C(\vec{r})$ to obtain

$$E_L^m = -i\omega L_m I_m, \quad E_C^m = -I_m / (i\omega C_m) \quad (2)$$

where the circuit parameters are defined by

$$L_m = \mu_0 (A_{m-1} + A_{m+1}) / 4, \quad C_m^{-1} = m^2 A_m / (2\epsilon_0 R(R-a)) \quad (3)$$

Here the key function is

$$A_m = \sum_{l=m}^{\infty} \frac{(l-m)!}{(l+m)!} \alpha^l [P_l^m(0)]^2 \quad (4)$$

in which P_l^m is the associated Legendre function and $\alpha = (R-a)/R < 1$.

In the thin-wire limit ($a \ll R$), we found an asymptotic form.

This logarithmic $A_m \approx D_m - \ln(2a/R) / (\alpha^m \pi)$ divergence is a typical

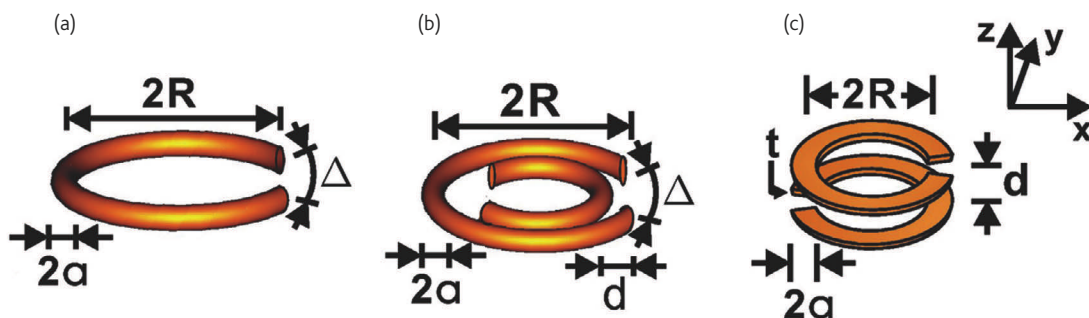


Fig. 1 Geometries of (a) single SRR, (b) co-planar SRR, and (c) BC-SRR.

characteristic of a thin-wire system⁸³. Ohm's law tells us that $\vec{j}(\vec{r}) = \rho(\vec{r})[\vec{E}_L(\vec{r}) + \vec{E}_C(\vec{r}) + \vec{E}_{ext}(\vec{r})]$ where $\vec{E}_{ext}(\vec{r})$ is the external field and $\rho(\vec{r})$ is the resistivity function of the ring. In terms of the Fourier components, we get the following matrix equation,

$$\sum_{m'} H_{mm'} I_{m'} = E_{ext}^m, \quad (5)$$

where $H_{mm'} = \tilde{\rho}(m-m') + i\omega L_m(1 - \Omega_m^2/\omega^2)\delta_{mm'}$; $\tilde{\rho}(m-m')$ is the Fourier component of $\tilde{\rho}(\phi) = \rho(\phi)/S$ (S is the wire cross-section area) and $\Omega_m = 1/\sqrt{L_m C_m}$. Diagonalizing the \mathbf{H} matrix, we obtain the eigenvalues $\{\lambda_j\}$ and eigenvectors of all EM modes, from which we can calculate the resonance frequencies, induced EM dipole moments, and the polarizabilities and the bi-anisotropic polarizabilities. For example, all resonance frequencies ω_j of the SRR are obtained through solving the equation

$$\det[H_{mm'}(\omega)] = \prod_m \lambda_m(\omega) = 0 \quad (6)$$

Extensions to other situations

The above mode-expansion theory can be easily extended to more complex situations. For the two ring systems, we find that the matrix-circuit equation could be written as

$$\sum_{m'j'} H_{\{mj\},\{m'j'\}} I_{m'j'} = E_{mj}^{ext} \quad (7)$$

where the matrix elements are

$$H_{\{mj\},\{m'j'\}} = \rho_j(m-m')\delta_{jj'} + i \left(\omega L_m^{jj'} - \frac{1}{\omega C_m^{jj'}} \right) \delta_{mm'}. \quad (8)$$

Here $j, j' = 1, 2$ label the two rings, L_m^{jj} and C_m^{jj} are the self inductive/capacitive parameters and $L_m^{jj'}$ and $C_m^{jj'}$ are the mutual inductance/capacitance parameters. The above theory can be applied to study the coplanar double-ring SRR in which two rings are placed on the same plane but with different radii (Fig. 1b), and the broadside coupled SRR (BC-SRR) with two identical rings placed on different planes (Fig. 1c). In addition, the gap position of each ring can be arbitrary in our system, which is simply described by the resistivity function $\rho(\phi)$. It is straightforward to extend our theory to study multi-ring systems. For the detailed forms of those circuit parameters, please refer to the original publications^{51, 52}.

Strictly speaking, the theory presented so far is only applicable to rings formed by thin wires with circular cross-sections. In practical situations, the metallic rings often have rectangular cross-sections^{3-6, 36-49, 54-68}, where the delta-like current distribution is no longer reasonable. Suppose the wire's cross-section is defined as $t \times 2a$, where $2a$ and t are the width and thickness of the wire, we focus on the flat-wire case satisfying $R \gg 2a \gg t$. For a good metal, the skin effect dictates that the current should mainly distribute on the metal surface. Noting that $a \ll \lambda$ with λ being the wavelength of the probing

EM wave of interest, we further assume that the current distributes uniformly along the wire width. Therefore, the current distribution in the flat wire can be written as,

$$\vec{j}(\vec{r}) = \begin{cases} j(\phi) \cdot t_\delta [\delta(z+t/2) + \delta(z-t/2)] \vec{e}_\phi, & \rho \in [R-a, R+a] \\ 0, & \text{otherwise} \end{cases} \quad (9)$$

where $t_\delta \ll t$ is the skin depth of the metal. We average both $\vec{E}_{LC}(\vec{r})$ and $\vec{j}(\vec{r}')$ over the cross-section area of the wire, and then set up the relationship between the two averaged quantities. For example, the averaged inductive field is

$$\vec{E}_L(\phi) = \frac{\int \vec{E}_L(\rho, z, \phi) \cdot \vec{e}_\phi t_\delta [\delta(z+t/2) + \delta(z-t/2)] dz d\rho}{\int t_\delta [\delta(z+t/2) + \delta(z-t/2)] dz d\rho}. \quad (10)$$

and the total current is given by $I(\phi) = j(\phi) \cdot 4at_\delta$. By linking these two averaged quantities, we can calculate the relevant circuit parameters⁵². Therefore, the circuit equations (5), (7) are still correct for flat-wire SRR cases, but with a set of modified circuit parameters⁵².

Applications and discussions

Our theory can be applied to study the resonance properties of various metallic ring systems. In the following three subsections, we summarize our results on a single-ring SRR, a coplanar double-ring SRR, and a BC-SRR, correspondingly.

Single-ring SRR

Consider a single-ring SRR illustrated in Fig. 1a. In the microwave frequency regime, we can safely set the resistivity of the metal as 0, and that of the air-gap as r . We will let $r \rightarrow \infty$ in the end. The magnitude of the lowest eigenvalue of matrix \mathbf{H} is shown as a function of frequency in Fig. 2 for a typical SRR. The series of resonances in Fig. 2 can be categorized into two classes. The even-numbered resonances ω_{2m} coincide well with the intrinsic resonances Ω_m , which in the thin-wire limit ($a/R \rightarrow 0$) becomes $\Omega_m \rightarrow m\omega_u$ where $\omega_u = c/R$ is the frequency unit of the present problem. Noting that $\lambda_{2m} = 2\pi c/\omega_{2m} = m \cdot 2\pi R$, we find that these resonances are solely determined by the ring geometry, with currents forming standard standing waves in the ring. The odd-numbered ones, however, must be introduced by the air gap Δ .

In fact, these resonance frequencies can be calculated analytically in the following limits: (1) $\Delta \rightarrow 0$; (2) $a/R \rightarrow 0$; (3) metal is perfect and the gap is ideal insulator ($r \rightarrow \infty$). Under these conditions, we have *rigorously* solved the matrix problem (6) and found two sets of solutions⁵³. One set of resonance frequencies is

$$\omega_{2m} = m\omega_u, \quad m = 1, 2, \dots \quad (11)$$

with eigenvectors exhibiting odd-symmetries (i.e., $I_{-m} = -I_m$). These modes correspond to the even-numbered resonance modes as shown in Fig. 2. Another set of resonance modes are determined by the following polynomial equation,

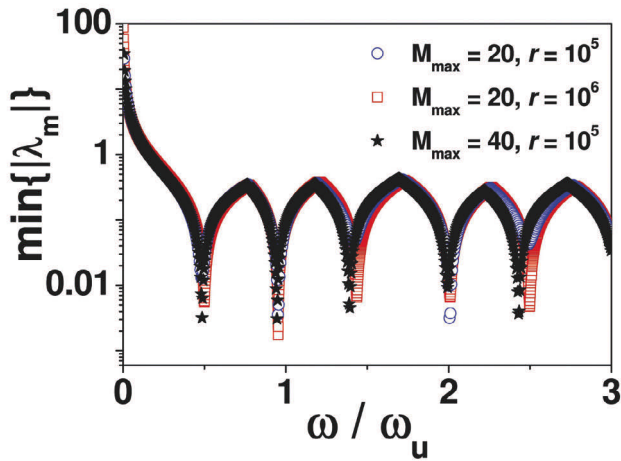


Fig. 2 $\min\{|\lambda_m|\}$ as functions of ω/ω_u for a single-ring SRR with $\Delta = \pi/40$ and $\alpha = 0.99$, calculated with different values of M_{\max} (the cutoff value of m) and r (in units of $\mu_0\omega_u$). Reproduced from⁵⁰ with permission from the American Physical Society.

$$1 + \sum_{m=1}^{\infty} \frac{2L_0\omega^2}{L_m\omega^2 - 1/C_m} = 0 \quad (12)$$

and their eigenvectors exhibit even symmetry (i.e., $L_m = -l_m$). Since as $a/R \rightarrow 0$, we have $L_m \rightarrow \ln(R/a)$ and $1/C_m \rightarrow m^2 \ln(R/a)$, using the identity $k\pi \cot(k\pi) = 1 + \sum_{m=1}^{\infty} 2k^2/(k^2 - m^2)$,

we found that Eq. (12) can be written as $(\omega/\omega_u)\cot(\omega\pi/\omega_u) = 0$, leading to the following solutions

$$\omega_{2m+1} = (m + 1/2)\omega_u, \quad m = 0, 1, 2, \dots \quad (13)$$

These solutions are just the odd-numbered resonance modes depicted in Fig. 2.

The information of the eigenvectors enables us to evaluate the EM responses of the system. Consider different probing plane waves with (a) $\vec{E} \parallel \hat{y}, \vec{k} \parallel \hat{z}$, (b) $\vec{E} \parallel \hat{y}, \vec{k} \parallel \hat{x}$, (c) $\vec{E} \parallel \hat{x}, \vec{k} \parallel \hat{z}$, (d) $\vec{E} \parallel \hat{x}, \vec{k} \parallel \hat{y}$, we show in Fig. 3 the induced dipole moments as functions of frequency. The odd-numbered resonance modes possess both magnetic (m_z) and electric (p_y) responses, while the even-numbered ones only electric (p_x) responses. The appearance of p_y is always accompanied by the appearance of m_z , manifesting the bi-anisotropy property of the SRR^{43, 47, 49}. Symmetry restricts a probing field to excite only a particular set of resonance modes of the SRR, and therefore, not all the resonance peaks appear simultaneously in each spectrum. We have performed finite-difference time-domain (FDTD) simulations⁸⁴ to verify these theoretical results. We first calculated the transmission spectra through arrays of such realistic SRR's, and then identify all resonance modes from the dips in the spectra. The transmission spectra under the four plane wave inputs are shown respectively in Fig. 4a-d. When we compare Fig. 4 with Fig. 3, we find that they agree with each other

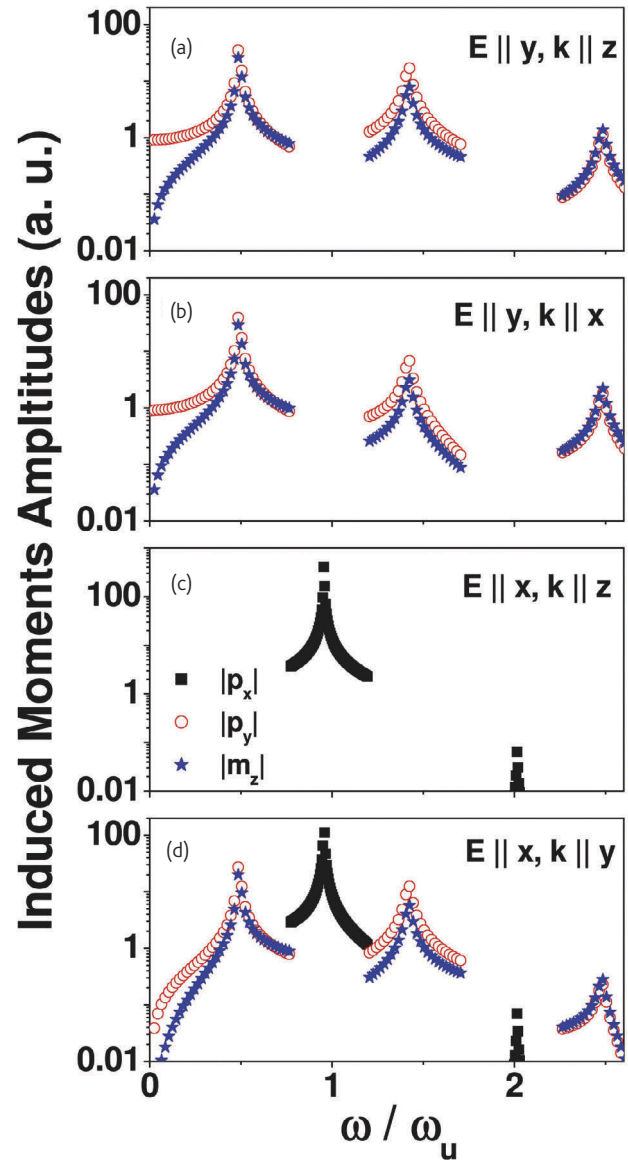


Fig. 3 Amplitudes of the induced moments, $|p_x|$, $|p_y|$, $|m_z|$, of the SRR as functions of ω/ω_u for different probing fields as shown in the figure. Reproduced from⁵⁰ with permission from the American Physical Society.

quite well. We clearly identify the dips at $\omega \approx 0.42\omega_u$ shown in Fig. 4a, b, d as the lowest eigen resonance mode (ω_1), the dips at $\omega \approx 1.19\omega_u$ shown in Fig. 4c, d as the second resonance mode (ω_2), and the dips at $\omega \approx 1.46\omega_u$ as the third one (ω_3). The quantitative differences between analytical and FDTD results must be caused by the couplings between different SRRs, since we have to adopt periodic arrays of SRRs to study the transmission spectra in the FDTD simulations.

Coplanar double-ring SRR

Now consider the coplanar double-ring SRR as shown in Fig. 1b.

Suppose the two rings have radius $R_1 = R$, $R_2 = R - d$, and each wire has

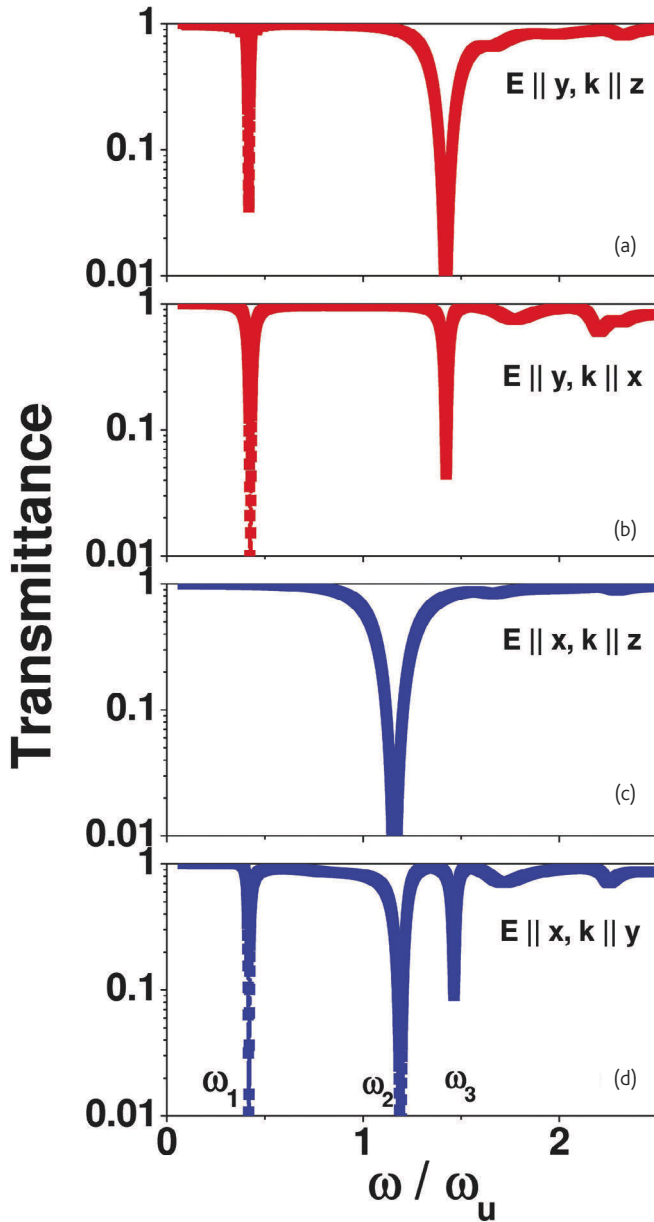


Fig. 4 FDTD calculated transmission spectra of the SRR arrays as functions of ω/ω_u for plane wave inputs specified in the figure. Here the SRR has $R = 4$ mm, $a = 0.1$ mm, and $\Delta = \pi/40$. Reproduced from⁵⁰ with permission from the American Physical Society.

a radius $a_1 = a_2 = a \ll R$. For an example with structural details shown in the caption of Fig. 5, we solved the matrix equation (7) and showed in Fig. 5 the calculated $\min[|\lambda_i|]$ as a function of ω/ω_u . Compared with the spectra of a single-ring SRR shown in the same figure, we find that each single-ring mode has split into a pair of modes in the double-ring case through mutual inductance/capacitance effects. Such inter-ring interactions may combine components of different rings with a certain relative phase to form a double-ring eigenmode⁵¹. Therefore, the magnetic (electric) polarizations are highly diminished in the ω_1^H (ω_1^L)

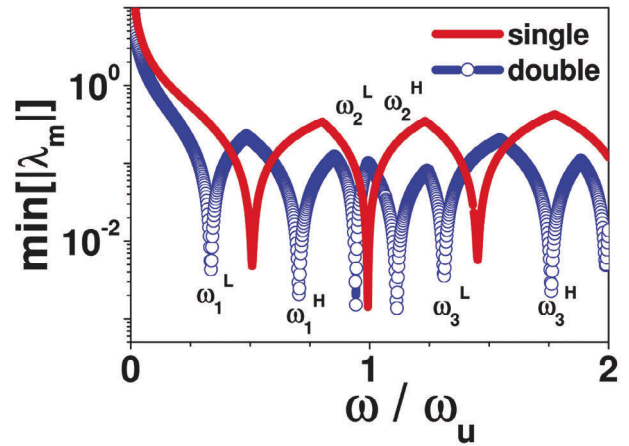


Fig. 5 $\min[|\lambda_i|]$ (in arbitrary units) as the functions of ω/ω_u calculated for a double-ring SRR (symbols) with $R = 4$ mm, $d = 0.4$ mm, $a = 0.1\sqrt{\pi}$ mm, $\Delta = \pi/90$, and a single-ring SRR (lines) with $R = 3.8$ mm, $a = 0.1\sqrt{\pi}$ mm, $\Delta = \pi/90$. Reproduced from⁵¹ with permission from the American Institute of Physics.

mode, and as the results, the bi-anisotropy is also highly suppressed as two rings approach.

Fig. 6 shows the dipole moments of the structure induced by different external plane waves. Similar to the single-ring case (Fig. 3), we find that the odd-numbered modes ($\omega_1^L, \omega_1^H, \omega_3^L, \omega_3^H, \dots$) carry both electric (P_y) and magnetic (M_z) polarizations, while the even-numbered ones ($\omega_2^L, \omega_2^H, \omega_4^L, \omega_4^H, \dots$) carry only electric (P_x) polarizations. In particular, one may easily find that m_z is much stronger than p_y for the mode ω_1^L , but things become reversed for the mode ω_1^H . These are precisely the evidence of the polarization decreasing effects discussed above. We performed FDTD simulations⁸⁴ to calculate the transmission spectra through arrays of realistic SRR structures, and again the transmission dips in the spectra show excellently one-by-one correspondence to the moment peaks in Fig. 6⁵¹.

The present theory allows us to *quantitatively* examine the bi-anisotropy of the SRR. We derived all elements of the electric/magnetic polarizabilities of the structure⁵¹, following the definitions in^{43, 47, 49}. We showed in Fig. 7a-b the calculated values of electric polarizability (α_{yy}^{ee}) and bi-anisotropic polarizability (α_{yz}^{em})^{43, 47, 49}, respectively, for double-ring SRR's with different values of d . Clearly, both α_{yy}^{ee} and α_{yz}^{em} are significantly suppressed as d decreases. As a result, such a mode becomes *purely magnetic* in the limit of $d \rightarrow 0$.

The magnetic resonance frequency ω_1^L is drastically lowered compared to the single-ring mode (denoted by ω_1). Under the condition $d \gg a$, we applied a perturbation theory with a 3-mode approximation to derive the following analytical formula to quantitatively account for such a frequency shift⁵¹,

$$\omega_1^L \approx \omega_1 [1 - 2\ln(2d/R) / (3 \ln(2a/R))]. \quad (14)$$

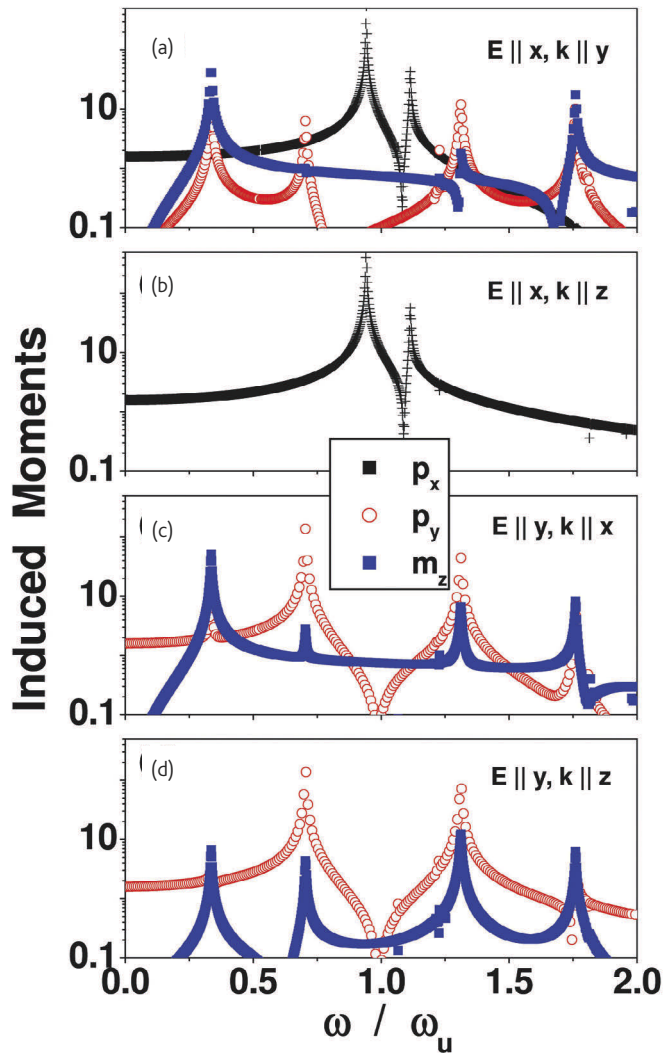


Fig. 6 Dipole moments (in arbitrary units) of the double-ring SRR (same as Fig. 5) induced by external plane waves with \vec{E} and \vec{k} directions specified in the legends. Reproduced from⁵¹ with permission from the American Institute of Physics.

The physics behind (14) is that $\delta\omega/\omega_1$ is dictated by a competition between the mutual interaction ($\propto \ln(2d/R)$) and the self interaction ($\propto \ln(2a/R)$). FDTD simulations⁵¹ on realistic SRR structures excellently verified the analytical formula (14).

This formula can also account for experiments very well. For the series of SRR's studied experimentally³⁶, adopting their definitions (i.e., set $R = r-w/2$, $a = w/2$, $d = t+w$ where w is the metal line width and t is the gap distance between two rings³⁶) and taking the experimental data $\omega_1 = 2\pi \times 4.58\text{GHz}$ ³⁶, we get an expression,

$$f = 4.58[1 - 2\ln(2(t+w)/(r-w/2)) / [3\ln(w/(r-w/2))]] \quad (15)$$

to estimate the resonance frequencies of SRR's measured³⁶. Fig. 8 shows that the experimental data³⁶ are reasonably described by (15).

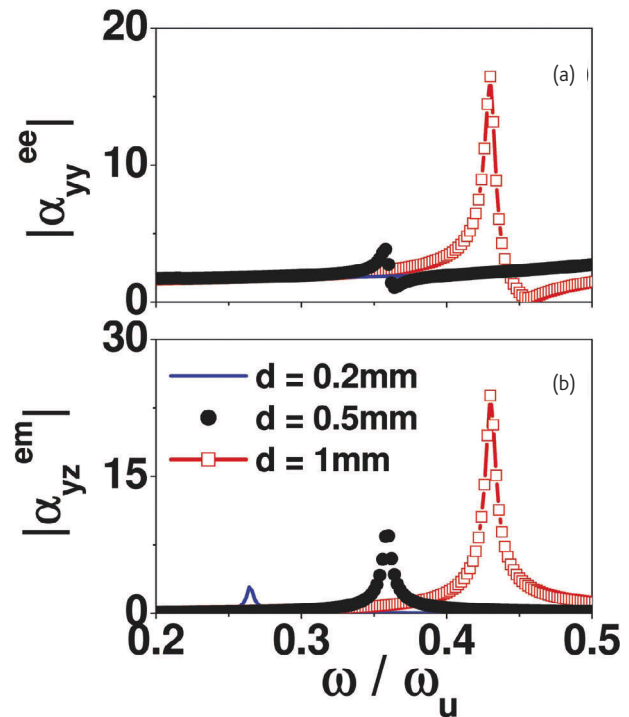


Fig. 7 Amplitudes of (a) electric polarizability $|\alpha_{yy}^{ee}|$ and (b) bi-anisotropic polarizability $|\alpha_{yz}^{em}|$ as the functions of ω/ω_u , for double-ring SRR's with $R = 4\text{ mm}$, $a = 0.1\sqrt{\pi}\text{ mm}$, and different values of d specified in the legend. Reproduced from⁵¹ with permission from the American Institute of Physics.

BC - SRR

We now consider the BC-SRR as shown in Fig. 1c. The spectrum of resonance frequency in the BC-SRR case is quite similar to that of a coplanar SRR (see Fig. 5), and each single-ring mode has again split into a pair of modes with different symmetries⁵². However, we found that the dipole moments exhibited by the resonance modes in a BC-SRR⁵² are quite different from those in the coplanar SRR⁵¹. In particular, in addition to the perpendicular magnetic polarization m_z , two more in-plane polarizations m_x, m_y can also be induced for the BC-SRR under specific conditions. We summarized the characteristics of the EM polarizations for the lowest four modes in Table 1. Two important conclusions can be drawn. First, all the resonance modes in a BC-SRR are *completely free of bi-anisotropy* (i.e., either *purely magnetic* or *purely electric*). This important character has also been noted previously^{43, 47, 49}. Second, some resonance modes (say, ω_1^L) could possess two magnetic moments simultaneously.

The second property of the BC-SRR enables us to design a *super* resonance unit for metamaterials. Metamaterials that possess magnetic responses along all three dimensions drew much attention recently⁷⁶⁻⁸². As many resonant structures are inherently anisotropic, a standard method to design 3D magnetic materials is to rotate the unit cell element and combine it with the original one to form an isotropic unit cell⁷⁶⁻⁸². Recently, several non-SRR-based schemes were also

Table 1 Characteristics of electric/magnetic polarizations of low-lying modes for a BC-SRR and a single-ring SRR. Reproduced from⁵² by permission of the American Physical Society.

System	Mode	p_x	p_y	m_z	m_x	m_z
Single	ω_1	No	Yes	Yes	No	No
Double	ω_1^L	No	Disappear	Enhanced	New	No
	ω_1^H	No	Enhanced	Disappear	No	No
Single	ω_2	Yes	No	No	No	No
Double	ω_2^L	Enhanced	No	No	No	No
	ω_2^H	Disappear	No	No	No	New

proposed to fabricate 3D isotropic metamaterials⁸⁵⁻⁸⁸. Here, we provide an alternative approach. We demonstrate that a layered structure, composed by planar arrays of BC-SRR's, can exhibit magnetic responses along all three dimensions at the same frequency. Since the structure is basically a multilayer system, it is very easy to fabricate, particularly in higher frequency regime where the complex 3D structures are relatively difficult to fabricate. As shown in Fig. 9a, the unit cell of the designed metamaterial contains two BC-SRR's, with one rotated by 90 degrees with respect to the other. To understand the resonance properties of the designed system, we employed FDTD simulations⁸⁴ to calculate the transmissions of EM plane waves with magnetic fields polarized along different directions and with different propagation directions⁵². The transmission spectra in different cases are compared in Fig. 9b. It is clearly shown that for **B** field along all three directions, a *common* resonance is excited at the frequency $\omega \sim 0.386\omega_u$, implying that the system exhibits strong responses to external magnetic fields along all three directions at this particular frequency.

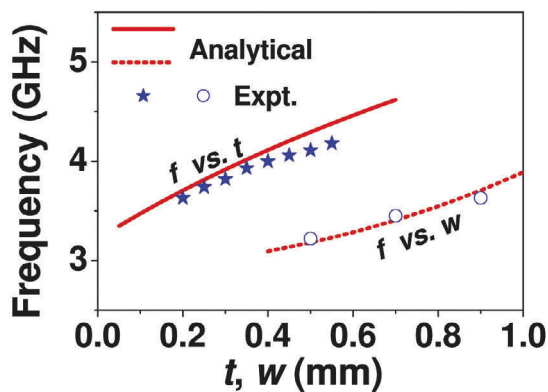


Fig. 8 SRR resonance frequency f (measured in GHz) as a function of t (setting $w = 0.9$ mm, solid line) and w (setting $t = 0.2$ mm, dotted line), calculated by our analytical formula. Symbols are experimental data taken from Figs. 7 and 8 of⁵⁶. Reproduced from⁵¹ with permission from the American Institute of Physics.

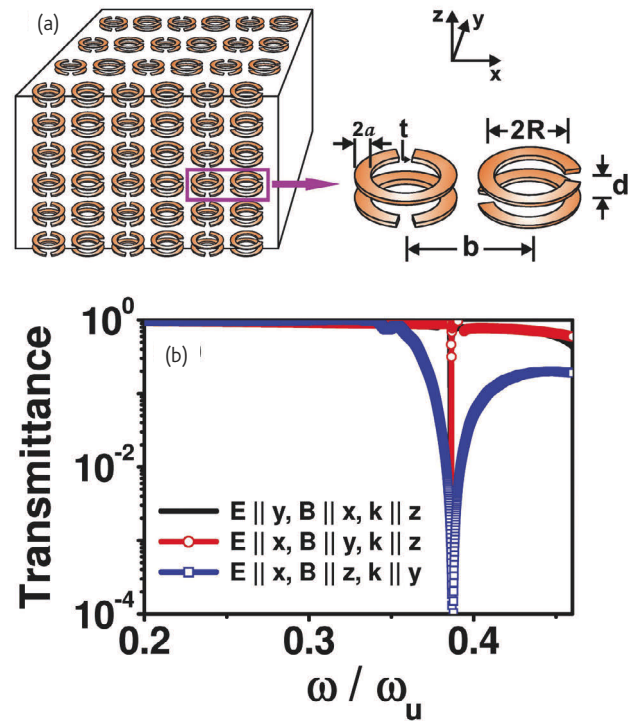


Fig. 9 (a) A schematic picture of the designed 3D magnetic material, with the inset showing the unit cell of structure. Here, $R = 4$ mm, $2a = 0.2$ mm, $t = 0.05$ mm, $d = 3$ mm, $b = 11$ mm and the gap width $\Delta = \pi/40$. (b) FDTD-calculated transmission spectra through the designed 3D magnetic material with different probing EM waves as specified in the figure. Reproduced from⁵² with permission from the American Physical Society.


Conclusions

In this concise review, we have briefly summarized our recent efforts in establishing a rigorous mode-expansion theory and employing it to study the EM resonance properties of various SRR structures. The theory was established under the quasi-static limit and can be applied to study the resonance eigenmodes in *arbitrary* metallic ring systems, in which the inductive/capacitive effects were included completely and the relevant circuit parameters were calculated rigorously. The theory has been employed to study various SRR systems, including a single-ring SRR, a coplanar double-ring SRR and a broadside coupled SRR, and the obtained results are generally in good agreements with the FDTD simulations on realistic structures. We have also developed several analytical formulas, which agree well with FDTD and available experimental results, and might be useful for future metamaterial designs.

In a very recent work, Page *et al.*⁸⁹ established a theoretical approach which can also be applied to calculate all resonance frequencies of ring-like resonators. That approach can give additional physical insight into how geometry parameters affect the resonance frequencies by using the concepts of characteristic impedances and effective phase velocities⁸⁹. However, that theory relies on finding a well-defined transmission-line description for

the structure and still needs some model parameters determined from other methods⁸⁹. We believe that our theory and that one⁸⁹ are complementary in many aspects and are applicable to different situations.

While there have been lots of efforts to study the SRRs theoretically, we believe an analytical theory established on more rigorous grounds is still highly desirable, particularly since it can yield more physical

insights and analytical formulas helpful for researchers working in this area. We look forward to more applications of our theory and extensions to other related problems. 

Acknowledgements

This work was supported by the China-973 Program (2004CB719800), the NSFC (60725417, J0730310) and PCSIRT. STC is supported in part by the US DOE.

References

- Veselago, V. G., *Sov. Phys. Usp.* (1968) **10**, 509.
- Landau, L., and Lifschitz, E. M., *Electrodynamics of Continuous Media*, Elsevier, New York (1984).
- Pendry, J. B., *et al.*, *IEEE Trans. Microwave Theory Tech.* (1999) **47**, 2075.
- Smith, D. R., *et al.*, *Phys. Rev. Lett.* (2000) **84**, 4184.
- Shelby, R. A., *et al.*, *Science* (2001) **292**, 77.
- Moser, H. O., *et al.*, *Phys. Rev. Lett.* (2005) **94**, 063901.
- Dolling, G., *et al.*, *Opt. Lett.* (2007) **32**, 53.
- Dolling, G., *et al.*, *Opt. Lett.* (2006) **31**, 1800.
- Zhang, S., *et al.*, *Phys. Rev. Lett.* (2005) **95**, 137404.
- Shalaev, V. M., *et al.*, *Opt. Lett.* (2005) **30**, 3356.
- Pendry, J. B., *Phys. Rev. Lett.* (2000) **85**, 3966.
- Fang, N., *et al.*, *Science* (2005) **308**, 534.
- Ono, A., *et al.*, *Phys. Rev. Lett.* (2005) **95**, 267407.
- Belov, P. A., *et al.*, *Phys. Rev. B* (2006) **73**, 033108.
- Engheta, N., *IEEE Antennas Wireless Propag. Lett.* (2002) **1**, 10.
- Zhou, L., *et al.*, *Appl. Phys. Lett.* (2005) **86**, 101101.
- Li, H., *et al.*, *Appl. Phys. Lett.* (2006) **89**, 104101.
- Li, J., *et al.*, *Phys. Rev. Lett.* (2003) **90**, 083901.
- Shadrivov, I. V., *et al.*, *Phys. Rev. Lett.* (2005) **95**, 193903.
- Sun, S., *et al.*, *Phys. Rev. E* (2007) **75**, 066602.
- Leonhardt, U., *Science* (2006) **312**, 1777.
- Pendry, J. B., *et al.*, *Science* (2006) **312**, 1780.
- Schurig, D., *et al.*, *Science* (2006) **314**, 977.
- Klein, M. W., *et al.*, *Science* (2006) **313**, 502.
- Feth, N., *et al.*, *Opt. Lett.* (2008) **33**, 1975.
- Wang, B., *et al.*, *Opt. Express* (2008) **16**, 16058.
- O'Brien, S., *et al.*, *Phys. Rev. B* (2004) **69**, 241101.
- Zharov, A. A., *et al.*, *Phys. Rev. Lett.* (2003) **91**, 037401.
- Liu, Y., *et al.*, *Phys. Rev. Lett.* (2007) **99**, 153901.
- Dolling, G., *et al.*, *Opt. Lett.* (2005) **30**, 3198.
- Podolskiy, V. A., *et al.*, *Opt. Express* (2003) **11**, 735.
- Dolling, G., *et al.*, *Science* (2006) **312**, 892.
- Mary, A., *et al.*, *Phys. Rev. Lett.* (2008) **101**, 103902.
- Alù, A., and Engheta, N., *Phys. Rev. B* (2008) **78**, 085112.
- Alù, A., *et al.*, *Opt. Express* (2006) **14**, 1557.
- Aydin, K., *et al.*, *New J. Phys.* (2005) **7**, 168.
- Radkovskaya, A., *et al.*, *Microwave Opt. Technol. Lett.* (2005) **46**, 473.
- Boulais, K. A., *et al.*, *Appl. Phys. Lett.* (2008) **93**, 043518.
- Aydina, K., and Ozbay, E., *J. Appl. Phys.* (2007) **101**, 024911.
- Aydin, K., *et al.*, *Opt. Express* (2004) **12**, 5896.
- Sauviac, B., *et al.*, *Electromagnetics* (2004) **24**, 317.
- Shamonin, M., *et al.*, *J. Appl. Phys.* (2004) **95**, 3778.
- Marqués, R., *et al.*, *IEEE Trans. Antennas Propag.* (2003) **51**, 2572.
- Aznar, F., *et al.*, *Appl. Phys. Lett.* (2008) **92**, 043512.
- Zhurbenko, V., *et al.*, *Microwave Opt. Technol. Lett.* (2008) **50**, 511.
- Shamonin, M., *et al.*, *Microwave Opt. Technol. Lett.* (2005) **44**, 133.
- García-García, J., *et al.*, *J. Appl. Phys.* (2005) **98**, 033103.
- Baena, J. D., *et al.*, *Phys. Rev. B* (2004) **69**, 014402.
- Marques, R., *et al.*, *Phys. Rev. B* (2002) **65**, 144440.
- Zhou, L., and Chui, S. T., *Phys. Rev. B* (2006) **74**, 035419.
- Zhou, L., and Chui, S. T., *Appl. Phys. Lett.* (2007) **90**, 041903.
- Huang, X. Q., *et al.*, *Phys. Rev. B* (2008) **77**, 235105.
- Chui, S. T., *et al.*, *J. Appl. Phys.* (2008) **104**, 034305.
- Katsarakis, N., *et al.*, *Appl. Phys. Lett.* (2004) **84**, 2943.
- Markos, P., and Soukoulis, C. M., *Phys. Rev. E* (2002) **65**, 036622.
- Zhou, J., *et al.*, *Phys. Rev. Lett.* (2005) **95**, 223902.
- Yen, T. J., *et al.*, *Science* (2004) **303**, 1494.
- Linden, S., *et al.*, *Science* (2004) **306**, 1351.
- Zhou, J., *et al.*, *Opt. Express* (2007) **15**, 17881.
- Klein, M. W., *et al.*, *Opt. Lett.* (2006) **31**, 1259.
- Economou, E. N., *et al.*, *Phys. Rev. B* (2008) **77**, 092401.
- Zhao, Q., *et al.*, *Appl. Phys. Lett.* (2007) **90**, 011112.
- Enkrich, C., *et al.*, *Phys. Rev. Lett.* (2005) **95**, 203901.
- Bilotti, F., *et al.*, *IEEE Trans. Antennas Propag.* (2007) **55**, 2258.
- Azad, A. K., *et al.*, *Appl. Phys. Lett.* (2008) **92**, 011119.
- Smith, D. R., *et al.*, *Appl. Phys. Lett.* (2000) **77**, 2246.
- Smith, D. R., *et al.*, *Phys. Rev. B* (2002) **65**, 195104.
- Popa, B., and Cummer, S. A., *Phys. Rev. B* (2005) **72**, 165102.
- Alicia, K. B., and Ozbay, E., *J. Appl. Phys.* (2007) **101**, 083104.
- Little, B. E., *et al.*, *J. Lightwave Technol.* (1997) **15**, 998.
- Marques, R., *et al.*, *Phys. Rev. Lett.* (2002) **89**, 183901.
- Xu, H., *et al.*, *Appl. Phys. Lett.* (2008) **92**, 041122.
- Wiltshire, M. C. K., *et al.*, *Science* (2001) **291**, 849.
- Wiltshire, M. C. K., *et al.*, *Opt. Express* (2003) **11**, 709.
- Zhang, S., *et al.*, *Phys. Rev. Lett.* (2005) **94**, 037402.
- Verney, E., *et al.*, *Phys. Lett. A* (2004) **331**, 244.
- Baena, J. D., *et al.*, *Appl. Phys. Lett.* (2006) **88**, 134108.
- Baena, J. D., *et al.*, *Appl. Phys. Lett.* (2007) **91**, 191105.
- Baena, J. D., *et al.*, *Phys. Rev. B* (2007) **76**, 245115.
- Gay-Balmaz, P., and Martin, O. J. F., *Appl. Phys. Lett.* (2002) **81**, 939.
- Zhao, Q., *et al.*, *Phys. Rev. Lett.* (2008) **101**, 027402.
- Koschny, Th., *et al.*, *Phys. Rev. B* (2005) **71**, 121103.
- Jackson, J. D., *Classical Electromagnetic*, Wiley, New York (1999), 3rd edition.
- CONCERTO 4.0, Vector Fields Limited, England, 2005.
- Zedler, M., *et al.*, *IEEE Trans. Micro. Theory Tech.* (2007) **55**, 2930.
- Grbic, A., and Eleftheriades, G. V., *J. Appl. Phys.* (2005) **98**, 043106.
- Alitalo, P., *et al.*, *J. Appl. Phys.* (2006) **99**, 064912.
- Vendik, I., *et al.*, *Micro. Opt. Tech. Lett.* (2006) **48**, 2553.
- Page, J. E., *et al.*, *Int. J. Electron Commun. (AEU)* (2008), doi: 10.1016/j.aeue.2008.02.006

Mie resonance-based dielectric metamaterials

Increasing attention on metamaterials has been paid due to their exciting physical behaviors and potential applications. While most of such artificial material structures developed so far are based on metallic resonant structures, Mie resonances of dielectric particles open a simpler and more versatile route for construction of isotropic metamaterials with higher operating frequencies. Here, we review the recent progresses of Mie resonance-based metamaterials by providing a description of the underlying mechanisms to realize negative permeability, negative permittivity and double negative media. We address some potential novel applications.

Qian Zhao^{1,2}, Ji Zhou^{1,*}, Fuli Zhang³, Didier Lippens³

¹ State Key Lab of New Ceramics and Fine Processing, Department of Materials Science and Engineering, Tsinghua University, Beijing, PRC

² State Key Lab of Tribology, Department of Precision Instruments and Mechanology, Tsinghua University, Beijing, PRC

³ Institut d'Electronique de Micro-électronique et de Nanotechnologie, UMR CNRS 8520, University of Lille 1, Villeneuve d'Ascq Cedex, France

*E-mail: zhouji@mail.tsinghua.edu.cn

Metamaterials are artificial electromagnetic media structured on a scale much shorter than their operating wavelength. Under this condition they can be considered as homogeneous media whose electromagnetic properties rely mainly on the basic cell rather than periodic effects as it is the case for photonic crystal or more generally electromagnetic band gap material. Their basic cells are generally constituted of resonant inclusions which yield a π phase shift in the material response above the resonant frequency. As a consequence, their effective permittivity and permeability can be negative either in separate or overlapping frequency bands, a unique and distinct property that is not observed in naturally occurring materials¹. For the latter condition they can be considered as double negative or negative index media hence

opening the effective parameter space, so that new functionalities in the light scattering can be envisaged.

Also recently, the achievement of near-zero or less than unity values of the effective permittivity and permeability was also recognized as one of the major goals of this research area. Great progress in electromagnetic metamaterials has been achieved for these unique physical properties and novel potential applications, such as negative refraction^{2,3}, perfect lens^{4,5} and cloaking⁶⁻⁸ have been shown. They have been experimentally demonstrated in a frequency range from the radio frequencies⁹ to millimeter waves¹⁰, infrared wavelengths¹¹⁻¹³, and visible optics¹⁴. Up to date, most of metamaterials are constructed with the use of sub-wavelength resonant metallic elements. For instance, the first left-handed

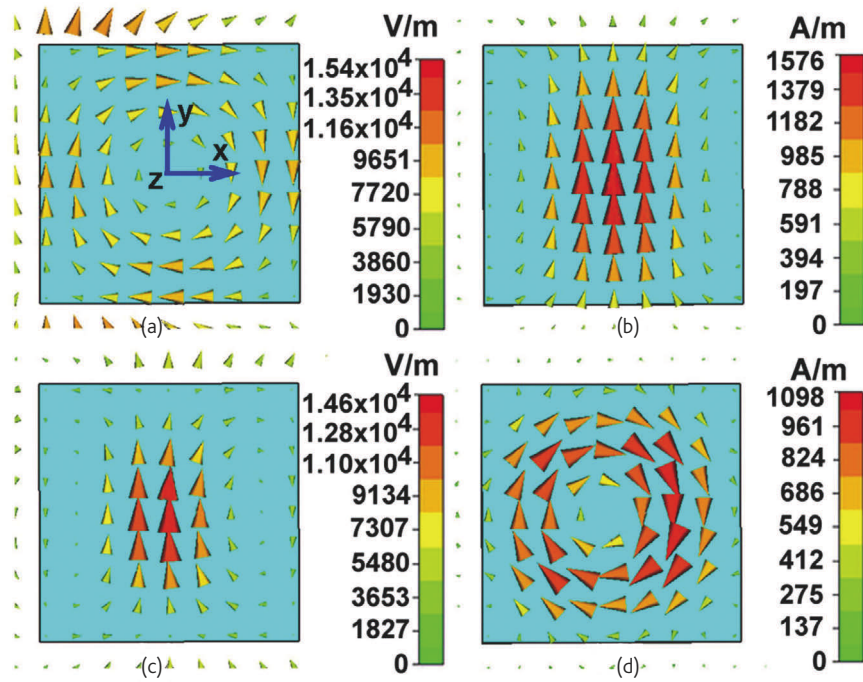


Fig. 1 Electric and magnetic field distribution in a dielectric cube with the magnetic field polarized along the z axis and electric field polarized along the y axis. (a) Electric field in the plane $z=0$ near the first Mie resonance. (b) Magnetic field in the plane $y=0$ near the first Mie resonance. (c) Electric field in the plane $z=0$ near the second Mie resonance. (d) Magnetic field in the plane $y=0$ near the second Mie resonance. (Reprinted with permission from³⁷. © 2008 American Physical Society.)

metamaterials (LHMs) with simultaneously negative permittivity and permeability have been fabricated by means of metallic split ring resonators (SRRs) and wires^{15, 16}, for tailoring the magnetic and electric responses, respectively. Other metallic elements, such as Ω -shaped structures^{17, 18}, U -shaped structures¹⁹, staplelike structures²⁰, paired rods²¹, dendritic²² and fishnet structures²³, are also successfully used to fabricate LHMs.

Usually, the metallic constitutive elements have conductive loss and anisotropic electromagnetic responses. Several authors have suggested methods^{24–26} to construct isotropic metamaterials by combining metallic SRRs and wires. However it is difficult to fabricate the bulk arrays of complex geometry with submicron or nanoscale sizes in order to generate a negative permeability effect at infrared and optical frequencies²⁷.

Recently, another route based on the interaction between electromagnetic waves and dielectric particles^{28, 29} was proposed to achieve the electric or magnetic resonances. The Mie resonances of dielectric inclusions provide a novel mechanism for the creation of magnetic or electric resonance based on displacement currents, and offer a simpler and more versatile route for the fabrication of isotropic metamaterials operating at higher frequencies. The progress on metallic elements-based metamaterials has been reviewed in many articles^{30–32} and books^{33, 34}. In this review, we focus on the scattering mechanisms based on Mie resonance in dielectric particles and describe the recent progress in these metamaterials including ferroelectric and polaritonic particles and their tunable behaviors.

Mie resonance of particles

From the viewpoint of scattering theory, all scattering objects can be represented by effective electric and/or magnetic polarizability densities. Light scattering by small (relative to the incident light wavelength) spherical particles is a fundamental topic in classical electrodynamics³⁵, and is based upon the exact Mie solution of the diffraction problem³⁶. The scattered field of a single isolated dielectric sphere with radius r_0 and relative refractive index n can be decomposed into a multipole series with the 2^m -pole term of the scattered electric field proportional to

$$a_m = \frac{n\Psi_m(nx)\Psi_m'(x) - \Psi_m(x)\Psi_m'(nx)}{n\Psi_m'(nx)\xi_m'(x) - \xi_m(x)\Psi_m'(nx)} \quad (1)$$

whereas the 2^m -pole term of the scattered magnetic field is proportional to

$$b_m = \frac{\Psi_m(nx)\Psi_m'(x) - n\Psi_m(x)\Psi_m'(nx)}{\Psi_m'(nx)\xi_m'(x) - n\xi_m(x)\Psi_m'(nx)} \quad (2)$$

where $x=k_0r_0$, k_0 is the free-space wavenumber, and $\Psi_m(x)$ and $\xi_m(x)$ are the Riccati-Bessel functions. The primes indicate derivation with respect to the arguments. The scattering coefficient a_m and b_m are related to the electric and magnetic responses of the sphere, respectively. From the Mie theory we can calculate the electric and magnetic dipole coefficients, a_1 and b_1 , respectively. From effective medium theory, we know that these are the multipole terms which contribute most significantly to the effective permittivity and

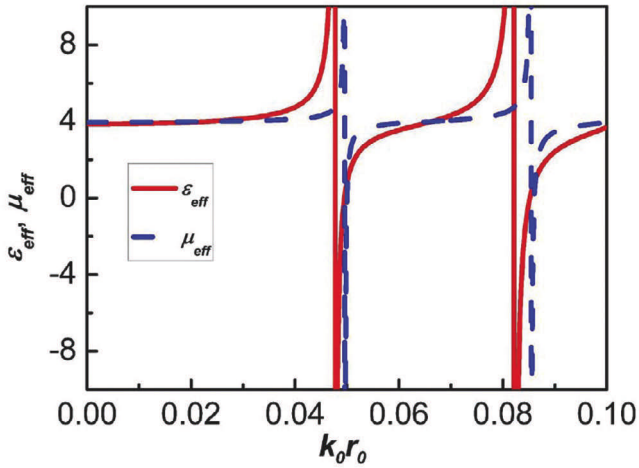


Fig. 2 Calculated effective permittivity ϵ_{eff} and permeability μ_{eff} of the magnetodielectric sphere arrays composite. (Reprinted with permission from²⁹. © 2003 IEEE.)

permeability of the particle composite. Since the magnetic response of a nonmagnetic particle is usually weak, it is important to strengthen the electromagnetic resonant behavior. For the lowest resonant frequencies of a_1 and b_1 , the sphere exhibits electric and magnetic dipoles. This conclusion can be assessed from the electromagnetic intensity distributions in a high dielectric ceramic cube for a plane incident wave propagating along the x axis³⁷ (Fig. 1). It can be seen that the electric or magnetic fields are mainly localized in the cubes. The azimuthal component of the displacement current inside each cube is greatly enhanced at the first Mie resonance (Fig. 1a) resulting in a large magnetic field along the z axis (Fig. 1b) which corresponds to the TE_{011} Mie resonance mode. At the second Mie resonance, the y component of the displacement current inside the cubes increases dramatically (Fig. 1c) and hence with a large magnetic field along the azimuth (Fig. 1d), which corresponds to the TM_{011} Mie resonance mode.

These electric and magnetic dipole resonances act as artificial 'atoms' which form the basis of new optical materials. In a material made up of a collection of such resonant particles, their combined scattering response can act like a material with almost arbitrary values of effective permittivity and permeability. This idea can be verified by using the model proposed in 1947 by Lewin³⁸ who considered the electromagnetic scattering properties of a composite material which was constituted of an array of lossless magnetodielectric spheres (ϵ_2 and μ_2) embedded in another background matrix (ϵ_1 and μ_1). The effective permittivity ϵ_{eff} and permeability μ_{eff} expressions based on Mie theory are as follows³⁸.

$$\epsilon_{eff} = \epsilon_1 \left(1 + \frac{3v_f}{\frac{F(\theta) + 2b_e}{F(\theta) - b_e} - v_f} \right) \quad (3)$$

$$\mu_{eff} = \mu_1 \left(1 + \frac{3v_f}{\frac{F(\theta) + 2b_m}{F(\theta) - b_m} - v_f} \right) \quad (4)$$

where

$$F(\theta) = \frac{2(\sin\theta - \theta \cos\theta)}{(\theta^2 - 1)\sin\theta + \theta \cos\theta} \quad (5)$$

$$b_e = \epsilon_1/\epsilon_2, \quad b_m = \mu_1/\mu_2 \quad (6)$$

The volume fraction of the spherical particles,

$$v_f = \frac{4}{3}\pi \left(\frac{r_0}{p}\right)^3, \quad \theta = k_0 r_0 \sqrt{\epsilon_2 \mu_2}, \quad r_0 \text{ and } p \text{ are the particle radius and}$$

the lattice constant, respectively. Eq 5 shows that $F(\theta)$ is a resonant function and becomes negative above resonance in some range of θ , resulting in the negative permittivity or permeability for negative values of $F(\theta)$ with a magnitude on the order of unity as given by Eqs. (3) and (4).

In Lewin's model, the constitutive parameters were formulated only considering the spheres resonating either in the first or second resonant modes of the Mie series. This is because the higher order Mie resonances often occur at frequencies beyond the long wavelength limit, and thus the Clausius-Mossotti equation does not apply. Then, Jylha *et al.*³⁹ improved those formulations by taking into account the electric polarizabilities of spheres operating in the magnetic resonant modes.

Independent of Lewin's model, O'Brien and Pendry²⁸ showed that a negative effective permeability can be obtained in a two-dimensional array of ferroelectric rods with the magnetic field polarized along the axes of the rods. Although the underlying physics is the same, the authors used another method⁴⁰ (transfer matrix method) to find the effective media values with similar conclusion. The aforementioned theoretical results show that a high permittivity microstructured medium can exhibit isotropic negative values of the effective permeability and permittivity.

Mie resonance as a new route for metamaterials

With the rapid development of LHMs, Lewin's model was reconsidered and introduced into the realm of metamaterials to realize single and double negative media. Based on Lewin's model, Holloway *et al.*²⁹ numerically demonstrated the feasibility of achieving simultaneously negative ϵ_{eff} and μ_{eff} in the magnetodielectric sphere arrays for wavelengths where the electric and magnetic resonances are excited in the spheres. Eqs. (3) and (4) show that ϵ_{eff} and μ_{eff} depend on the permeability and permittivity of the dielectric inclusions and host medium, as well as the volume fraction of spheres of radius r_0 . Fig. 2 shows ϵ_{eff} and μ_{eff} calculated for $v_f = 0.5$, $\epsilon_1 = \mu_1 = 1$, $\epsilon_2 = 40$, and

$\mu_2 = 200$ as a function of $k_0 r_0$. There are two regions where both ϵ_{eff} and μ_{eff} become negative with the bandwidths becoming narrower by decreasing the volume fraction v_f .

From a practical point of view, many kinds of materials and shapes of particles have been proposed in the literature to fabricate negative or less than unity permeability and permittivity dielectric metamaterials operating in different frequency regions. The designing ideas are summarized in the following.

Magnetic response

The realization of abnormal permeability is a tricky issue for various metamaterials, because the magnetic response of materials is usually weak, especially at infrared or visible frequencies. Lewin's model shows that two methods based on Mie resonance can be used to achieve a negative effective permeability effect. The first one is to use magnetodielectric inclusions with large values of permeability and permittivity. The second method is to use nonmagnetic dielectric particles with extremely large permittivity values. In the former case, two terms b_e and b_m in Eqs. (3) and (4) contribute to the negative permeability, while only b_e plays an important role for the latter. The possibility to use magnetodielectric particles has been numerically demonstrated²⁹. However a magnetodielectric particle with simultaneously large values of permittivity and permeability seems physically unattainable even in the microwave. Eq. (4) indicates that nonmagnetic spheres with very high permittivity values can also be employed to induce negative permeability and permittivity effects at the different Mie resonance frequencies.

Polaritonic materials, such as ionic solids and polar semiconductors, or ferroelectric materials can provide the large permittivity. For ferroelectric materials, their extreme high permittivity values can be preserved at least up to millimeter wavelengths⁴¹. At infrared frequencies however a roll-off of the dielectric constant is observed so that they cannot be used in this frequency range. In contrast, the lattice resonance in polaritonic crystals can be exploited to tailor the permittivity resonance at infrared and optical frequencies. As a consequence, the polaritonic resonance of crystals could be potentially used in the infrared spectral region. The relative permittivity is⁴²

$$\epsilon_r(\omega) = \epsilon(\infty) \left(1 + \frac{\omega_L^2 - \omega_T^2}{\omega_T^2 - \omega^2 - i\omega\gamma} \right), \quad (7)$$

where $\epsilon(\infty)$ is the high-frequency limit of the permittivity, ω_T and ω_L are the transverse and longitudinal optical phonon frequencies, and γ is the damping coefficient. Therefore, large values of $\epsilon_r(\omega)$ can be achieved near the transverse phonon frequency.

A three-dimensional dielectric composite consisting of an array of dielectric cubes [$\text{Ba}_{0.5}\text{Sr}_{0.5}\text{TiO}_3$ (BST)] with a relative permittivity of 1600 in a Teflon substrate was fabricated (Fig. 3a) to demonstrate the feasibility of this full dielectric metamaterial route. On this basis, isotropic negative values of the effective permeability were

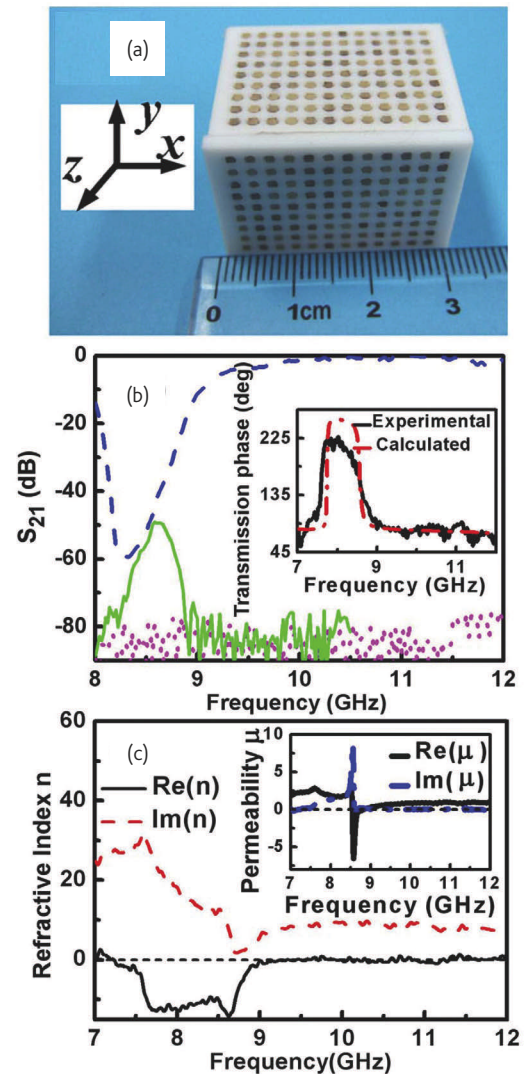


Fig. 3 A three-dimensional dielectric composite with isotropic negative permeability. (a) Photograph of BST cubes arrayed in Teflon substrate. (b) Transmission for the dielectric cube array only (dashed line), wire array only (dotted line), and the combination of BST cubes and wires (solid line). Inset of Fig. 3(b) shows the measured and calculated transmission phase. (c) Retrieved refractive index and permeability (inset). (Reprinted with permission from³⁷. © 2008 American Physical Society.)

experimentally demonstrated in the microwave region³⁷. The dielectric cube side length l was 1.0 mm for a lattice constant of 2.5 mm. And the first TE and TM resonance modes, i.e., magnetic and electric resonances were determined by transmission measurements at 6.12 and 8.28 GHz respectively. Using smaller cubes ($l = 0.75$ mm) with a magnetic resonance near 8.5 GHz, in conjunction with an electric response from metallic wires, researchers fabricated double negative media. The results of transmission measurements are displayed in Fig. 3b and the retrieved electromagnetic parameters (Fig. 3c) further verified the negative permeability near the first Mie resonance.

A rectangular dielectric block⁴³ and piezoelectric disks⁴⁴ were also experimentally verified to design very low-loss magnetic metamaterials.

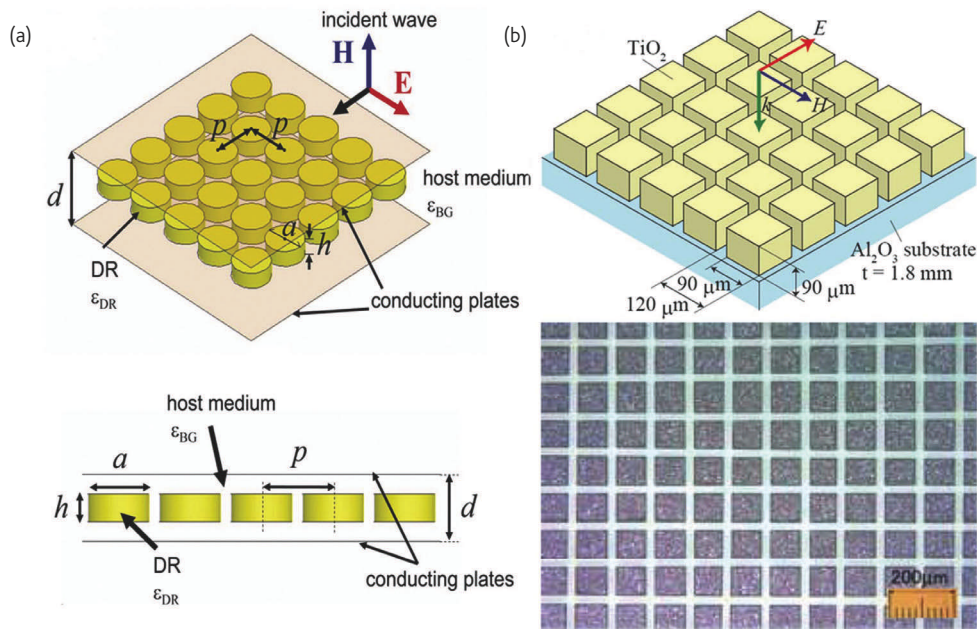


Fig. 4 Schematic of metamaterials based on Mie resonance. (a) A two-dimensional lattice structure for one dielectric-resonator in the cutoff microwave waveguide. (Reprinted with permission from⁴⁵. © 2007 IEEE.) (b) Terahertz metamaterial consisting of polycrystalline TiO_2 cubes-arrays on the Al_2O_3 substrate. (Reprinted with permission from⁴⁸. © 2008 Metamaterials.)

Also a two-dimensional square lattice of dielectric disk inserted between two metallic parallel-plate waveguide (Fig. 4a) was also used to demonstrate negative refraction, where the macroscopic behavior of dielectric disk provides negative effective permeability and the waveguide plays a role in a TE cut-off waveguide leading to negative effective permittivity⁴⁵. A dielectric block [(Zr,Sn) TiO_4 ceramics, dielectric constant 36.7] with a thin metallic rod screwed inside was proposed to fabricate gradient metamaterial lenses and numerically demonstrated to deflect and focus the incident plane waves⁴⁶. Dielectric-resonator-based composite right/left-handed transmission lines used to the design of leaky wave antenna can alleviate the significantly large conducting loss and increase the radiation efficiency⁴⁷. Terahertz metamaterials based on the Mie resonance of polycrystalline TiO_2 cubes-arrays on the Al_2O_3 substrate (Fig. 4b) were also experimentally demonstrated by Shibuya *et al.*⁴⁸, in which the negative permeability and permittivity occur around 0.28 and 0.38 THz, respectively.

A three-dimensional collection of polaritonic spheres was proposed to obtain isotropic negative effective permeability near the first Mie resonance at infrared frequencies⁴⁹. The calculated effective parameters (LiTaO_3 crystal) reported in this reference are shown in Fig. 5 and the isotropy of electromagnetic properties was also verified by a comparison with a full multiple scattering approach. Semiconductor nanoparticles, such as CuCl with a $3P$ exciton line at 386.93 nm, Cu_2O with a $2P$ exciton⁵⁰, and GaP ⁵¹ were also suggested to realize negative permeability within and below the optical region. Metal nanoclusters possessing large permittivity at visible frequency can also be used to obtain magnetic Mie resonance^{52, 53}.

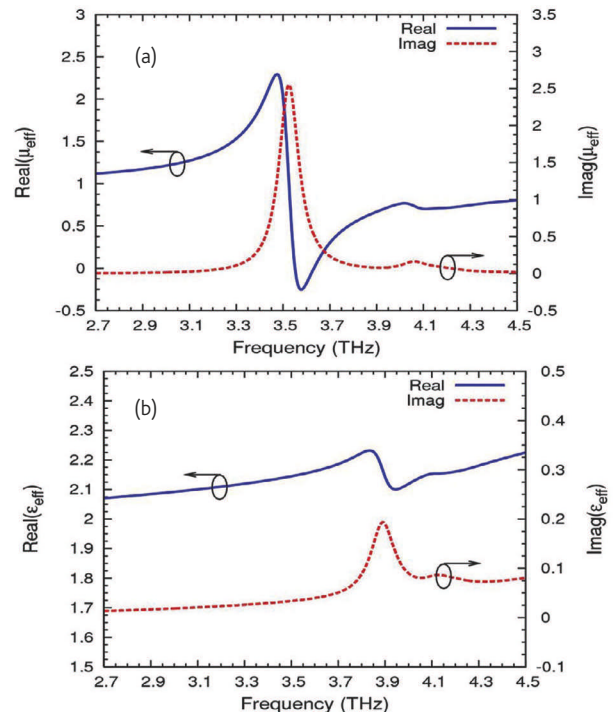


Fig. 5 The calculated effective relative permeability (a) and permittivity (b) of a collection of LiTaO_3 spheres. (Reprinted with permission from⁴⁹. © 2005 American Physical Society.)

Similar to spherical or cubic dielectric elements, the cylindrical particles can also generate the Mie electromagnetic resonances. The most important issue is to determine the resonant modes. For

a TE polarization (E field perpendicular to the rod axis), the lowest Mie resonance mode (TE_0) corresponds to the magnetic response, resulting in negative permeability values. A two-dimensional array of ferroelectric rods^{28, 54} and polaritonic rods⁵⁵ were proposed to obtain negative effective permeability⁵⁶, which can be considered as the TE_0 mode. For TM polarization (E field parallel to the rod axis), the lowest two Mie resonances modes, TM_0 and TM_1 , correspond to the electric and magnetic responses, and consequently lead to negative permittivity and permeability, respectively. The electromagnetic field distribution displayed for the TM_1 mode (Fig. 6) can further clarify the magnetic resonance mechanism⁵⁷. The electric field is distributed along the $\pm z$ directions with opposite signs along the propagation direction (Fig. 6b), accounting for a strong circular displacement current (Fig. 6d). Such displacement current results in a large magnetic field along the y axis (Fig. 6c), which corresponds to the TM_1 mode.

Electric response

An electric response can be accomplished with simpler metallic structures, such as uncoupled rods or strips. The first method to obtain negative permittivity is the bulk metals at optical frequencies, where conduction electrons can be assumed to be reasonably free and plasma-like behavior is responsible for a negative dielectric permittivity at frequencies less than the plasma frequency⁵⁸. Usually, the plasma frequencies of metals are at ultraviolet frequencies and dissipation is small. As the frequency is much lower than the plasma frequency, the imaginary part of the complex permittivity increases dramatically while very large negative values of the real part are obtained.

Pendry *et al.*⁵⁹ suggested a metallic wire array structure to realize a plasma-like state. With such a configuration, the negative permittivity frequency range can be tuned by the lattice constant and the wire diameter in the low frequency spectral region even at microwave frequencies. Additionally, negative dielectric permittivity can also be obtained in more ordinary dielectric media with bound charges, within a frequency band above a resonance frequency, where the resonant Lorentz permittivity occurs⁵⁸.

Another method is to use the electric resonant mode of the Mie resonance of dielectric particles. For the dielectric sphere or cube, it can be equivalent to a dipole at the second resonant mode as exemplified by the field mapping shown in Fig. 1. For a dielectric column particle, it can be equivalent to an electric dipole at the first resonance mode (TM_0) and can result in negative permittivity.

Negative refraction

The mechanisms of electric and magnetic resonances in dielectric particles (spheres, cubes or rods) have been analyzed above. Negative refraction can be fulfilled by combing the two resonances together. However, the first electric resonance (TM mode) is at a higher frequency than the fundamental magnetic resonance (TE mode) for the identical sphere. Due to the different resonance frequencies of TE and TM modes in the different-sized particles, we can consider the conditions when the first lowest resonance of TM_{011} mode related to a bigger sphere coincides with the TE_{011} resonance in a smaller sphere. Recently, Vendik *et al.*^{60, 61} numerically studied an artificial double negative media whose basic unit cell is composed by two

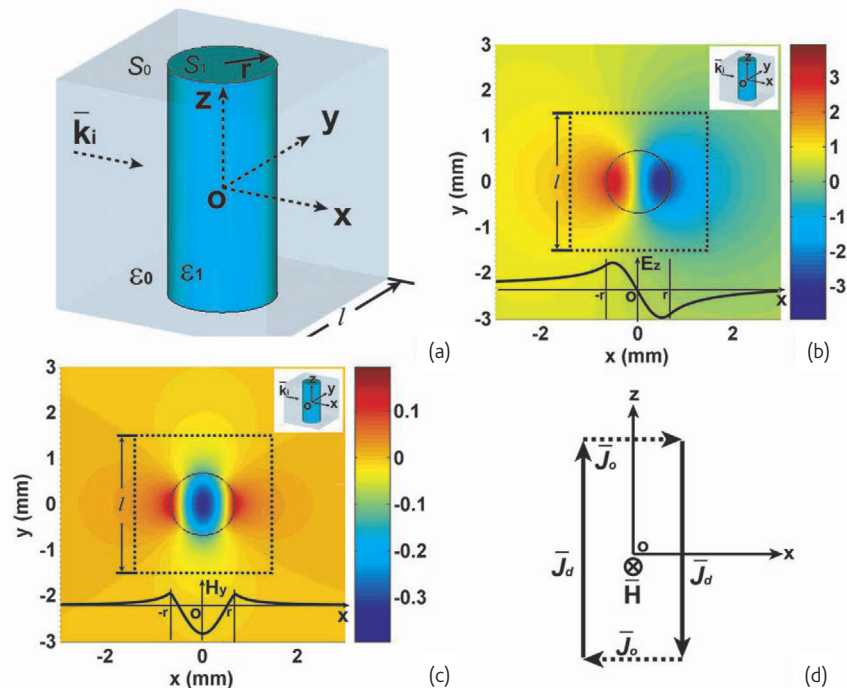


Fig. 6 Electric and magnetic field distributions in a dielectric rod at the second resonant mode (TM_1 mode). (a) Unit cell configuration. (b) Electric field distribution. (c) Magnetic field distribution. (d) Equivalent current ring. (Reprinted with permission from⁵⁷. © 2007 American Physical Society.)

dielectric spheres of different sizes. The larger sphere was used for the negative permeability while the small one allows achieving a negative permittivity in the same microwave frequency band. At the same time, two sets of spheres, having the same size but different materials, were also developed to realize negative refraction⁶². More recently, a three-dimensional isotropic negative-index composite at infrared or visible frequencies was reported^{51, 63-66}. The proposed homogeneous isotropic structures consist of dielectric spheres (gallium phosphide) embedded randomly in a negative permittivity host medium (Cesium)⁵¹, or two interpenetrating lattices of spheres⁶³⁻⁶⁶. One lattice ensures a negative permeability using a polaritonic material (LiTaO₃, SiC, CuCl) and the other lattice creates a negative permittivity effect by using a plasmonic material (n-type Ge, Au, MgB₂). Negative refraction index effect exists not only in the situation of a regular lattice arrangement but also for randomly distributed nanoparticles when the losses are ignored. However, the numerical results also demonstrated that the negative refraction could not be achieved owing to the large imaginary part of the wave vector corresponding to evanescent rather than propagating waves when the losses of the constitutive materials were taken into account.

Another method to fabricate isotropic LHMs based on Mie resonance is using only one kind of micron-scale non-magnetic coated spheres⁶⁷⁻⁶⁹. The underlying physical mechanisms correspond to a negative effective permeability effect due to polaritonic sphere core while a negative effective permittivity effect results from an electric-dipole resonance of sphere coating on its outer surface whose dispersion follows a Drude model. For an isolated sphere, an electric dipole resonance can be driven when its material permittivity is -2 . Since this permittivity value is negative, the electric field is evanescent within the sphere so that such electric dipole resonance is a surface resonance in contrast to the volume effect of the magnetic resonance. Therefore, the coating can be designed to have a negative permittivity. Note that the magnetic resonance of the core is hardly affected, as long as the permittivity of the coating remains small in comparison to the large permittivity of the core. The spheres with a core of a polaritonic crystal LiTaO₃ and the coated thin layer of a Drude model semiconductor (or a polaritonic material) were used to demonstrate isotropic negative refraction⁷⁰. The calculated effective electromagnetic parameters are shown in Fig. 7. Such three-dimensional LHMs consisting of metal-coated semiconductor spheres can be used to realize subwavelength imaging⁷¹ and electromagnetic transparency^{72, 73}.

Besides dielectric spheres array, the electric and magnetic Mie resonances in dielectric rods can also be used to achieve negative permittivity and permeability values. Under TM illumination, a resonant permittivity due to the TM₀ mode excitation and a resonant permeability due to the TM₁ mode excitation can be used to realize negative permittivity and permeability, respectively. Schuller *et al.*⁷⁴ experimentally and numerically observed and identified the Mie

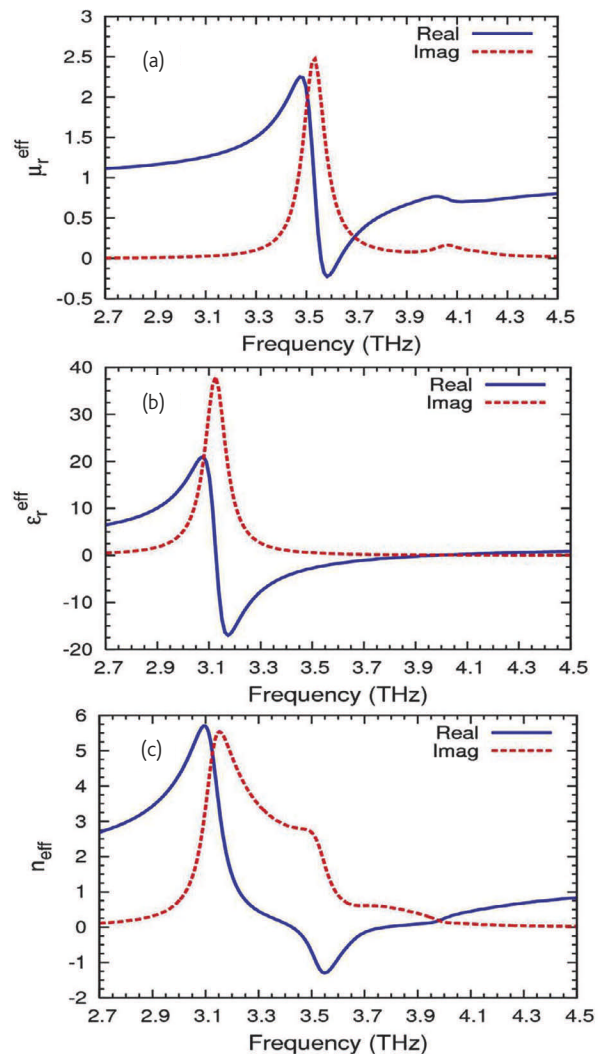


Fig. 7 The effective (a) permeability, (b) permittivity, and (c) index of a collection coated spheres. The cores are made of LiTaO₃ with radius 4 μm , and the coatings are a Drude material with radius 0.7 μm . (Reprinted with permission from⁷⁰. © 2006 American Physical Society.)

resonance modes of SiC particles at mid-IR under various polarization conditions. Also they proposed to obtain a negative refractive index by combining the two resonances of TM₀ and TM₁ modes (Fig. 8).

A theory on the electric and magnetic dipole activities of dielectric rods in s-polarized light was presented recently. The authors claimed that large wavelength-to-period ratios do not necessarily result in an isotropic metamaterial. They also suggested that silicon rod arrays could exhibit a true metamaterial left handed dispersion branch in the visible to mid-IR despite the moderate value of the refractive index ($n \sim 3.5$)⁷⁵. Such a conclusion is interesting by considering Mie resonance in moderate permittivity materials in optics. It has however to be checked by experiments in order to discriminate negative refraction effects resulting from the conventional band folding in the diffraction regime⁷⁶ from pure left handed branch effects in the

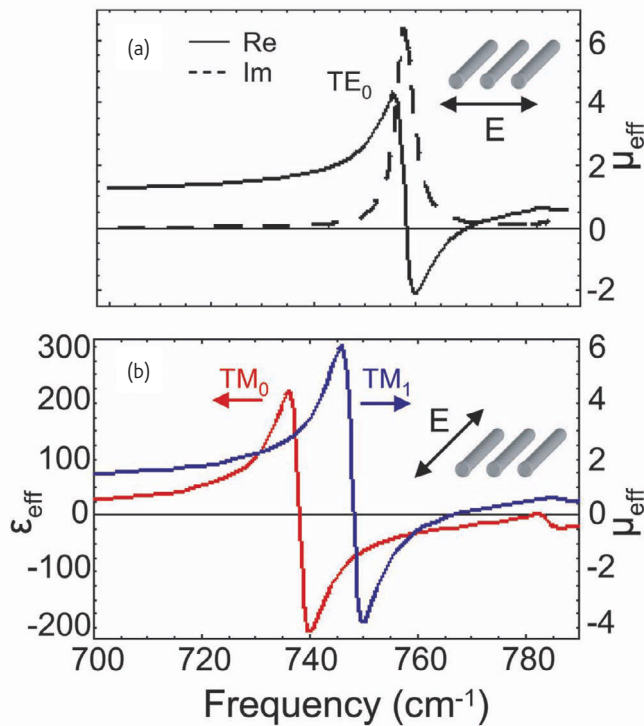


Fig. 8 (a) Calculated effective permeability for a normal incidence TE illuminated array of infinitely long SiC rods. (b) Calculated permittivity (permeability) due to excitation of the zeroth (first) order TM mode. (Reprinted with permission from⁷⁴. © 2007 American Physical Society.)

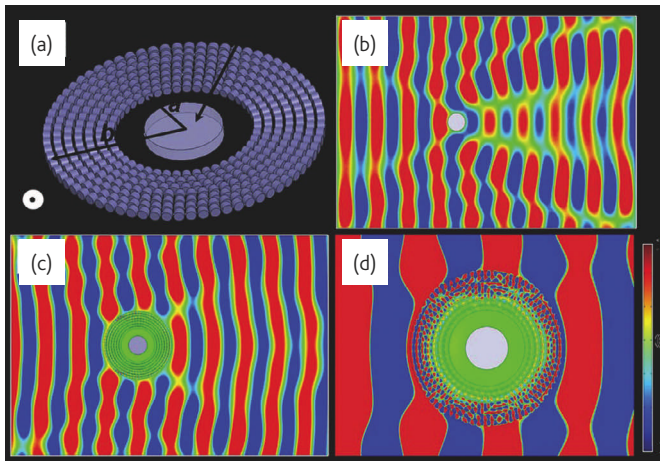


Fig. 9 (a) Schematic of a terahertz all-dielectric cloak. Steady-state E_z pattern calculated at 0.58 THz for a copper rod without (b) and with cloak (c). (d) Magnified view of the field pattern of (c). (Reprinted with permission from⁷⁷. © 2008 Optical Society of America.)

long wavelength regime. A verification of negative refraction in a TM illuminated array of large permittivity ceramic rods was experimentally verified at microwave frequencies, corresponding to the combination of TM_0 and TM_1 modes⁵⁷.

All-dielectric cloaks

Conformal transformation of electromagnetic domains has been proposed as an exciting approach to control the flow of propagating

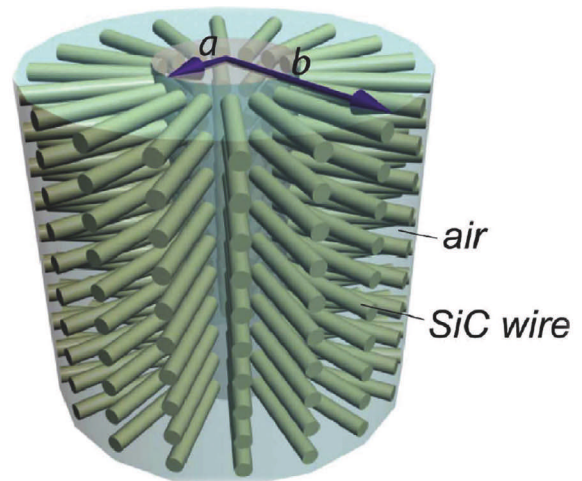


Fig. 10 Schematic of a cylindrical non-magnetic cloak for TE polarization at mid-infrared. (Reprinted with permission from⁷⁸. © 2008 Optical Society of America.)

waves and realize invisibility cloak⁶. Effective permeability can be less than unity around the magnetic resonance and such metamaterials have been suggested to construct invisibility cloak^{7, 8}. An all-dielectric cloak (Fig. 9) consisting of radially positioned micrometer-sized ferroelectric cylinders was suggested to perform cloaking at 0.58 THz, which exhibits a strong magnetic resonance based on Mie theory⁷⁷.

At last, Silicon Carbide (SiC) rod, a polaritonic material with phonon resonance bands centered around 12.5 μm , was also suggested to built transparency cloak (Fig. 10) at mid-infrared with the TE resonance mode⁷⁸. To sum up, an all-dielectric configuration provides an attractive route for designing cloaking devices at microwave, terahertz and infrared frequencies.

Tunable Mie resonance-based metamaterials

As seen in the previous sections, resonance effects in the electric and magnetic responses appear as a necessary condition for fabricating left-handed metamaterials. Such resonances are strongly dependent on the geometrical dimensions and on the dielectric properties of the constitutive elements. Usually negative values can only be achieved over a narrow frequency range near the resonances, especially for the magnetic resonance. From the application point of view, and for a deeper understanding of the intrinsic properties of negative media, it is desirable to implement structures with tunable and reconfigurable resonant properties⁷⁹. Some tunable metamaterials based on the metallic structures have been proposed by modifying the locally dielectric or permeability environment. For example, a control of the electric and magnetic responses of SRRs and related configurations was experimentally demonstrated through photoexcitation of free carriers in a GaAs substrate⁸⁰, electrically or magnetically controlled liquid crystals^{81, 82}, along with electroreological fluids^{83, 84}, ferroelectric⁸⁵, ferromagnetic materials⁸⁶⁻⁸⁹ and other methods⁹⁰. All these examples correspond however to anisotropic tunable metamaterials whereas

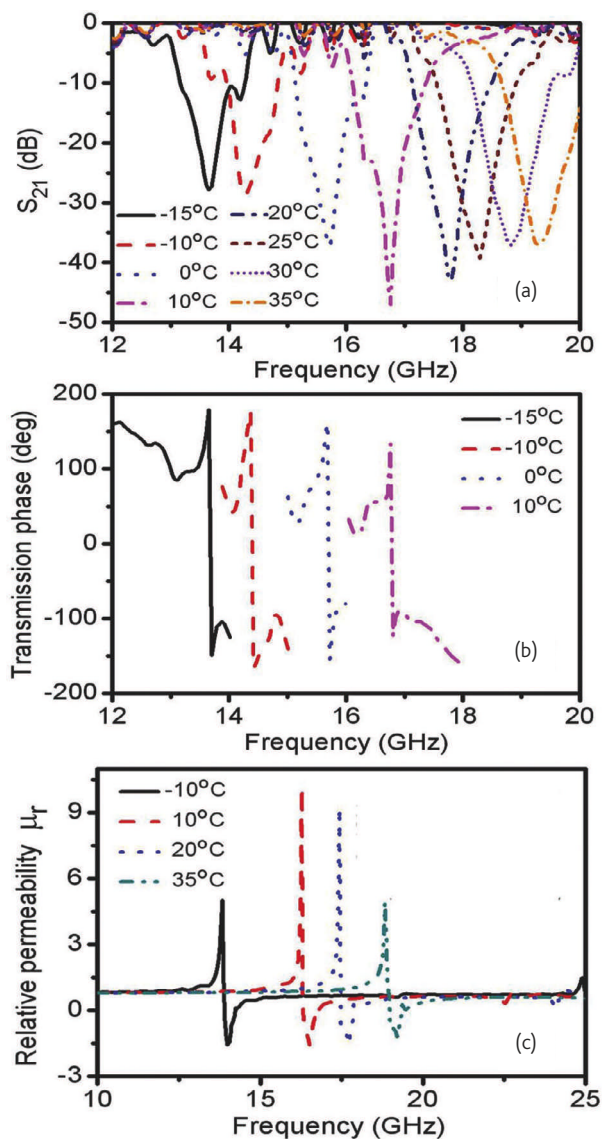


Fig. 11 The actively modulated isotropic negative permeability dielectric composite. (a) Dependence of the first magnetic resonance on the temperature. (b) Dependence of transmission phases on the temperature. (c) Calculated effective permeability under different temperature. (Reprinted with permission from⁹¹. © 2008 American Institute of Physics.)

isotropic properties can be more suitable for potential applications notably for all angle negative refraction.

The first dynamic tuning of isotropic metamaterial relying on Mie resonance has been demonstrated recently by altering the dielectric property of the basic cell⁹¹. As expected from the Mie resonance theory, at the first resonance the dielectric sphere is equivalent to a magnetic dipole with a resonance frequency $\omega \approx \pi c / (r_0 \sqrt{\epsilon_2})$ within the long-wavelength limit. Usually, the permittivity of the high κ ceramic inclusions varies as a function not only of the local field, but also of temperature⁹². Therefore, a variation of the effective permeability of the composite material can be realized by changing

the sample temperature. For a proof of this principle, a simple cubic lattice of ceramic cubes of 0.45 mm side length (BST doped with 5wt% MgO) were arrayed in a Teflon substrate with a lattice constant of 1.25 mm. The microwave scattering parameters were measured under various temperature conditions (Fig. 11a, b). The magnetic resonance corresponding to the first Mie resonance in the dielectric cubes can be continuously and reversibly adjusted from 13.65 GHz to 19.28 GHz with a temperature changing from -15°C to 35°C. The frequency dependence of the effective permeability, displayed in Fig. 11c, shows that negative permeability values can be achieved in a frequency band of about 6 GHz by a temperature variation of 50°C. It is believed that this temperature controlled metamaterial could be used for the design of adaptive three-dimensional metamaterials and invisibility cloaks which exhibit basically a very narrow fractional bandwidth of the order of 1%⁹³.

Another method used to adjust the negative refraction of Mie resonance is to alter the dielectric property of the background medium. Khoo *et al.*⁹⁴ proposed nanospheres dispersed liquid crystals to realize tunable negative–zero–positive index of refraction in the optical and terahertz regimes.

Outlook

As an alternative method for the design of electromagnetic metamaterials, the dielectric particles show several advantages, notably in terms of isotropic parameters, and the fabrication techniques targeting at higher frequencies of operation. Although several experimental demonstrations have allowed the verification of the first principles at microwave and terahertz frequencies, it appears that the research on this area is at a very primary stage with numerous theoretical and numerical studies. Further experimental works are expected at mid-term in order to demonstrate the possibility of fabricating isotropic negative index material notably in the infrared and visible frequency ranges. Towards this goal the challenging issues are the preservation of large dielectric constant and low loss in these frequency ranges, which appear as the necessary condition to operate in the long wavelength regime. The introduction of active materials may alleviate or even overcome the problem of intrinsic losses⁹⁵. At last the inexpensive chemical methods, such as colloidal crystallization, may be suitable for the synthesis of nanoparticles^{96, 97}. Although much work is needed before practical implementations are possible, dielectric metamaterials are a promising candidate for real-world application of the many exciting opportunities provided by electromagnetic metamaterials. mt

Acknowledgments

This work is supported by the National Science Foundation of China under Grant Nos. 50425204, 50621201, 50632030, 60608016 and 10774087, and by the State Key Lab of Tribology under Grant No. SKLT 08B12. D.L. would like also to thank the Delegation Générale pour l'Armement for its support in the framework of the contract 06.34.021.

Reference

1. Pendry, J. B., *Nature Mater.* (2006) **5**, 763.
2. Shelby, R. A., *et al.*, *Science* (2001) **292**, 77.
3. Houck, A. A., *et al.*, *Phys. Rev. Lett.* (2003) **90**, 137401.
4. Pendry, J. B., *Phys. Rev. Lett.* (2000) **85**, 3966.
5. Fang, N., *et al.*, *Science* (2005) **308**, 534.
6. Pendry, J. B., *et al.*, *Science* (2006) **312**, 1780.
7. Schurig, D., *et al.*, *Science* (2006) **314**, 977.
8. Cai, W., *et al.*, *Nat. Photonics* (2007) **1**, 224.
9. Wiltshire, M. C. K., *et al.*, *Science* (2001) **291**, 849.
10. Zhang, F. L., *et al.*, *Appl. Phys. Lett.* (2008) **93**, 083104.
11. Dolling, G., *et al.*, *Science* (2006) **312**, 892.
12. Linden, S., *et al.*, *Science* (2004) **306**, 1351.
13. Liu, H., *et al.*, *Adv. Mater.* (2008) **20**, 2050.
14. Dolling, G., *et al.*, *Opt. Lett.* (2007) **32**, 53.
15. Pendry, J. B., *et al.*, *IEEE Trans. Microw. Theory Tech.* (1999) **47**, 2075.
16. Smith, D. R., *et al.*, *Phys. Rev. Lett.* (2000) **84**, 4184.
17. Huangfu, J., *et al.*, *Appl. Phys. Lett.* (2004) **84**, 1537.
18. Zhang, F. L., *et al.*, *IEEE Trans. Microw. Theory Tech.* (2008) **56**, 2566.
19. Enkrich, C., *et al.*, *Phys. Rev. Lett.* (2005) **95**, 203901.
20. Zhang, S., *et al.*, *Phys. Rev. Lett.* (2005) **94**, 037402.
21. Shalaev, V. M., *et al.*, *Opt. Lett.* (2005) **30**, 3356.
22. Zhou, X., and Zhao, X. P., *Appl. Phys. Lett.* (2007) **91**, 181908.
23. Dolling, G., *et al.*, *Opt. Lett.* (2006) **31**, 1800.
24. Baena, J. D., *et al.*, *Appl. Phys. Lett.* (2006) **88**, 134108.
25. Gay-Balmaz, P., and Martin, O. J. F., *Appl. Phys. Lett.* (2002) **81**, 939.
26. Koschny, T., *et al.*, *Phys. Rev. B* (2005) **71**, 21103.
27. Veselago, V. G., and Narimanov, E. E., *Nat. Mater.* (2006) **5**, 759.
28. O'Brien, S., and Pendry, J. B., *J. Phys.: Condens. Matter* (2002) **14**, 4035.
29. Holloway, C. L., *et al.*, *IEEE Trans. Antennas Propag.* (2003) **51**, 2596.
30. Shalaev, V. M., *Nat. Photon.* (2007) **1**, 41.
31. Padilla, W. J., *et al.*, *Materials Today* (2006) **9**, 28.
32. Soukoulis, C. M., *et al.*, *Adv. Mater.* (2006) **18**, 1941.
33. Engheta, N., and Ziolkowski, R. W., (eds.), *Electromagnetic Metamaterials: Physics and Engineering Explorations*, Wiley-IEEE Press, New Jersey, USA, (2006).
34. Marques, R., Martin, F., and Sorolla, M., *Metamaterials with Negative Parameters: Theory, Design, and Microwave Applications*, Wiley-Interscience Press, New Jersey, USA, (2007).
35. Jackson, J. D., *Classical Electrodynamics*, 2nd ed., Wiley, New York, USA, (1999).
36. Bohren, C. F., and Huffman, D. R., *Absorption and Scattering of Light by Small Particles*, Wiley-Interscience, New York, USA, (1983).
37. Zhao, Q., *et al.*, *Phys. Rev. Lett.* (2008) **101**, 027402.
38. Lewin, L., *Proc. Inst. Electr. Eng.* (1947) **94**, 65.
39. Jylha, L., *et al.*, *J. Appl. Phys.* (2006) **99**, 043102.
40. Contopanagos, H. F., *et al.*, *J. Opt. Soc. Am. A* (1999) **16**, 1682.
41. Houzet, G., *et al.*, *Appl. Phys. Lett.* (2008) **93**, 053507.
42. Kittel, C., *Introduction to Solid State Physics*, 7th ed., John Wiley and Sons Inc., New York, USA, (1996).
43. Popa, B.I., and Cummer, S.A., *Phys. Rev. Lett.* (2008) **100**, 207401.
44. Acher, O., *et al.*, *Appl. Phys. Lett.* (2008) **93**, 032501.
45. Ueda, T., *et al.*, *IEEE Trans. Microw. Theory Tech.* (2007) **55**, 1280.
46. Lin, X. Q., *et al.*, *Appl. Phys. Lett.* (2008) **92**, 131904.
47. Ueda, T., *et al.*, *IEEE Trans. Microw. Theory Tech.* (2008) **56**, 2259.
48. Shibuya, K., *et al.*, *Terahertz metamaterials composed of TiO₂ cube arrays*, Presented at 2nd International Congress on Advanced Electromagnetic Materials in Microwaves and Optics, Pamplona, Spain, September 21-26, 2008.
49. Wheeler, M. S., *et al.*, *Phys. Rev. B* (2005) **72**, 193103.
50. Yannopapas, V., and Vitanov, N. V., *Phys. Rev. B* (2006) **74**, 193304.
51. Seo, B. J., *et al.*, *Appl. Phys. Lett.* (2006) **88**, 161122.
52. Wu, Q., and Park, W., *Appl. Phys. Lett.* (2008) **92**, 153114.
53. Rockstuhl, C., *et al.*, *Phys. Rev. Lett.* (2007) **99**, 017401.
54. Felbacq, D., and Bouchitte, G., *New J. Phys.* (2005) **7**, 159.
55. Huang, K. C., *et al.*, *Appl. Phys. Lett.* (2004) **85**, 543.
56. Felbacq, D., and Bouchitte, G., *Phys. Rev. Lett.* (2005) **94**, 183902.
57. Peng, L., *et al.*, *Phys. Rev. Lett.* (2007) **98**, 157403.
58. Ramakrishna, S. A., *Rep. Prog. Phys.* (2005) **68**, 449.
59. Pendry, J. B., *Phys. Rev. Lett.* (1996) **76**, 4773.
60. Vendik, O. G., and Gashinova, M. S., in Proceedings of the 34th European Microwave Conference, Amsterdam (IEEE Press, Piscataway, NJ, 2004), Vol. 3, pp. 1209-1212.
61. Vendik, I. B., *et al.*, *Tech. Phys. Lett.* (2006) **32**, 429.
62. Ahmadi, A., and Mosallaei, H., *Phys. Rev. B* (2008) **77**, 045104.
63. Yannopapas, V., *Phys. Rev. B* (2007) **75**, 035112.
64. Kussow, A. G., *et al.*, *Phys. Stat. Sol. B* (2008) **245**, 992.
65. Kussow, A. G., *et al.*, *Phys. Rev. B* (2007) **76**, 195123.
66. Yannopapas, V., *Appl. Phys. A* (2007) **87**, 259.
67. Qiu, C. W., and Gao, L., *J. Opt. Soc. Am. B* (2008) **25**, 1728.
68. Yannopapas, V., *Phys. Stat. Sol. (RRL)* (2007) **1**, 208.
69. Alu, A., and Engheta, N., *J. Appl. Phys.* (2005) **97**, 094310.
70. Wheeler, M. S., *et al.*, *Phys. Rev. B* (2006) **73**, 045105.
71. Yannopapas, V., *J. Phys.: Condens. Matter* (2008) **20**, 255201.
72. Gao, L., *et al.*, *Phys. Rev. E* (2008) **78**, 046609.
73. Alu, A., and Engheta, N., *Phys. Rev. E* (2005) **72**, 016623.
74. Schuller, J. A., *et al.*, *Phys. Rev. Lett.* (2007) **99**, 107401.
75. Vynck, K., *et al.*, "All-dielectric rod-type metamaterials operating at optical frequencies," <http://arxiv.org/abs/0805.0251> (2008).
76. Fabre, N., *et al.*, *Phys. Rev. Lett.* (2008) **101**, 073901.
77. Gaillot, D. P., *et al.*, *Opt. Express* (2008) **16**, 3986.
78. Cai, W., *et al.*, *Opt. Express* (2008) **16**, 5444.
79. Chen, H. T., *et al.*, *Nature* (2006) **444**, 597.
80. Padilla, W. J., *et al.*, *Phys. Rev. Lett.* (2006) **96**, 107401.
81. Zhao, Q., *et al.*, *Appl. Phys. Lett.* (2007) **90**, 011112.
82. Zhang, F. L., *et al.*, *Appl. Phys. Lett.* (2008) **92**, 193104.
83. Hou, B., *et al.*, *Opt. Express* (2005) **13**, 9149.
84. Huang, Y., *et al.*, *Prog. Nat. Sci.* (2008) **18**, 907.
85. Hand, T. H., and Cummer, S. A., *J. Appl. Phys.* (2008) **103**, 066105.
86. Kang, L., *et al.*, *Appl. Phys. Lett.* (2008) **93**, 171909.
87. Kang, L., *et al.*, *Opt. Express* (2008) **16**, 8825.
88. Kang, L., *et al.*, *Opt. Express* (2008) **16**, 17269.
89. Zhao, H. J., *et al.*, *Appl. Phys. Lett.* (2007) **91**, 131107.
90. Chen H., *et al.*, *Appl. Phys. Lett.* (2006) **89**, 053509.
91. Zhao, Q., *et al.*, *Appl. Phys. Lett.* (2008) **92**, 051106.
92. Vendik, O. G., and Zubko, S. P., *J. Appl. Phys.* (1997) **82**, 4475.
93. Gaillot, D. P., *et al.*, *New J. Phys.* (2008) **10**, 115039.
94. Khoo, I. C., *et al.*, *Opt. Lett.* (2006) **31**, 2592.
95. Gordon, J. A., and Ziolkowski, R. W., *Opt. Express* (2007) **15**, 2622.
96. Huang, X. G., *et al.*, *Langmuir* (2007) **23**, 8695.
97. Li, W., *et al.*, *Langmuir* (2008) **24**, 13772.



Powdery melting points

With M5000 melting point of powdery substances can be analyzed. Measuring is fully automatic. A fan cooling allows fast measurements in every range of temperature. A printer may be connected optionally.

- Digital temperature control with 0.1 °C resolution
- Ventilator cooling
- Automatic determination of melting point
- Signal tone when melting point is reached
- Keypad for easy cleaning
- RS-232 interface for printer connection
- English and german error message in clear text

Contact: www.kruess.com

Opportunity under the microscope

A six figure investment in sophisticated new equipment is helping Teesside-based scientists focus in on new opportunities.

Intertek MSG, which is based at the Wilton Centre, has acquired a state-of-the-art electron microscope to enhance the services offered to its customers working in the areas of nanotechnology and materials science.

The purchase, which was made jointly with fellow Wilton Centre tenant NanoCentral, will enable Intertek MSG to offer researchers the ability to examine an extended range of materials in even greater detail.

Director Dr Simon Allen said: "Our work involves the investigation and analysis of products as diverse as aerospace composites, pharmaceuticals and medical devices. The new addition to our equipment ensures our scientists have the best available resource to help solve our customers' problems and grow their businesses."

He added: "For many years electron microscopes have enabled us to look in minute detail at structures too small for a light microscope but until now we could only study dry or dried samples."

"The exciting thing about our new analytical instrument is that for the first time we can also examine the microstructures of wet materials. This greatly expands the range of industries that we can support and is excellent news both for our business and our customers."

Formerly part of ICI, Intertek MSG has been based at the Wilton Centre since the 1970s.

Dave Willis, Wilton Centre manager, said the company "flies the flag" for excellence in scientific research.

"With continued investment like this to support them, the team can only go from strength to strength," he added.

Contact: www.wiltoncentre.co.uk

Residual gas analyzer

Micromeritics introduces the MicroStar residual gas analyzer, a quadrupole mass spectrometer that complements Micromeritics' AutoChem 2920 and 2950 dynamic chemisorption analyzers. The MicroStar is ideally suited for pulse chemisorption studies and temperature-programmed reactions allowing the user to follow the evolution of residual gases from the AutoChem. This information may then be used to determine reaction kinetics, product selectivity, and reaction yields; all of which are vital components of a successful catalyst development program. Unlike traditional temperature-programmed desorption or reduction experiments where only one active gas is monitored, the MicroStar provides continuous monitoring of reaction products (up to 128 different masses).

Contact: www.micromeritics.com



Temperature measurement and control.

The first of a new generation of innovative temperature measurement and control solutions by Lake Shore, the Model 336 temperature controller comes standard equipped with many advanced features promised to deliver the functionality and reliable service you've come to expect from the world leader in cryogenic thermometry. The Model 336 is the only temperature controller available with four sensor inputs, four control outputs and 150 W of low noise heater power. Two independent heater outputs providing 100 W and 50 W can be associated with any of the four sensor inputs and programmed for closed loop temperature control in proportional-integral-derivative (PID) mode. The improved autotuning feature of the Model 336 can be used to automatically collect PID parameters, so you spend less time tuning your controller and more time conducting experiments.

Contact: www.lakeshore.com

Carl Zeiss has launched a new system for optical sectioning

The ELYRA product family features several new superresolution microscopy methods and significantly expands the application of light microscopy by clearly resolving details which previously could not be imaged by commercially available systems.

ELYRA's high resolution and flexibility will allow scientists to expand their experimental design to enable study of cellular components smaller than the diffraction limit.

The new LSM 780 expands the LSM 7 laser scanning microscopy family. This new system has about double the sensitivity of existing laser scanning microscopes and allows the study of samples with very weak or quickly bleaching fluorescence signals. The improved sensitivity can also be used to collect images at higher speeds.

The third new product, VivaTome, is a new optical sectioning system created for developmental and cell biologists to examine the dynamics of living specimens. The VivaTome is easy to use and provides clear and quantifiable images of cell structures, tissue sections or living organisms.

With the launch of the new systems, ELYRA, LSM 780 and VivaTome, Carl Zeiss offers important new tools to allow scientists to expand their research horizons.

Contact: www.zeiss.de

Combined AFM and raman solution for advanced materials research

Bruker announces the official launch of the new N8 NEOS SENTERRA micro-analysis system that combines the Raman Spectroscopy and Atomic Force Microscopy (AFM) on a single optical microscope platform.

A comprehensive materials research investigation demands a multi-technique approach. Bruker Optics' SENTERRA Raman spectrometer and Bruker Nano's N8 NEOS Atomic Force Microscope was combined to allow morphological, structural and chemical analysis of the same sample area. Calibrated sample positioning allows simple and precise serial measurements, where the resultant Raman spectra is easily correlated with the AFM image.

Contact: www.brukeroptics.com



From Molecules to Monolayers: Self-Assembly and Analysis, Molecule by Molecule

Date: Now available on demand (Webinar recorded: Tuesday 17th November 2009)

Registration: Free

Moderator: Jonathan Agbenyega, Commercial Editor, *Materials Today Magazine*

Panelists: Paul Weiss, Director, California NanoSystems Institute and Professor, Chemistry and Biochemistry at University of California, Los Angeles
Milan Mrksich, Professor of Chemistry at the University of Chicago and Investigator at the Howard Hughes Medical Institute

Description:

Self-assembly has been likened to taking a jigsaw puzzle box, shaking it and when you open the box you find the jigsaw puzzle correctly made! As research in this field develops, we are continually finding more and more naturally occurring self-assembly systems in the complex world around us.

The breadth of application of self-assembly vast and this educational webinar will focus on:

- Using Self-Assembled Monolayers and Mass Spectrometry for BioChip Applications
- Self and Directed Assembly for the Control of Single Molecule Environments

The webinar is aimed at alternative energy researchers, surface chemists, mass spec audience, organic electronics, polymer science, self-assembly, molecular electronics and a number of biological audiences such as: proteomics, enzyme researchers and analytics.

Registration Details:

→ www.materialstoday.com/webinars



In-Situ Nanomechanical Testing Techniques: Opening Doors to a New World of Materials Characterization

Date: Now available on demand (Webinar recorded: Wednesday 18th November 2009)

Registration: Free

Moderator: Jonathan Agbenyega, Commercial Editor, *Materials Today Magazine*

Panelists: Dr. Oden Warren, CTO, Hysitron, Inc.
Dr. William Gerberich, University of Minnesota
Dr. S.A. Syed Asif, Director of R&D, Hysitron, Inc.

Description:

Next generation materials research is highly dependent on the development and application of innovative nanomechanical testing techniques. This webinar will cover the background and future of advanced in-situ nanomechanical characterization techniques that are becoming increasingly pertinent to research institutions and industries around the world.

The newest developments in nanoindentation-based techniques have further expanded materials characterization capabilities of researchers by combining several other cutting-edge techniques and capabilities, including: TEM/SEM, heating/cooling, acoustic emission monitoring, dynamic mechanical analysis (DMA), quantitative mechanical property mapping, electrical contact resistance, and scanning probe microscope (SPM) imaging. Combining standard nanomechanical testing with any of the in-situ capabilities discussed in this webinar greatly enhances the amount of information one can obtain from depth-sensing indentation testing.

Registration Details:

→ www.materialstoday.com/webinars

FORTHCOMING EVENTS

30 November 2009 – 4 December 2009
Materials Research Society Fall Meeting
 Boston – MA – USA

The increasingly cross-disciplinary worldwide activity on materials research culminates every year in the MRS Fall Meetings. Symposium organizers from around the world have created a program that addresses leading-edge research and captures the extraordinary progress in materials science and technology, featuring an exciting mix of well-established and popular topics.

http://www.mrs.org/s_mrs/

4 – 7 December 2009
Nanotech Business Summit
 Cairo – Egypt

This conference brings together senior business leaders and world-renowned innovators to explore the ways that nanotechnology will become the next big growth innovation. The summit provides informative presentations, business match-making services and numerous networking opportunities to serve as an incubator of new ideas and new relationships.

<http://www.nanobus.sabrycorp.com/conf/nanobus/09/>

6 – 11 December 2009
11th Pacific Polymer Conference: Progress in Polymers for the New Millennium

Cairns – Australia

PPC11/31APS will be a major international gathering of polymer scientists and engineers. All aspects of our profession will be covered in a comprehensive program, including modern polymerization methodologies, living free radical polymerization, complex polymer architectures, functional polymers, nano-composites, traditional composites, electro- and optico-active polymers, polymers in biology and medicine, naturally-derived polymers, polymers at interfaces and surfaces, polymer engineering, polymer rheology, polymer processing, mechanical properties and polymer characterization.

<http://www.ppc11.org/>

7 – 11 December 2009
Characterisation of Advanced Materials

University of Surrey – UK

The aim of this five-day course is to introduce the principles of the most popular materials analysis

characterisation methods based on microscopy, chemical, physical and structural analysis and thermal techniques. Consideration is also given to the analysis of particulate materials and coatings.

http://portals.surrey.ac.uk/portal/page?_pageid=822,1938861&_dad=portal&_schema=PORTAL

13 – 17 December 2009
Third International Conference on Mechanics of Biomaterials & Tissues

Clearwater Beach – FL – USA

The aim of the Third International Conference on Mechanics of Biomaterials is to provide a forum for the discussion of the modeling and measurement of deformation and fracture behavior in biological materials and in those materials which are used to replace them in the human body. A particular theme of the conference will be how lessons learnt in the study of engineering materials can be made relevant to the study of biomaterials.

<http://www.icmbt.elsevier.com/>

10 – 14 January 2010
PCSI-37

Santa Fe – New Mexico, USA

The annual PCSI conference is devoted to achieving a fundamental understanding of the physical, chemical, biological, structural, optical, magnetic and electrical properties of surfaces and interfaces. These studies include characterization of growth processes, interfacial phenomena, transport and the structure and influence of defects. Generous amounts of discussion time will be included in the program in order to emphasize the workshop character and to stimulate the exchange of new ideas.

<http://www.pcsiconference.org/>

20 – 22 January 2010
Electronic Materials and Applications 2010

Orlando – FL – USA

Jointly programmed by the Electronics Division and Basic Science Division of ACeRS, this is the first in a series of annual meetings. The 2010 focus is on electronic ceramics for energy storage and conversion applications and the complementary fundamental science issues

<http://ceramics.org/electronic-materials-and-applications-2010/>

23 – 28 January 2010
SPIE Photonics West

San Francisco – USA

Experience SPIE Photonics West—the worlds leading photonics, laser, and biomedical optics event

<http://spie.org/x2584.xml>

24 – 29 January 2010
34th International Conference and Exposition on Advanced Ceramics and Composites (ICACC)

Daytona Beach – FL – USA

This conference showcases cutting-edge research and product developments in advanced ceramics, armor ceramics, solid oxide fuel cells, ceramic coatings, bioceramics and more. Investigate the 11 symposia and 4 focused sessions planned for 2010.

<http://ceramics.org/34th-international-conference-exposition-on-advanced-ceramics-composites/>

01 – 05 February 2010
Introduction to Physical Metallurgy

University of Surrey – Surrey – UK

The course aims to provide a general introduction to the field of Physical Metallurgy. It covers phase diagrams, transformation diagrams and the associated thermodynamics, diffusion, liquid-solid transformations, ferrous and non-ferrous materials and cold work, recovery and recrystallisation.

http://portals.surrey.ac.uk/portal/page?_pageid=822,1938865&_dad=portal&_schema=PORTAL

15 – 19 February 2010
Polymers: Science, Engineering and Applications

University of Surrey – Surrey – UK

This course combines a comprehensive study of the science and engineering of polymers with an up-to-date appreciation of the development and application of polymers in traditional and new areas. The course starts with a good insight into the physical and chemical structure and the various types of polymers. Polymer synthesis, chemical and physical processing techniques and manufacturing technologies are presented for the development of polymer structures and the manufacturing of polymer products for various applications.

http://portals.surrey.ac.uk/portal/page?_pageid=822,2436682&_dad=portal&_schema=PORTAL

materialstoday



ELSEVIER

diary

Each month we publish brief details of current and forthcoming meetings. The forthcoming meetings are listed for a 3 months period of time starting 3 months after the current issue, leaving sufficient time for registration. This list is not exhaustive.

If you are organizing a future conference or workshop and would like to have it listed in *Materials Today* please contact Jonathan Agbenyega – j.agbenyega@elsevier.com.

Events *Materials Today* has a contra deal with and that are relevant to the current issue of the magazine are listed in the box below.

If, as an organizer, you would like to discuss a contra deal, please contact Francesca Webb – f.webb@elsevier.com

30 November 2009 – 4 December 2009

Materials Research Society Fall Meeting

Boston – MA – USA

The increasingly cross-disciplinary worldwide activity on materials research culminates every year in the MRS Fall Meetings. Symposium organizers from around the world have created a program that addresses leading-edge research and captures the extraordinary progress in materials science and technology, featuring an exciting mix of well-established and popular topics.

http://www.mrs.org/s_mrs/

For further information please visit www.materialstoday.com/events

Solar

Ellipsometry Solutionssm

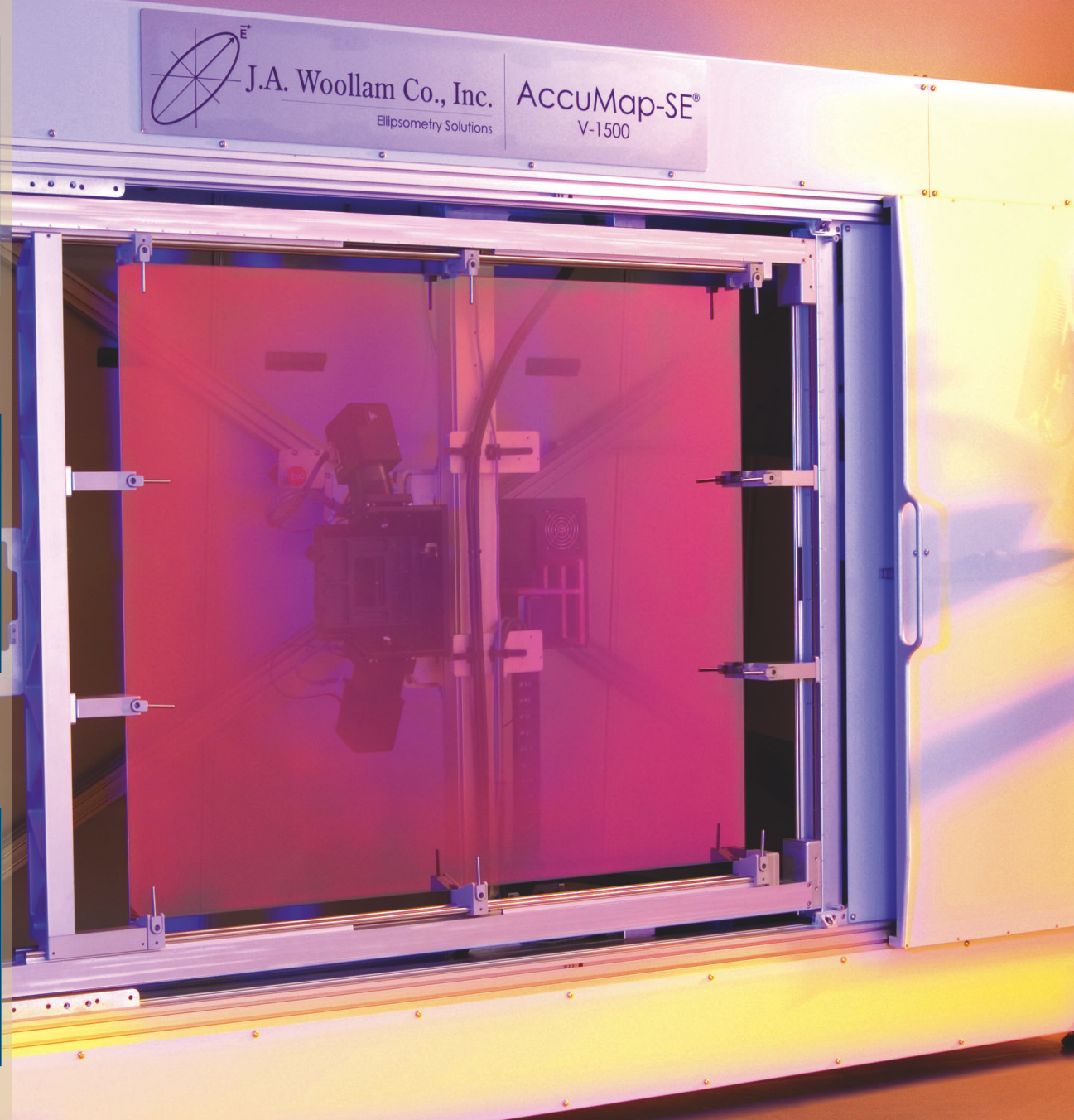
Thin Film
Characterization



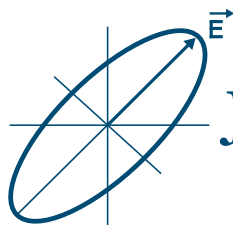
Measure Thickness
& Optical Constants



In situ
Feedback Control



We provide Ellipsometry Solutions for your thin films. Non-destructively characterize film thickness and optical constants for a wide range of coatings: amorphous and polycrystalline silicon, porous and nanostructured coatings, CIGS, CdTe/CdS, SiNx and other AR coatings, organic layers, transparent conductive oxides like ITO, AZO, and ZnO, and much more.



J.A. Woollam Co., Inc.

645 M Street, Suite 102 • Lincoln, NE 68508 • USA
Ph. 402-477-7501 • Fx. 402-477-8214
www.jawoollam.com

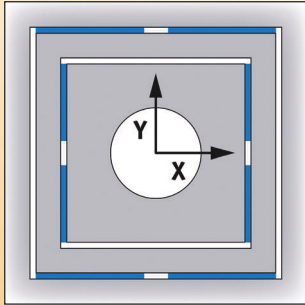
LOT
LOT ORIEL GRUPE EUROPA

Ph. +49-6151-8806-68
www.lot-oriel.com



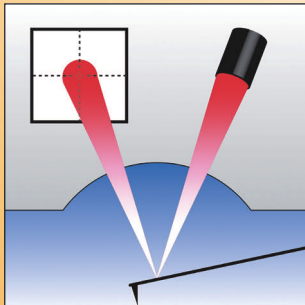
Nanosurf® easyScan 2 FlexAFM

Your Versatile AFM System for Materials and Life Science



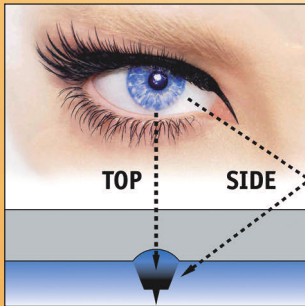
Flexure-Based Scanner Technology

The flexure structure at the basis of the XY-scanner is inherently flat and rugged. Being electromagnetically actuated, all scanning motions in this plane are highly linear. A decoupled piezo-based Z-scanner provides fast feedback response, thus allowing high scan speeds with high accuracy to be obtained.



SureAlign™ Laser Optics

Nanosurf's patented SureAlign™ technology makes laser adjustment upon changing to liquid environments a thing of the past. Whether measuring in air or in liquid, the FlexAFM laser is always right on target.



Superior Top and Side View in Liquid

Smart top and side view through the FlexAFM's optical system allow easy sample observation and approach. There is no difference in viewing quality between air and liquid.



Nanosurf AG
Grammetstrasse 14
CH-4410 Liestal / Switzerland

www.nanosurf.com

